

DISSERTATION

submitted to the

Combined Faculties for Natural Sciences and for Mathematics

of the Ruperto-Carola University of Heidelberg, Germany

for the degree of

Doctor of Natural Sciences

presented by

Dipl.–Phys. Markus Eberhard Hartung

born in Erftstadt-Liblar, Germany

Oral examination: 14th of May, 2003

Commissioning of the Adaptive Optics System NAOS-CONICA for the VLT

The way to First Light

Referees:

Prof. Dr. Hans-Walter Rix

Prof. Dr. Wolfgang Duschl

Abstract

In October 2002 NAOS-CONICA, one of the most powerful adaptive optics systems was offered to the astronomical community. The instrument is installed at the Very Large Telescope in Chile and operated by the European Southern Observatory. The adaptive optics system NAOS corrects for atmospheric turbulence and provides the near-infrared multi-mode camera and spectrograph CONICA with diffraction limited images. Development of NAOS was achieved by a French consortium, while CONICA was developed by a German consortium under the leadership of the Max-Planck-Institut für Astronomie, Heidelberg. In the context of this PhD thesis several critical contributions to the successful commissioning were made.

The major test and calibration results obtained on the way to First Light, i.e., during the laboratory, integration and commissioning periods are presented. They cover cryogenics, mechanics, optics and detector characteristics of CONICA.

A major achievement was the development and implementation of a technique for the calibration of static optical aberrations. Since the instrument is designed to achieve absolute Strehl ratios higher than 70%, even the accumulation of residual static wavefront perturbations arising from optical components in the imaging path, critically affect the overall performance. The technique has been completely implemented for the instrument, and the adaptive optics system automatically corrects the static aberrations according to the different instrument configurations. The presented technique will be of great importance for future adaptive optics systems.

Particular attention is paid to the calibration of CONICA's high resolution imaging spectroscopy mode, realized by a cold tunable Fabry-Perot interferometer. A detailed guideline is given of how to process a phase-shift map and the capabilities for 3-dimensional structure analysis are demonstrated at Eta Carinae. A first, high-spatial resolution velocity map is created.

Zusammenfassung

Im Oktober 2002 wurde der astronomischen Gemeinschaft eines der leistungsfähigsten Systeme zur Korrektur atmosphärischer Turbulenz zugänglich gemacht. Das Instrument NAOS-CONICA ist am Very Large Telescope in Chile installiert und wird von der Europäischen Südsternwarte betrieben. Die adaptive Optik NAOS korrigiert atmosphärische Bildverzerrungen und liefert der Nahinfrarotkamera CONICA beugungsbegrenzte Bilder. Ein französisches Konsortium entwickelte NAOS, während CONICA durch ein deutsches Konsortium unter der Federführung des Max-Planck-Instituts für Astronomie in Heidelberg entwickelt wurde. Im Rahmen dieser Dissertation wurden bedeutende Beiträge zur erfolgreichen Inbetriebnahme des Instruments geleistet.

Die wesentlichen Test- und Kalibrationsergebnisse auf dem Weg zum "First Light" sind dargestellt. Sie schliessen Kryotechnik, Mechanik und Optik ein und beleuchten die Detektoreigenschaften von CONICA. Diese Ergebnisse wurden während der Labor-, Integrations- und Commissioning-Phase erzielt.

Eine besondere Errungenschaft ist die Entwicklung und Anwendung einer Technik, um statische optische Aberrationen zu kalibrieren. Da das Instrument für absolute Strehlzahlen größer als 70% konzipiert wurde, wird die Gesamtleistung wesentlich durch residuelle Wellenfrontstörungen beeinflusst, die durch die verschiedenen optischen Komponenten im abbildenden Lichtpfad verursacht werden. Diese Technik wurde vollständig im Instrument integriert und die Adaptive Optik korrigiert automatisch die statischen Aberrationen entsprechend der momentanen Konfiguration des Instruments. Die dargelegte Technik zur Kalibration statischer Wellenfrontstörungen ist von großer Bedeutung für zukünftige Instrumente mit adaptiver Optik.

Ein besonderes Augenmerk ist auf die Kalibration des kryogenen Fabry-Perot-Interferometers gerichtet. Die wesentlichen Schritte zur Erzeugung einer Phasenkarte werden ausführlich erklärt, und die Anwendungsmöglichkeiten zur 3-dimensionalen Strukturanalyse sind anhand von Eta Carinae dargelegt. Eine erste, hochauflösende Karte des Geschwindigkeitsprofils wurde erstellt.

Meiner Frau

Contents

1	Introduction	1
1.1	Historic remarks on AO Instrumentation and where we are	1
1.2	History and Schedule of the Project NAOS-CONICA	2
1.3	Outline of this Thesis	3
2	NAOS-CONICA	5
2.1	Description of the Instrument	5
2.2	CONICA	7
2.3	NAOS	9
3	Laboratory Tests and Calibrations of CONICA	13
3.1	Flexure	14
3.2	Cooling and instrumental background	14
3.3	Detector characteristics	18
3.3.1	Dark current and full well versus reverse bias	19
3.3.2	Cosmetics	20
3.3.3	Detector gain via the shot noise method	23
3.3.4	Conversion and linearity	23
3.3.5	Readout noise	24
3.4	Throughput	27
3.5	Direct imaging	28
3.5.1	Scale and distortion	28
3.5.2	Point Spread Functions	31
3.6	Long slit spectroscopy	31
3.7	Polarimetry	35

3.8	The Fabry-Perot Interferometer	35
3.8.1	Principles	37
3.8.2	Wavelength and order calibration	37
3.8.2.1	Fine calibration of the Grism's dispersion relation	38
3.8.2.2	Finesse	39
3.8.2.3	Calibration of FPI Scan Units	40
3.8.2.4	The phase jump correction	43
3.8.3	The phase map	45
3.8.4	Narrow fringes	50
4	Calibration of static aberrations of NAOS and CONICA	53
4.1	Application of the phase diversity technique	54
4.1.1	Estimation of static aberrations by Phase Diversity	54
4.1.1.1	Phase diversity principle	54
4.1.1.2	Imaging model	55
4.1.1.3	Aberration estimation principle	56
4.1.2	Phase diversity setup	58
4.1.2.1	CONICA stand-alone: focus shift by object	58
4.1.2.2	NAOS-CONICA: focus shift by the deformable mirror	60
4.1.3	Simulation results	61
4.1.4	Error budget	62
4.1.4.1	System limitations	64
4.1.4.2	Image limitations	68
4.1.4.3	Algorithm limitations	70
4.1.4.4	Conclusion	71
4.1.5	Practical example	72
4.1.5.1	Input data	72
4.1.5.2	Pre-processing	72
4.1.5.3	CONICA aberration estimation	74
4.2	Experimental Results	76
4.2.1	Calibration of NAOS and CONICA static aberrations	76
4.2.1.1	Disentanglement of the wavefront errors	78

4.2.1.2	Calibration of CONICA: camera and filters	79
4.2.1.3	Calibration of NAOS: dichroics	81
4.2.2	Image quality versus estimated aberrations	82
4.2.2.1	Strehl ratios by PD and focal plane image	82
4.2.2.2	Comparison of Strehl ratios	84
4.2.2.3	Focus adjustment	85
4.2.3	Closed loop compensation of NAOS-CONICA static aberrations	87
4.2.3.1	Rendering of aberrations	87
4.2.3.2	Full AO correction	87
4.3	Conclusion	89
5	A Fabry-Perot Scan of Eta Carinae	91
5.1	Data reduction	91
5.2	Eta Carinae	96
5.3	Investigation of the 3D structure of the Homunculus	96
5.4	Conclusion	100
6	Gallery	101
6.1	The way to First Light	101
6.2	Highlights during Commissioning and Science Verification	110
7	Summary and Conclusions	117
A	Argon calibration lines	119
B	Phase diversities and oversampling	121
C	Calculation of Strehl Ratios	123
C.1	SR via image space	123
C.2	SR via Fourier space	124
C.2.1	Finite pixel size	124
C.2.2	Diffusion	124

D PD results for broadband and neutral density filters	129
D.1 Image SR versus PD SR	129
D.2 PD calibration results	130
D.3 Conclusion	132
E List of publications	133
Bibliography	135
References	135
Technical Reports and Manuals	141
Abbreviations and Acronyms	143
Acknowledgements	145

Chapter 1

Introduction

1.1 Historic remarks on AO Instrumentation and where we are

Human curiosity has always triggered the development of new techniques in the hope to expand his mental horizon, to be pleased by discovery, and to obtain answers. Astrophysical research is driven by the same motives and the scientists do not get tired in inventing new methods and building new instruments to further improve the knowledge of our universe. The more details we would like to see, or the farer we want to go, the higher the spatial resolution we need. The diffraction-limited spatial resolution of telescopes is proportional to the ratio of observing wavelength and the diameter of the entrance aperture. Usually the aperture is given by the shape of the primary mirror. As the size of the primary mirrors increased during the evolution of telescopes, it quickly turned out that atmospheric turbulence limits the spatial resolution for primary mirrors bigger than 10 cm, i.e, a spatial resolution of 1 arcsec in the optical. The only advantage of further increase the diameter is to gain light collecting surface and improve the sensitivity.

Half a century ago, Babcock (1953) wrote about the possibility of compensating astronomical seeing.¹ He proposed to compensate the dynamic wavefront perturbations by a deformable mirror² in a conjugate image plane of the primary mirror.³ But his ideas were far ahead of the technical possibilities at that time, and it took more than 20 years to build an adaptive optics (AO) system able to sharpen images (Hardy et al. 1977). From then on, military application (satellite detection, ground surveillance, laser beacons) pushed the development of adaptive optics systems. First seeing compensated images of stars were obtained at the Air Force Maui Optical Site (AMOS) telescope in Hawaii in 1982 through the Advanced Research Projects Agency (ARPA). This agency was in charge of developing new technologies for the U.S. Department of Defense.

In the same way military applications (Hudson and Hudson 1975) accelerated the development of infrared detectors. They became accessible to civil use in astronomy later on. With the availability of low-noise infrared arrays and the fact that the demands on adaptive optics systems are less restrictive in the infrared, in 1989 time was ripe for the construction of the first successful civil adaptive optics

¹Seeing is an astronomical terminus to describe the degree of atmospheric turbulence. It is the size of the blurred spot of a non-resolved object, i.e a star. Typically the seeing of good astronomical sites is of the order of 1 arcsec.

²The deformable mirror was suggested to be realized by a thin layer of oil covering a mirror surface. The shape of the surface is controlled via electrostatic forces. This device is referred to as Eidophor.

³A modern introduction to the field of adaptive optics is found in Tyson (1998); Hardy (1998).

systems on an astronomical telescope (Rousset et al. 1990). This first prototype called COME-ON was installed at the 1.52-m telescope of the Observatoire de Haute Provence. In 1992, the system was upgraded and installed as COME-ON-PLUS at the 3.6-m telescope on La Silla, Chile. Two years later the operation was optimized and became a user facility instrument with the new name ADONIS.

Recently, its powerful successor NAOS was installed at one of the four 8.2-m telescopes of the Paranal observatory. Using a deformable mirror with 185 actuators, it provides the near-infrared camera CONICA with diffraction-limited images. Since October 2002, NAOS-CONICA is offered to the astronomical community and belongs to the most powerful astronomical instruments worldwide.

During the last decade, all large telescope projects have been running adaptive optics programs (VLT⁴, Keck⁵, Subaru⁶, Gemini⁷, CFHT⁸, Calar Alto⁹) and in particular for the future giant telescopes (30-100-m class) adaptive optics system technologies will play a major role.

1.2 History and Schedule of the Project NAOS-CONICA

CONICA, the COude Near-Infrared CAmera, a 1 to 5 μm infrared camera for diffraction-limited imaging and spectroscopy, was proposed by a consortium of the Max-Planck-Institut für Astronomie, Max-Planck-Institut für Extraterrestrische Physik and the Osservatorio Astronomico di Torino in response to a Call for Proposal from the European Southern Observatory (ESO). In 1991, it was selected as one of the first-generation instruments for the Very Large Telescope (VLT). Subsequent re-organization in the VLT schedule led to the (temporary) cancellation of the AO equipped Coudé foci and the loss of the Osservatorio Astronomico di Torino to the CONICA project. In 1994, studies for implementing AO at the VLT Nasmyth foci were initiated and, in parallel, an effort started to re-design CONICA and transform it into an instrument compatible with a Nasmyth focus. In 1997, a consortium consisting of the Office National d'Etudes et Recherches Aérospatiales (ONERA), Observatoire de Paris and Laboratoire d'Astrophysique de l'Observatoire de Grenoble (LAOG) was granted a contract to develop and build the Nasmyth AO System NAOS for the VLT.

Since the beginning of 2000, mechanics and optics of NAOS were pre-assembled in Grenoble. Optical components were verified and aligned. The stiffness of the mechanical main structure was tested. In August 2000, NAOS was transported to Bellevue near Paris, re-assembled, and prepared for the integration with CONICA.

The author joined the project in Summer 1999, when CONICA was running through its first cooling cycles. Having finished the main laboratory verification of the functionalities of CONICA stand-alone, the infrared camera was transported to Bellevue in October 2000, to be integrated with NAOS. The author accompanied the instrument and participated at the integration period in Paris, which after some schedule adjustments, lasted until September 2001.

⁴Very Large Telescope (4x8.2 m), Mount Paranal, Atacama desert, Chile, operated by the European Southern Observatory.

⁵W.M. Keck Observatory (2x10 m), Mauna Kea, Hawaii, operated by the California Institute of Technology.

⁶Subaru Telescope (8.2 m), Mauna Kea, Hawaii, operated by the National Astronomical Observatory of Japan.

⁷Gemini North (8.1 m), Mauna Kea, Hawaii, and Gemini South (8.1 m), Cerro Pachón, Chile, international partnership between U.S.A., U.K., Canada, Chile, Australia, Argentina and Brazil.

⁸Canadian-French-Hawaiian Telescope (3.6 m), Mauna Kea, Hawaii, operated by Canada-France-Hawaii Telescope Corporation.

⁹Calar Alto Observatory (3.5 m), Spain, operated by Centro Astronómico Hispano Alemán and the Max-Planck-Institut für Astronomie.

After the combined instrument had passed the preliminary acceptance officially reviewed by the contractor ESO, the instrument was shipped to Cerro Paranal, Chile. As a member of the commissioning team the author followed NAOS-CONICA on the mountain in order to assist to re-integration at the telescope and to performance evaluations and adjustments after First Light on November 25, 2001 (Brandner et al. 2002). In total, the four commissioning periods spread over 6 months from November 2001 until May 2002 with little recovery breaks in Europe in between.

Commissioning was followed by Science Verification that was performed by ESO, still with some remote support from the German and French instrument teams.

Finally, NAOS-CONICA has been opened to the astronomical community since October 2002.

1.3 Outline of this Thesis

Detailed descriptions of the instruments NAOS and CONICA and their respective sub-devices can be found in the literature. Therefore the description of the instrument in Chapter 2 is confined to a rough overview of the major design aspects and capabilities. The most important results obtained during the verification of CONICA stand-alone in Heidelberg are presented in Chapter 3. They cover cryogenics, mechanics, optics and detector characteristics of CONICA. Of particular interest is the description of the calibration procedure for the cold tunable Fabry-Perot, a rather unique sub-device for low-noise imaging spectroscopy with diffraction-limited spatial resolution.

The main achievement containing most of the personal research effort is described in detail in Chapter 4. It deals with the development of a technique to fully calibrate for remaining static aberrations of NAOS-CONICA arising from optical components outside the AO loop. CONICA's optical setup was extended to realize a phase diversity wavefront sensor. By this means the imaging optics and the CONICA detector itself allowed for wavefront sensing. A phase diversity algorithm developed by ONERA has been used to derive the wavefront error from the CONICA images. The measured wavefront error is described by a set of Zernike coefficients. These coefficients - describing the total wavefront error - are disentangled and assigned to the optical components that they stem from. The Zernike coefficients are managed by a database that is addressed by the instrument control software to update the AO system with the appropriate wavefront correction for the actual instrument configuration. The (absolute) achieved gain through pre-correction turns out to be 10% in J-band and 2-3% in K-band. Internal Strehl ratios as high as 70% in J-band in 93% in K-band are reached. Even this rather small appearing gain in K is of high importance. On the way to scientific goals as e.g. planet detection the total error budget must be tackled to eliminate every percentage point of loss in Strehl ratio. The successful implementation of this technique is an important aspect to ensure best optical performance of NAOS-CONICA, one of the most powerful AO systems. Moreover, this implementation may serve as guideline for future high performance AO systems.

Chapter 5 demonstrates the observing capabilities of CONICA's cold Fabry-Perot at Eta Carinae. The data have been acquired in December 2002 in a guaranteed observing time slot. A velocity map is generated with a phase-shift corrected data cube. Even if the Fabry-Perot scan was obtained with very short exposure times, a first high-spatial resolution map of Eta car is generated, and the exciting capabilities of 3-dimensional structure analysis are worked out.

Finally, a picture gallery illustrates moments on the way to First Light, and some technical and scientific highlights during Commissioning and Science Verification are picked out.

Chapter 2

NAOS-CONICA

2.1 Description of the Instrument

This chapter is dedicated to a brief description of the instrument NAOS-CONICA. Figure 2.1 gives a schematic overview of this VLT instrument. NAOS (Rousset et al. 1998, 2000) is attached to the Nasmyth B focus of the fourth unit telescope (UT4) called Yepun. It picks up an f/15 beam, corrects for atmospheric turbulence, and hands on again an f/15 beam providing CONICA with diffraction-limited images. Having passed the Nasmyth focal plane, the beam is led to a first collimating paraboloid. Then it is reflected successively onto the tip-tilt (TTM) and the deformable mirror (DM). A second off-axis paraboloid re-focuses the light onto the entrance focal plane of CONICA, which is located behind the entrance window in the cold cryostat. Between NAOS and CONICA an atmospheric dispersion compensator (ADC) can be slid in for observations at large zenith angles.¹ The dichroic mirror separates the optical train into the imaging path and the wavefront sensing path. NAOS offers five different dichroic beam splitters (Sect. 4.2.1.3) to adapt for the flux and the spectral characteristics of the guide star.

The wavefront sensing path consists of a field selector and two wavefront sensors. The field selector is located between the dichroic mirror and the wavefront sensor (WFS) input focus. For the sake of clarity these components are not shown in Fig. 2.1. The two WFSs of Shack-Hartmann type, one in the visible and one in the near-infrared spectral range², enhance the sky coverage³ of possible guide stars. The field selector chooses the guide star in a 2 arcmin field of view and allows differential object tracking⁴, pre-calibrated flexure compensation (Sect. 3.1), and counter-chopping. In combination with the deformable mirror it is also able to correct for a certain amount of defocus, as needed when the prisms of the atmospheric dispersion compensator are shifted into the beam. Note that this ability of focus correction offers a possibility to perform the measurements needed for the calibration of the static optical aberrations. This will be treated in Chapter 4.

The high angular resolution camera CONICA (Lenzen et al. 1998; Hartung et al. 2000) is equipped with an Aladdin InSb 1024² array covering the 1-5 μm spectral region. The pixel size is 27 μm with a

¹A pilot study for this device is found in Holzwarth (1992).

²The infrared wavefront sensor of NAOS is the first one world-wide that is operated routinely on a large AO system.

³The sky coverage is increased in the sense that specific astronomical sources of high scientific interest become accessible. In fact, IR wavefront sensors will always be sky background limited while visible WFS are still improving their characteristics. Regarding just the increase of sky coverage in terms of pure object numbers, the gain is small.

⁴A demonstration on Saturn is given in Sect. 6.2.

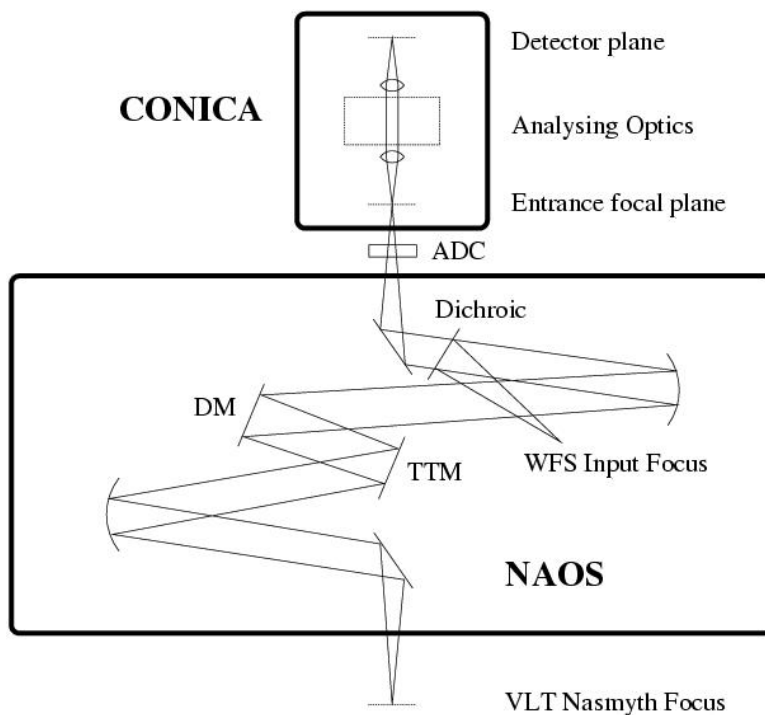


Figure 2.1: Outline of the VLT instrument NAOS-CONICA.

Table 2.1: The FWHM of a point source for a 8-m single-dish telescope (VLT-UT4).

J	H	K	L	M
32 mas	42 mas	57 mas	94 mas	116 mas

filling factor of approximately 100%. The detector gain is in the order of 10 electrons/ADU.⁵ Splitting the wavelength region into two parts (1.0 to 2.5 μm and 2.0 to 5.0 μm) allows one to keep the light path achromatic. Therefore, the four different pixel scales are realized by seven cameras (Table 2.2). To each pixel scale a camera is associated with the short wavelength region (S-camera) and another one with the long wavelengths region (L-camera). The only exception is the camera with the highest magnification (C50S). There is no long wavelength counterpart needed.⁶

A variety of different observing modes is provided by the analyzing optics: coronagraphy, low resolution long-slit spectroscopy, imaging spectroscopy by a tunable cold Fabry-Perot interferometer, polarimetry by wire-grids or Wollaston prisms, and about 40 broad- and narrow-band filters for direct imaging can be chosen. The testing and calibration of these modes is described in Chapter 3.

Further information about NAOS-CONICA is found in the user manual, in particular concerning the preparation of on-sky observations (Brandner et al. 2003, Manual). An up-to-date version can be accessed via the corresponding ESO website (ESO, NAOS-CONICA).

⁵Analogue Digital Unit.

⁶The Nyquist criterion for L and M-band is already fulfilled for a camera with lower magnification (C25L).

Table 2.2: Pixel scales and Field of view (FOV) of the camera objectives. The camera objectives were renamed after Commissioning. The new names are given in parentheses.

Camera Objective	Wavelength region	Scale (mas/pix)	FOV (arcsec)
C06S (S109)	1.0 - 2.5 μm	109.2	\varnothing 73
C06L (L109)	2.0 - 5.0 μm	109.2	\varnothing 73
C12S (S54)	1.0 - 2.5 μm	54.6	56 x 56
C12L (L54)	2.0 - 5.0 μm	54.6	56 x 56
C25S (S27)	1.0 - 2.5 μm	27.3	28 x 28
C25L (S27)	2.0 - 5.0 μm	27.3	28 x 28
C50S (S13)	1.0 - 2.5 μm	13.6	14 x 14

2.2 CONICA

Figure 2.2 gives an insight to the cryo-mechanical design of the near-infrared camera. The vacuum is provided by a turbo-molecular pump directly attached at the bottom of the cryostat. For clean, non-contaminated dewar conditions a high-vacuum down to 10^{-8} mbar can be established. The operational upper limit of pressure is at the order of 10^{-5} mbar. At this pressure limit, the cooling power still can fight the thermal coupling by the gas molecules and CONICA's components are not yet at the risk of damage. A closed-cycle cooler⁷ is employed for cooling the instrument. The interior of the instrument becomes dark for the infrared detector at temperatures below 80 K. The inner structure of the cryostat is connected with the powerful first stage of the cooling head. The second stage⁸, less powerful but colder, ensures the working temperature of the detector between 25 and 35 K. A system of hoses surrounding the inner structure allows one to accelerate the cooling procedure with liquid nitrogen. Typically, 100l are consumed for one cooling cycle. After two days cooling the functionalities of CONICA can be used and the detector leaves the regime of saturation. To reach the final equilibrium and to bring the instrumental background below the detection limit, at least four days cooling time is required.

The analyzing optics (masks, slits, pupil stops, gratings, polarizers, filters, and objectives) are fixed on several wheels. For focus adjustment the detector is attached to a tuning stage. All moving functions in the interior of the cryostat are controlled via motor encoder units that are mounted outside the dewar. This design approach has the advantage that the absolute encoder units can easily be accessed and in case of emergency the axles can be tuned manually. The disadvantage is the high effort in thermal shielding of the axles that are subject to a high temperature gradient from room temperature (300 K) to the temperature of the interior (< 80 K).

The adapter flange serves as the coupling piece between NAOS and CONICA. It houses a slider with an open and closed (warm) position, the tunable atmospheric dispersion compensator (TADC) and a mirror to fold the optical train towards the integration sphere.⁹ The sphere can be illuminated by continuous (Halogen) and spectral (Argon) light and is used for day-light or laboratory calibrations.

⁷Type: Leybold RGD 580. According to the Joules-Thomson effect the abrupt adiabatic expansion of helium is used as cooling mechanism. This is done in a closed loop, i.e. the expanded Helium gas is re-compressed and re-fed into the cooling head.

⁸The cooling head of the Closed Cycle Cooler comprises of two stages with different cooling power and different equilibrium temperature. E.g., assuming an equilibrium temperature of 60 K for the first stage, a cooling power of 50 W

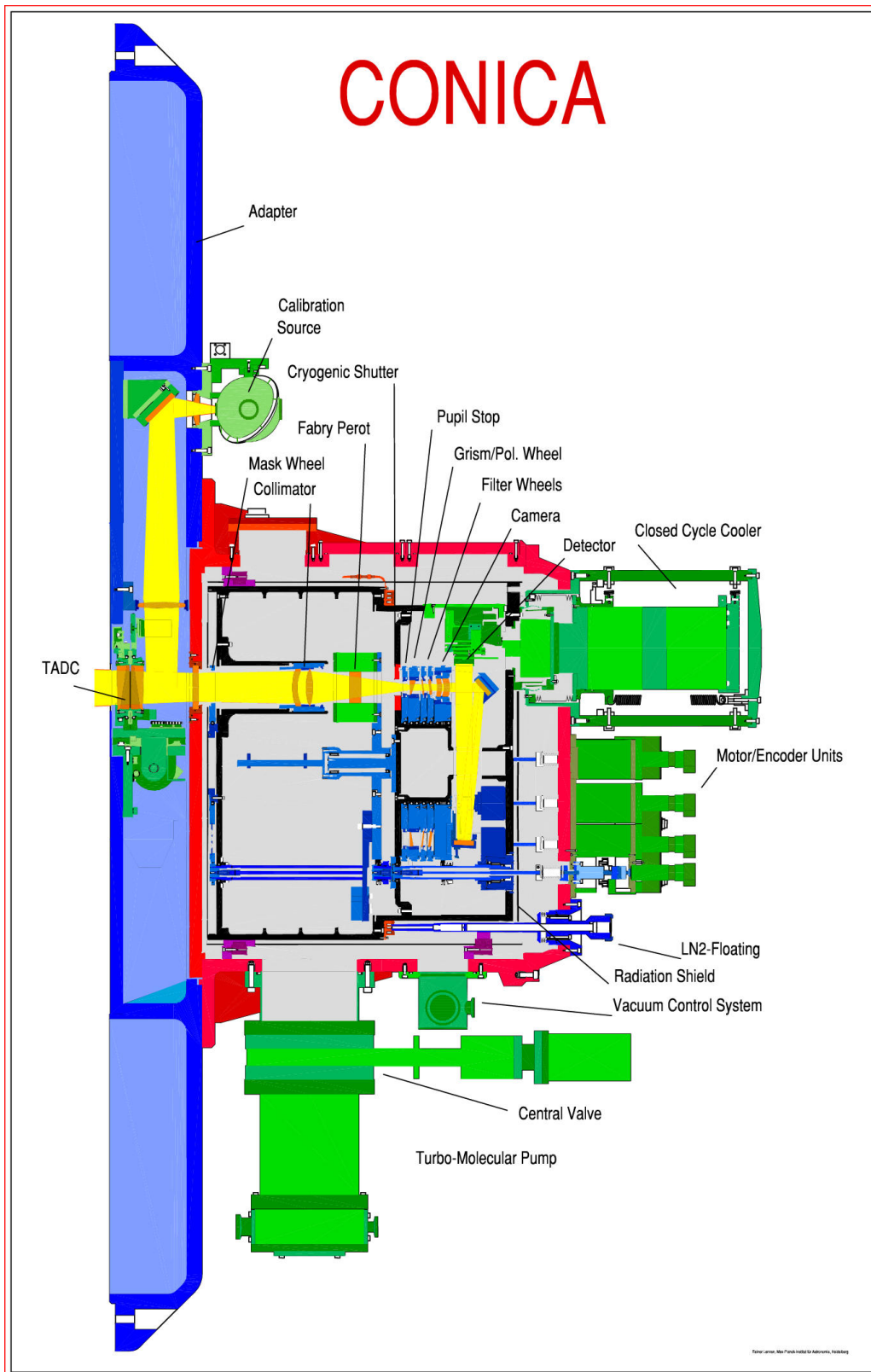


Figure 2.2: Drawing of CONICA.

2.3 NAOS

The main mechanical structure with the optical beam is depicted in Fig. 2.3 from both sides. The big cylindric excrescences house the parabolic mirrors. The essential components like tip-tilt and deformable mirror (185 actuators), the dichroic mirrors, and the parabolics shown in the overview (Fig. 2.1) can be identified. Perpendicular to the line through the parabolic mirrors, the two wavefront sensors are mounted flush through the cylindric main structure. An important issue was the optimization of the mechanical structure regarding stiffness and weight.

The field selector¹⁰ (FS) comprises two parallel mirrors mounted on high precision tip-tilt-piston stages. The mirrors can be declined to feed the selected wavefront sensor with the guide star within a 2 arcmin Field of View (FOV) and keep it fixed to a few milliarcseconds. The translatory degree of freedom in axial direction allows for a focus adjustment. The positioning accuracy and vibration suppression is highly critical for the total AO performance. The specified tasks of the FS lead to the extreme dynamical range of 100 000 and are realized by a closed-loop control of the electro-magnetic actuators (Spanoudakis et al. 2000).

The visible WFS (Feautrier et al. 2000, 2003) uses a 128^2 pixels low noise CCD¹¹ installed in a liquid nitrogen continuous flow cryostat in order to minimize dark current and readout noise. The spectral range spans from $0.45 \mu\text{m}$ to $1 \mu\text{m}$. In order to enhance the dynamics, neutral density filters can be slit in. For non-zero zenith angles, a tunable atmospheric dispersion compensator corrects the elongated PSF to ensure good AO performance. On a cryogenic translation mechanism just in front of the CCD, two micro-lens arrays are fixed providing a 14×14 and a 7×7 sub-aperture configuration. For the purpose of alignment, an open position allows one to obtain a pupil image on the detector.

The infrared WFS (Gendron et al. 2003) uses a Hawaii HgCdTe 1024^2 array. As its visible counterpart, the IR WFS is cooled by a continuous liquid nitrogen flow. The Shack-Hartmann parameters are optimized by one 14×14 and two 7×7 sub-aperture configurations. The 14×14 configuration is adjusted to point like-objects and high flux. The FOV can be tuned from 1.6 arcsec to 4.8 arcsec. The 7×7 configurations are low-flux configurations, one optimized for point-like objects (maximum FOV 2.8 arcsec) and the other for bad seeing and extended objects (maximum FOV 4.8 arcsec).

Figure 2.4 shows the performance in terms of Strehl ratio over reference star magnitude for both wavefront sensors. These measurements have been performed during the commissioning on Paranal (Mouillet and Fusco 2002, Tech. Rep.) and may serve as rough reference to estimate a performance when preparing astronomical observations. In general, the NAOS preparation software (Mouillet et al. 2003) is in charge to optimize the modes and the user may focus on his science goals.

is provided, and for the second stage at 30 K the cooling power is still 7 W. The given values are rough estimates.

⁹Ulbricht Kugel.

¹⁰Developed and manufactured by CSEM.

¹¹EEV/Marconi, 16 output ports, 500 frames/sec, 3 electrons readout noise.

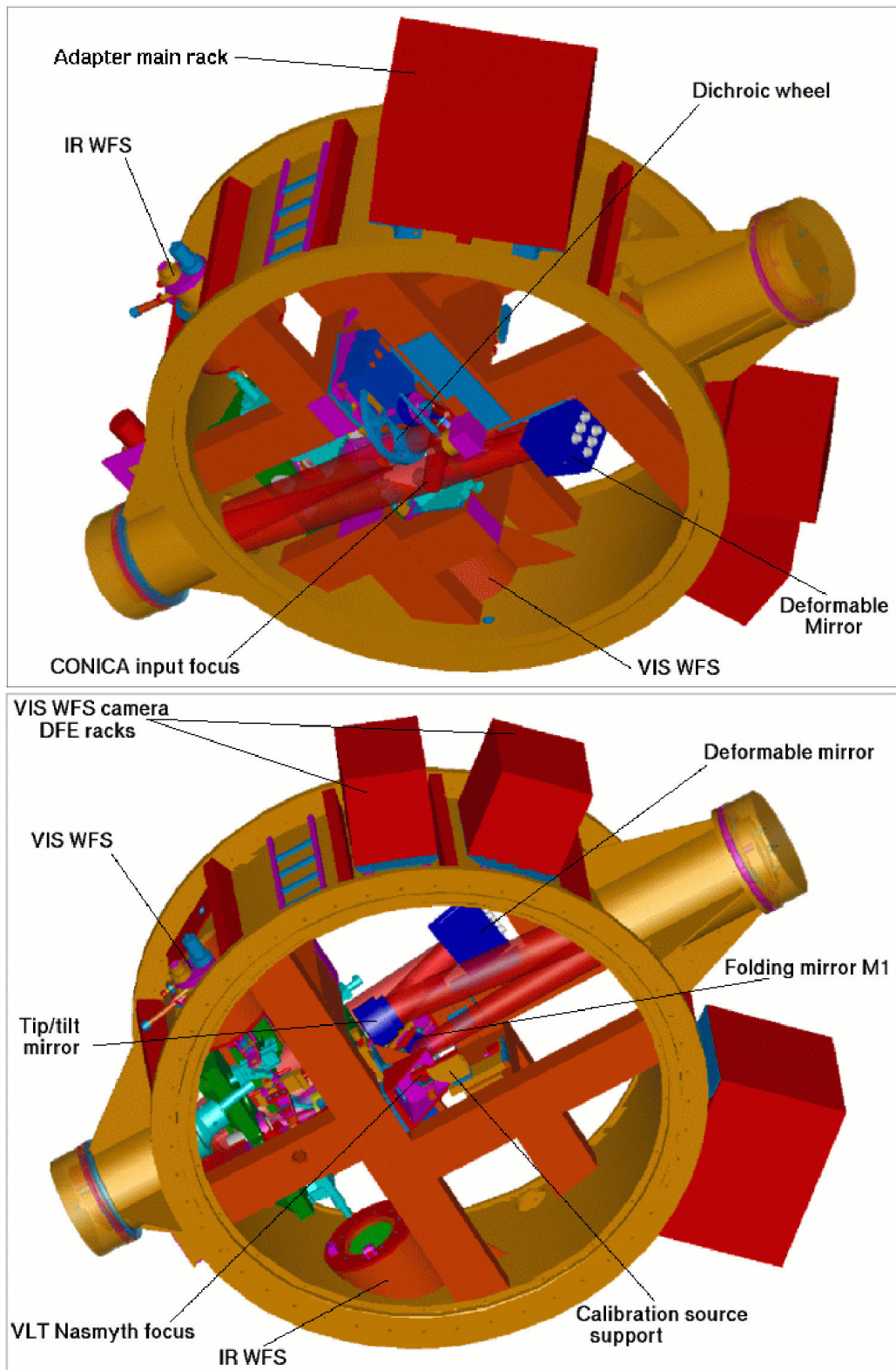


Figure 2.3: NAOS: Main mechanical structure from the CONICA side (top) and from the UT side (bottom).

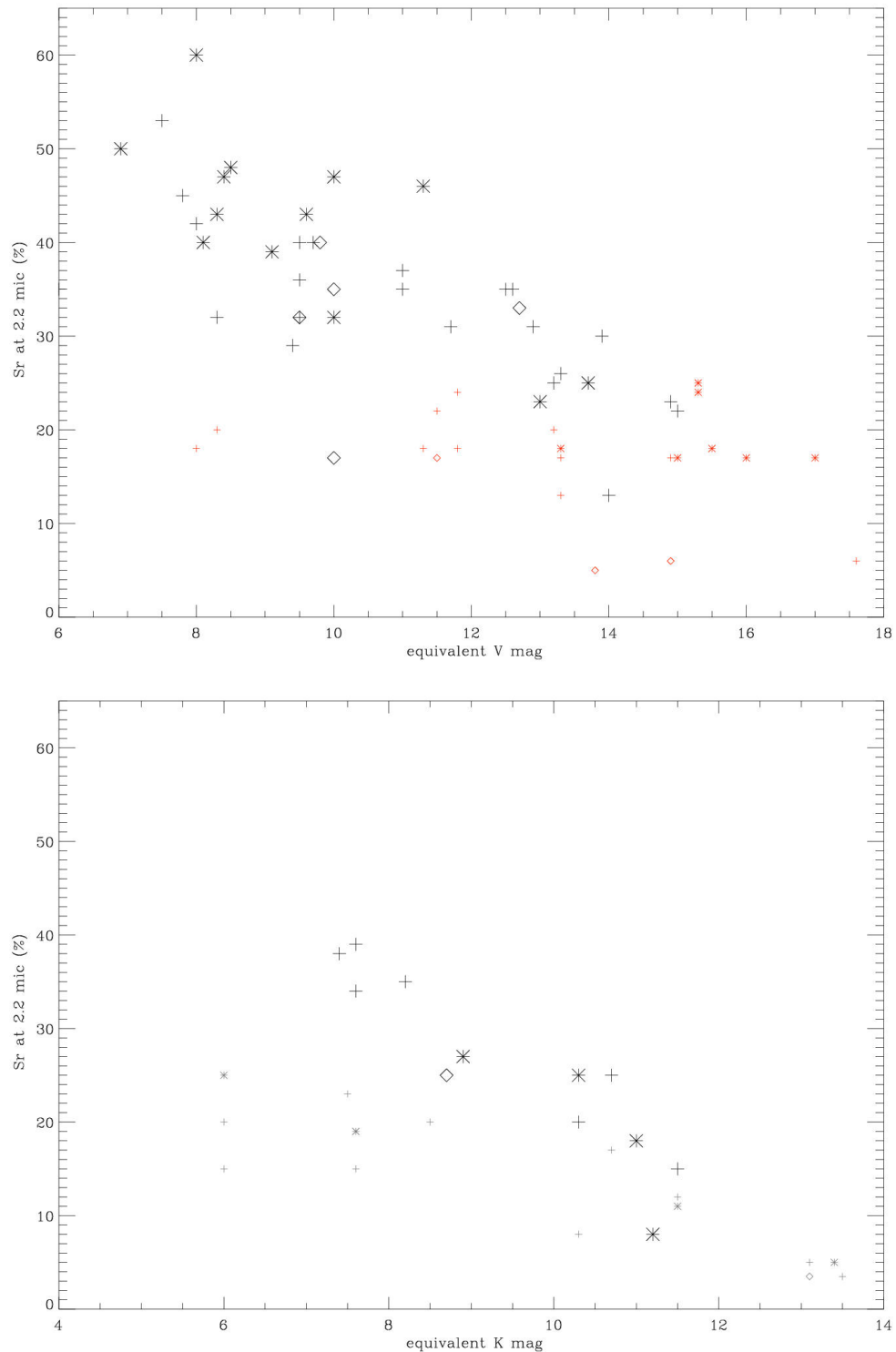


Figure 2.4: Measured SR in K-band obtained with the visible WFS (top) and the infrared WFS (bottom). The SRs are a function of guide star flux (equivalent V and K mag). The symbols indicate seeing conditions derived from the seeing monitor and corrected for airmass: stars (good seeing: ≤ 0.7 arcsec), cross (moderate seeing: ≤ 1.1 arcsec) and diamonds (poor seeing: ≥ 1.1 arcsec). Small symbols identify the use of the 7x7 lenslet array.

Chapter 3

Laboratory Tests and Calibrations of CONICA

Parts of this chapter are published in Hartung et al. (2000), *Proc. SPIE*, volume 4008, and Hartung et al. (2003), *Proc. SPIE*, volume 4841.

This chapter is dedicated to the laboratory tests and calibrations that had been performed mainly during the testing period in Heidelberg, before the instrument was integrated with NAOS in Paris. In this epoch CONICA, still a stand-alone device, was tuned and modified to fulfill the ESO specifications for the preliminary acceptance review. The product assurance verification matrix bases on the Final Design Report, a voluminous series of documents, specifying the technical and scientific parameters of the instrument regarding electronics, software, cryogenic mechanics and optics.¹ For the vast variety of specifications, it is beyond the scope of this thesis to compile them all, and we will constrain ourselves to the major items:

Flexure For all rotating instruments internal flexures are a critical item, especially for cryogenic ones, as high thermal isolation conflicts with rigorous stable mounting. A high effort was performed at CONICA to optimize the cryo-mechanical behavior. Intensive flexure measurements had been carried out with CONICA stand-alone in Heidelberg, and later on with the integrated instrument NAOS-CONICA in Paris. A short summary of the achieved performance is given in Sect. 3.1.

Instrumental background A highly critical subject arose through the internal background radiation, in particular due to CONICA's design approach to unify the short and the long wavelength channel. A series of successive improvements and modifications was undertaken to tackle the instrumental background and to fulfill the given specifications (Sect. 3.2).

Detector characteristics A review of the most important measurements to characterize the infrared array is presented in Sect. 3.3.

Throughput The overall transparency of CONICA was characterized by differential throughput measurements using a tunable blackbody source (Sect. 3.4).

¹Lenzen (1995e,d); Wagner (2001); Bickert and Tusche (1997); Lenzen (1995f, 1998, 1995b,a,g,c,j); Lenzen and Wagner (1996); Lenzen (1996, 1995i,h); Bickert (1995); Tusche (1997), Tech. Rep. and Manuals.

Optics Sections 3.5, 3.6 and 3.7 summarize some of the first laboratory results of CONICA's imaging, polarimetric and spectroscopic modes.

The Fabry-Perot Interferometer In Sect. 3.8 a detailed study of the Fabry-Perot calibrations is presented. We give a description of wavelength and order tuning, and explain the construction of the phase-shift map. For this section we make use of recent calibration data from guaranteed observing time in December 2002. The presented calibration results reflect the actual state of the Fabry-Perot interferometer.

3.1 Flexure

NAOS and CONICA are installed at a Nasmyth focus of a azimuthal telescope. Hence, the instrument has to rotate to compensate for image rotation during telescope tracking². A particular effort in design has been undertaken to eliminate internal flexure and to keep the image as stable as possible. According to the specification of the tracking performance the image must not move more than $4.6 \mu\text{m}$ in respect to the entrance focal plane for any rotation of 30 degrees or a maximum integration time of 20 min. In practice, there is a trade-off in rigidity and weight; and it is not feasible to build an instrument with such a complicated optical train stiff enough, to fulfill the hard specifications without implementing a special compensation (Granier 2001). This compensation is realized by the field selector, a high resolution tip-tilt-piston mirror device (Sect. 2.3) in the light path of the AO loop which takes over a number of important tasks:

The principal one is to select the reference star for AO correction and direct its light into the wavefront sensor. In addition, it allows closed loop tracking during dithering, counter chopping and differential object tracking in case of a moving AO reference object.

To employ the FS for flexure compensation, the pointing models for the miscellaneous observing modes (visible or infrared sensing, imaging or spectroscopy, several pixel scales) must be determined. A calibration point source of NAOS is slid into the entrance focal plane. Having closed the AO loop, the instrument is continuously turned, and a template stores the image frames over the rotation angle for both rotation directions. The relative movement of the image is extracted and yields the pointing model for the corresponding instrument configuration. The pointing model differs slightly in respect to rotation direction due to hysteresis. Hence, two pointing models have to be applied. The telescope control software (TCS) indicates the instrument control software (ICS) the actual required model. Analogously, the ICS applies the appropriate model according to its actual configuration. Exemplary, the trajectory of the pointing model for one specific instrument configuration is shown in Fig. 3.1. Fig 3.2 demonstrates the tracking performance with active flexure compensation.

3.2 Cooling and instrumental background

The inner structure of CONICA is cooled to a temperature well below 80 Kelvin to sufficiently suppress the thermal background. Cooling is performed by a closed-cycle cooler. The start-up can be accelerated with liquid nitrogen, so that the working temperature is reached within two days (Sect. 2.2). In

²A compensation of image rotation could have been implemented by an additional counter-rotating device, with the advantage of eliminating internal flexures of NAOS and CONICA, but the disadvantage to include further optical components within the beam. In particular for L and M band observations this would bring in further background sources (if not cooled) and in general the amount of light on the infrared chip at the end of the optical train would be reduced.

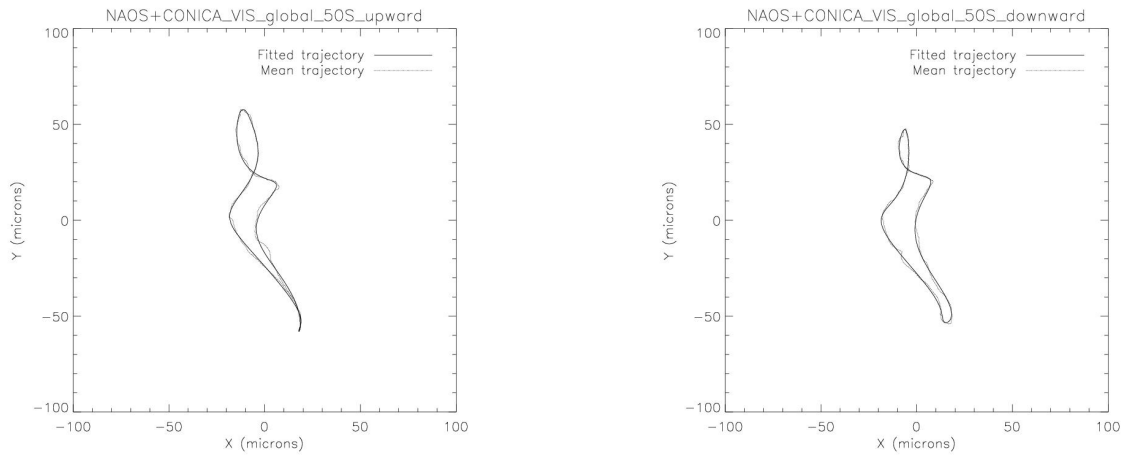


Figure 3.1: Global NAOS-CONICA tracking model for both rotation directions in closed loop with the visible WFS. The measurement was performed in the imaging mode using camera C50S.

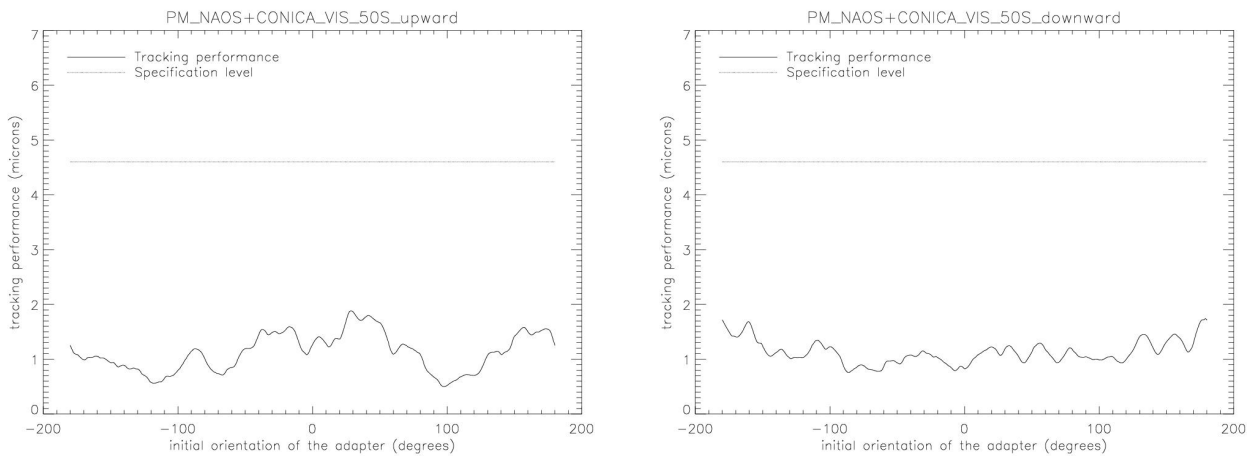


Figure 3.2: Tracking performance for both rotation directions in comparison to the specification. With active flexure compensation, the image stabilization fulfills the specification.

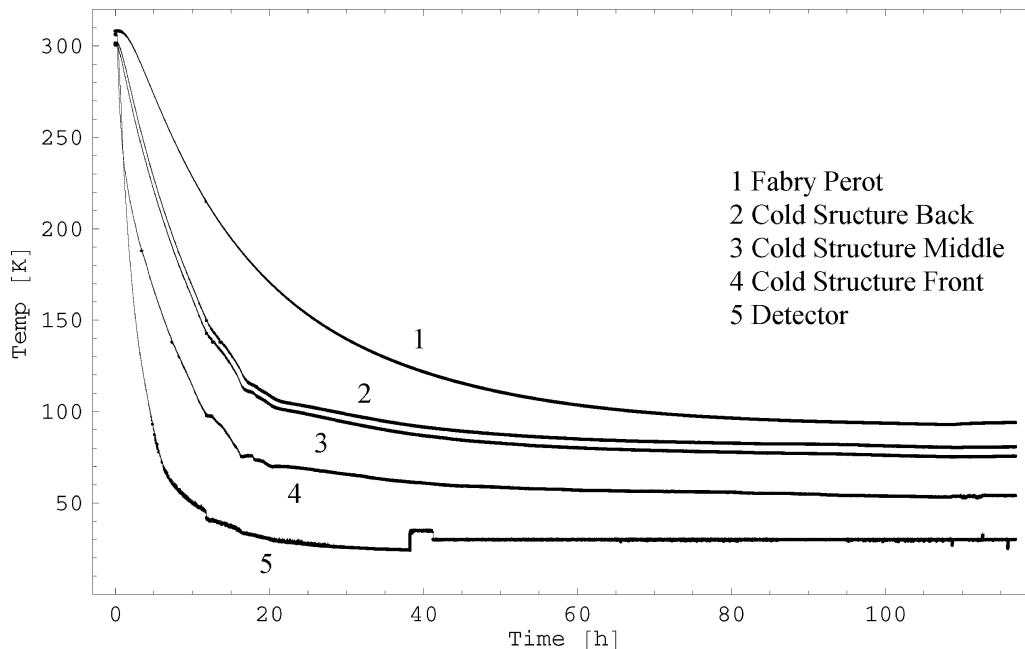


Figure 3.3: Cooling procedure: The lowest graph represents the detector temperature. The step in the detector temperature (5) at 40 h is due to a change of the set value for the operating temperature in the control loop.

Figure 3.3 temperatures at a front, middle and back position of the inner structure, as well as detector and Fabry-Perot temperatures, are logged for a typical cooling process. The cryogenic state of CONICA is permanently monitored.

The infrared detector is cooled by the second stage (Sect. 2.2) of the closed-cycle cooler. The operation temperature is stabilized by a PID-control loop³ at a value between 25 and 35 K. According to the temperature curves in Fig. 3.3, the detector is enclosed by surfaces of 55 K to 75 K. Using the quantum efficiency given in Fig. 3.4, the total thermal background load per pixel is determined. The resulting flux per pixel is expected to be well below one photon per second (Fig. 3.5).

The number of thermal photons critically depends on the cut-off wavelength of the detector sensitivity. This cut-off has been estimated by the spectral mode of CONICA. With a grism optimized for the M-Band, the external room temperature radiation illuminating the entrance slit was diffracted and imaged onto the detector. The 300 K blackbody intensity increases strongly towards longer wavelengths until it breaks down beyond $5 \mu\text{m}$. With this method we can deduce the quantum efficiency cut-off of the detector. The resulting quantum efficiency is shown in Fig. 3.4. The data for wavelengths below $5 \mu\text{m}$ are taken from Fowler et al. (1995). Our estimated data for the region from 5 to $5.5 \mu\text{m}$ were brought into line with them.

A highly critical subject arose through internal background radiation, in particular due to CONICA's design approach to unify the short and the long wavelength channel. Although different imaging

³The feedback signal is generated by weighted proportional, integrated and differential (PID) parts of the input signal.

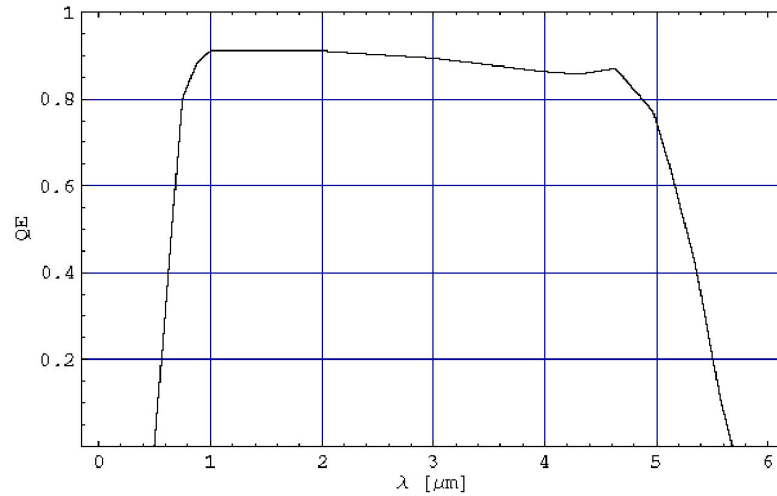


Figure 3.4: The quantum efficiency of the CONICA detector (Aladdin InSb 1024² array).

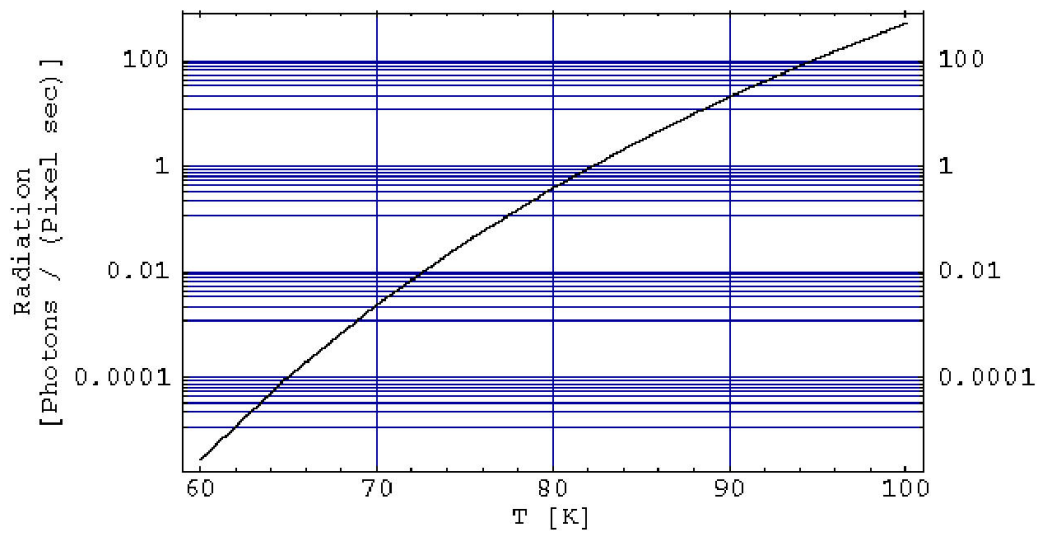


Figure 3.5: The total theoretical background load per pixel at blackbody temperature T for the detector quantum efficiency depicted in Fig 3.4.

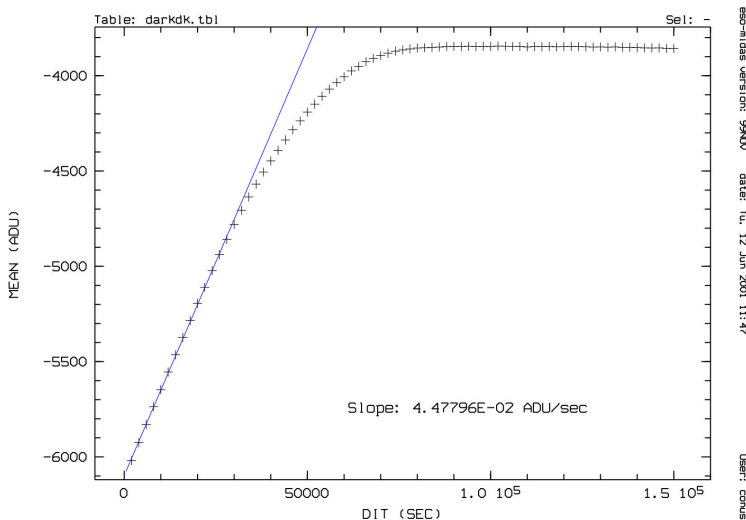


Figure 3.6: Instrumental dark measurement at 0.2 V reverse bias. Non-destructive readout every 2000 sec. Full integration time almost 42 h. The saturation level is reached after approximately 19.5 h.

optics must be used for the wavelength regime of 1 to 2.5 μm and 2 to 5 μm , only one chip covers the whole wavelength range. The advantage of a more compact design and lower cost is paid by higher constraints of the instrumental background.⁴ In the case of JHK observations the sky background is low (in comparison to L and M), thus the achievable S/N would suffer from any additional internal background signal. To prevent a restriction of imaging and spectroscopic J-band observations by instrumental background, CONICA is cooled well below 80 K. According to the specification, the dark current of the chip must not exceed 1 electron/sec. The instrumental dark signal can easily be determined by integrating in the closed position of the grism/polarizer wheel. Since the wheel is located inside the cryostat and its temperature being well below 80 K, all thermal radiation coming from the entrance window is blocked. First test measurements revealed the instrumental dark signal to be far beyond specification. The improvement of the baffles for the feed-throughs of the Closed Cycle Cooler and the focus drive, the replacement of stainless steel axles by carbon fiber axles, and the hermetic encapsulation of the fanout board brought the instrumental background down to a value below 1 electron/sec. Fig. 3.6 shows a dark integration in the uncorrelated readout mode lasting almost 42 h. Every 2000 sec the chip is read out without reset. Taking into account the appropriate detector gain (Sect. 3.3.4), the slope of the straight line yields a dark current of 0.5 electrons/sec. The full well capacity of the pixels is reached in about 19.5 h (70200 sec), having accumulated 2200 ADU. Note that the full well capacity without or with low photon flux is significantly smaller than under high flux conditions.

3.3 Detector characteristics

The eye of CONICA is the infrared detector, an Aladdin2 1Kx1K InSb array⁵, manufactured by the Santa Barbara Research Center, meanwhile Raytheon. The chip has a pixel size of 27 μm with a filling factor better than 98% and is specified with a full well capacity of 300000 electrons under 1 V reverse

⁴A complementary design is realized in ISAAC, a seeing limited NIR camera at the VLT (Moorwood 1997).

⁵The acronym stands for Advanced Large Area Detector Development in InSb.

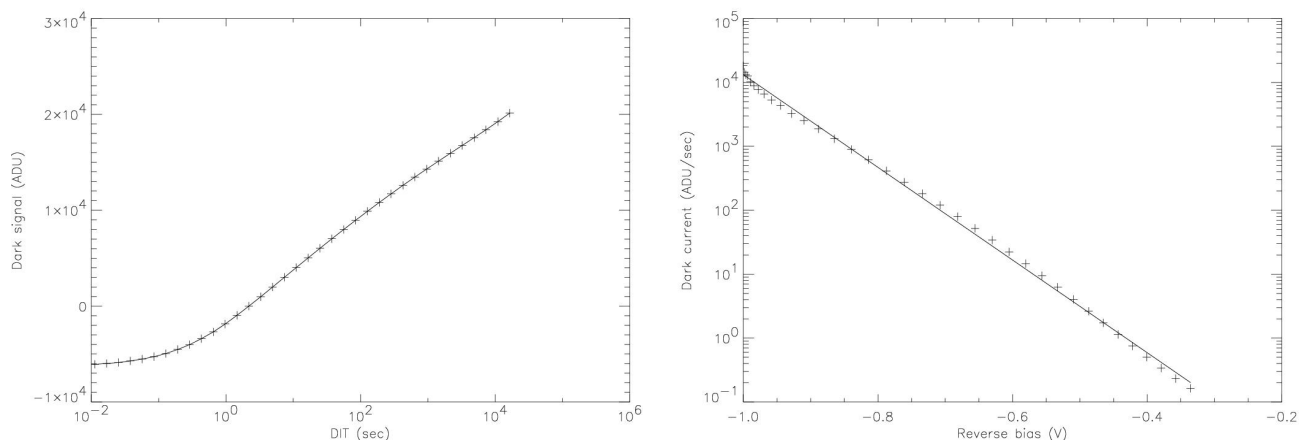


Figure 3.7: **Left:** Accumulated dark signal for exponentially increasing DITs (from 8.2 msec to 16381.5 sec). Reverse bias is set to the maximum value of 1 V. Logarithmic abscissa. **Right:** Dark current over reverse bias derived from data to the left. Logarithmic ordinate. The straight line indicates an exponentially least squares fit.

bias. Measurements show the quantum efficiency to be between 80% and 90% over the full wavelength region spanning 1 to 5 μm . The sampling technique dependent readout noise ranges from 8 to 50 electrons. The operating temperature lies between 30 and 35 K.

For a comprehensive introduction of infrared detectors in general and the Aladdin array in particular we recommend McLean (1997) and McCaughrean (1988). In both publications the astronomical application of infrared arrays is treated. In this section we present some results of the extensive investigation of the detector characteristics. In particular, we focus on those measurements concerning the adjustment of the detector for the different CONICA observing conditions.

3.3.1 Dark current and full well versus reverse bias

The full dynamic range corresponding to the full well capacity (FWC) of 300000 electrons can be accessed by putting the maximum reverse bias voltage of 1 V across the detector diodes. The dark current varies in a strongly nonlinear way with the applied bias voltage. Therefore, the price to pay for a high dynamic range is a high dark current coming along with a high number of warm pixels. Figure 3.8 gives an idea of the cosmetics for raw frames taken at different bias voltages. The frames are obtained in CONICA's cold dark configuration (closed position of the grism/polarizer wheel) with a detector integration time (DIT) of 1 sec. All shown images have the same grey scale limiting values of 0 and 2000 ADU for the minimum and maximum limit, respectively. Since we intend to compare the cosmetic behaviour of the raw frames for the different bias voltages, we do not modify the grey scale parameters. The histograms to the left characterize the warm pixel statistics. The shifted signal level due to accumulated dark electrons can be seen at higher voltages, as well.

A high detector dark current and a high number of warm pixels does *not* imply that these settings result in useless images of minor quality. But the setting has to be tuned according to the observation conditions. Usually, the photon signal in M-band observations is much higher than the signal due to

the detector dark current at high bias voltages. In Sect. 3.3.2 a nice demonstration of a cosmetically clean image for the case of an extreme dark current is given (Fig. 3.10). The proper bias setting turns out to be a trade-off between the required dynamical range and the adequate sensitivity. In case of a low photon background as in J and H-band observations or in spectroscopy, a low bias voltage setting is appropriate.

To measure the bias dependent dark current, we use the maximum reverse bias voltage and read out dark frames with an exponentially increasing DIT ranging from approximately 10 msec to 16400 sec. In the initial state the full reverse bias voltage is applied to the capacity of the depletion region. The dark current continuously discharges this capacity and the reverse bias voltage decreases. Thus, the dark current decreases as well. The pixel signal corresponds to the actual voltage at the moment of the read out. This results in a “discharge curve” shown in Fig. 3.7 at the left. Be aware that the time axis is logarithmic. We can use this discharge curve to deduce the bias dependence of the dark current, if we know the proportionality of a signal difference given in ADU and the corresponding change in voltage.

In Fig. 3.9 the FWC given by the saturation level in ADU is plotted versus the impressed reverse bias voltage (see Table 3.1). The experimental data points are obtained by integrating until saturation for the different reverse bias voltages. The flux is kept constant and amounts to about 13000 ADU/sec. Using the intersection of the regression line and the FWC for 1 V bias, we deduce a proportionality of $35000 \text{ ADU} / (1 - 0.083) \text{ V} = 38.1 \text{ ADU/mV}$.

Using this proportionality we can plot the dark current i versus the reverse bias voltage as done in Fig. 3.7 at the right. The straight line is a linear regression fit and results in the exponential function

$$i = 13200 \frac{\text{ADU}}{\text{sec}} e^{-\frac{U}{60 \text{ mV}}} \quad (3.1)$$

modelling the measured data. This formula does not describe the behaviour of the bias dependent dark current with a very high precision, but confirms the data to be consistent with a diode characteristic, and the model is by far accurate enough to choose the proper bias voltage setting and to estimate the expected dark current. At the very beginning the dark current starts at an extremely high level ($> 10000 \text{ ADU/sec}$). In the first second of integrating, the bias falls about 100 mV and the dark current reduces by an order of magnitude. The histogram at the bottom of Fig. 3.8 shows the level of integrated dark current to be about 2000 ADU after 1 sec DIT. On the other side, at bias voltages lower than 0.3 V the dark current becomes negligible and hence appropriate for observations with low photon background.

3.3.2 Cosmetics

The maximum reverse bias voltage of 1 V is not used for astronomical observations. Nevertheless, Fig. 3.10 gives a nice demonstration that cosmetically clean images can be obtained even with this extreme detector setting. The images are acquired in M-band and show a fiber with a diameter of $400 \mu\text{m}$ in the entrance focal plane of NAOS. The high photon background of the thermal infrared requires hardware windowing to lower the minimum possible DIT. All frames are taken with a DIT of 8.2 msec in the uncorrelated readout mode. From the left to the right we depict first the raw frames without and with feeding light into the fiber, and then the reduced image after correction with a dark frame and flat-fielding. Hot pixels have not been removed. Even when no light is fed into the fiber, the outlet part of the fiber and its mounting can clearly be seen in the raw frame due to thermal

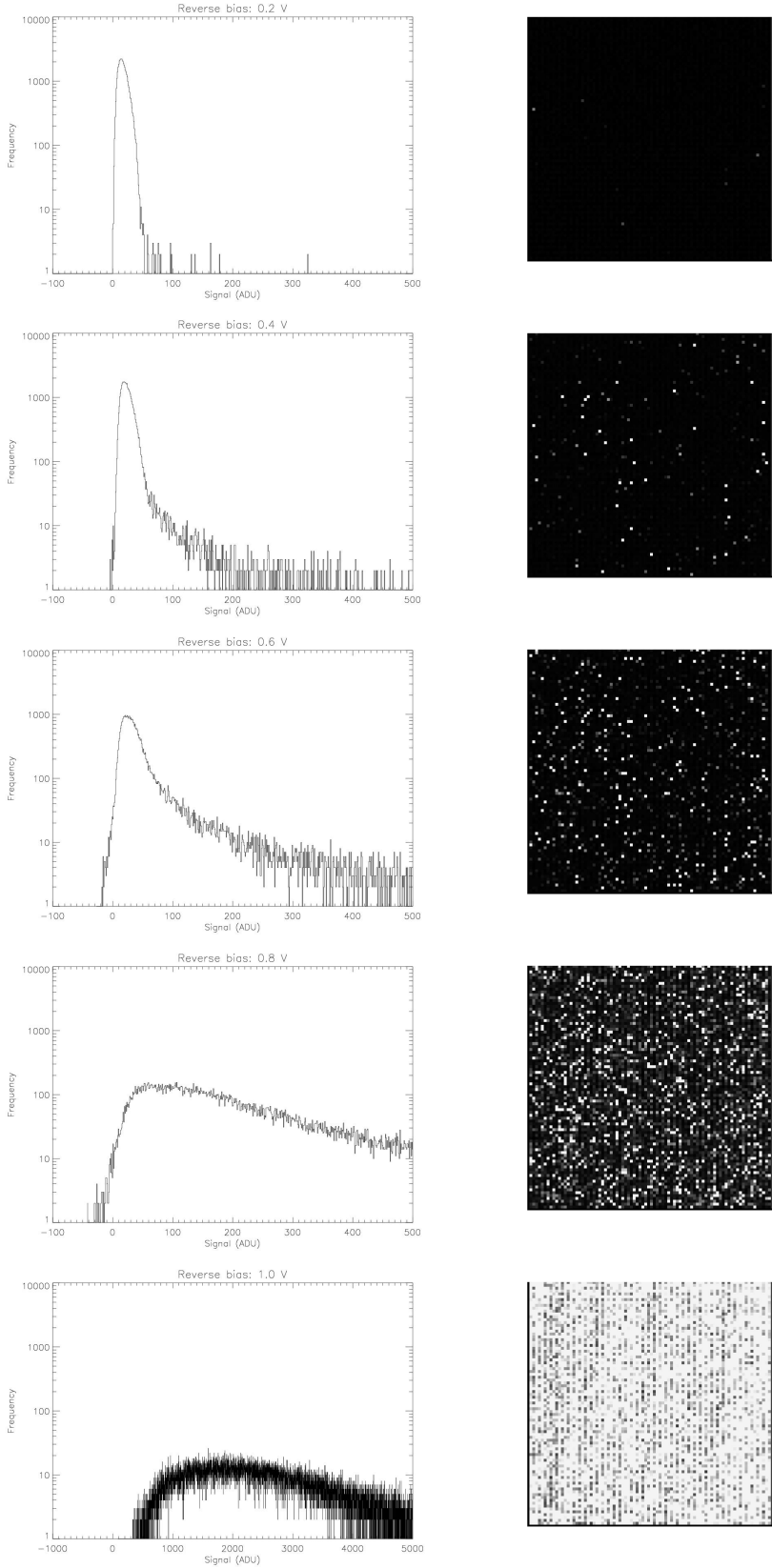


Figure 3.8: Warm pixel statistics for different reverse bias voltages at dark frames.

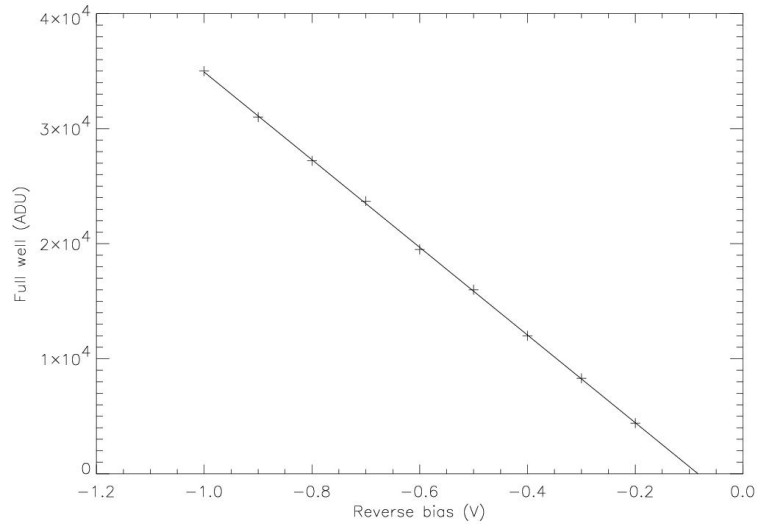


Figure 3.9: The full well capacity (level of saturation) is plotted versus the reverse bias voltage. The regression line intersects the abscissa at -0.083V . The flux amounts to approximately 13000ADU/sec . Note that the full well capacity is flux dependent.

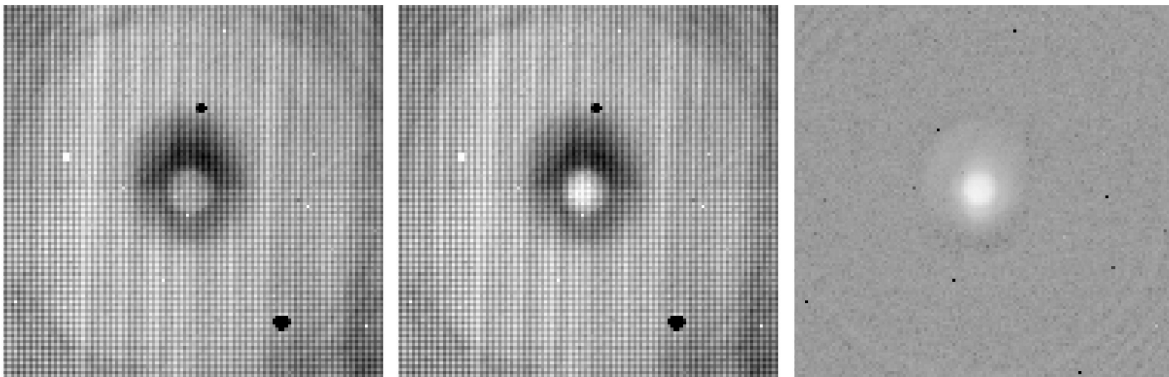


Figure 3.10: Demonstration of a cosmetically clean image at an extreme reverse bias voltage (1V). M-band image of a calibration fiber in the entrance focus of NAOS-CONICA. From left to right: Raw frame with dark fiber, raw frame with illuminated fiber, and the reduced image.

radiation. The background level of this frame reaches already about 70% (!) of the saturation level. The signal from the additional light is about 2 to 3% of the saturation level.

As a matter of fact, in case of astronomical observations the conditions would be much more moderate because of the significantly lower emissivity of the telescope mirrors and the night sky than the laboratory environment. Thus, lower reverse bias voltages are appropriate.

Table 3.1: Summary of linearity, conversion and well capacity data for the different bias voltages. RO mode: Double_RdRstRd.

Reverse Bias (V)	1% Linearity (10 ³ ADU)	5% Linearity (10 ³ ADU)	Conversion (e-/ADU)	Full Well (ADU)
0.2	< 3.3	< 3.9	12.7	4400
0.3	< 6.2	< 7.8	11.9	8300
0.4	< 8.0	< 11.1	11.0	12000
0.5	< 10.0	< 13.8	9.8	16000
0.6	< 10.8	< 15.6	8.7	19500
0.7	< 11.0	< 16.9	6.9	23700
0.8	< 11.7	< 18.2	5.3 ?	27200
0.9	< 11.8	< 18.0	(3.5)	31000
1.0	< 11.7	< 16.6	(2.2)	35000

3.3.3 Detector gain via the shot noise method

The conversion factor can be determined by measuring the signal variance with respect to the signal itself. During the measurement it must be taken care to stay in the shot noise dominated regime. This is assured in providing the right signal level and using the appropriate detector configuration voltages. This method is a standard method to determine the detector gain (conversion factor).

The variance σ_e^2 given by

$$\sigma_e^2 = N_e^2 + S_e \quad (3.2)$$

where N_e determines the readout noise and S_e the signal in electrons. This expression is transformed into Analogue Digital Units (ADU) using the dimensionless conversion factor $1/q$, which describes the ratio between electrons and counts:

$$q^2 \sigma_{\text{ADU}}^2 = q^2 N_{\text{ADU}}^2 + q S_{\text{ADU}}. \quad (3.3)$$

We solve for σ_{ADU}^2 and the equation gets into a form that the readout noise and the conversion factor q can easily be taken from the linear regression of the data points:

$$\sigma_{\text{ADU}}^2 = N_{\text{ADU}}^2 + \frac{1}{q} S_{\text{ADU}}. \quad (3.4)$$

The intercept of the ordinate yields the square of the readout noise in ADU and the inverse of the slope represents the conversion factor. Since infrared array commonly are read out in a double correlated mode, the resulting readout noise has to be divided by $\sqrt{2}$ to obtain the value for a single readout.

Even if this method allows one to determine in addition to the detector gain the readout noise, its value is usually of a low precision. A much more accurate way to determine the readout noise is its statistical deduction by a set of dark frames with small integration times (Sect. 3.3.5).

3.3.4 Conversion and linearity

The conversion (gain) from electrons to ADU is determined by the standard shot noise method that is explained above. Assuming that we are shot noise limited, we plot the signal variance over the signal

and obtain the conversion factor in ADU/e from the slope of the straight line fitting the data. The axis intercept of the ordinate yields the square of the read out (RO) noise in ADU. These values for the RO noise are indicated on the plots in Fig. 3.11, but note that in particular for high bias voltages they are not precise. The RO noise will be determined by another method described in the next subsection.

We use the CONICA calibration halogen lamp to illuminate the detector. For the whole range of possible reverse bias voltages starting at 0.2 V up to 1.0 V in steps of 100 mV we acquire a series of images with DITs ranging from 20 msec to 3 sec. The flux of the halogen lamp is kept constant. Some of these curves are shown in Fig. 3.11. The plots on the left side show simply the integrated signal over the DIT. These plots are used to determine the 1% and 5% limits of linearity. The plots on the right side use the same data, but plotted in the way described above to determine the conversion factor. The variance with increasing DIT deviates from a straight line through the origin as the FWC is approached. This is traced back to the dependence of the conversion factor on the bias voltage. In particular, this becomes significant for high bias voltages. At the end the variance data points correspond to data taken in saturation, and they drop down. The results are summarized in Table 3.1.

The dependence of the conversion on the bias voltage results from the coupling of conversion to the pixel capacity, or to be more precise, the capacity of the bias dependent depletion region in combination with the parallel constant gate capacity of the unit cell source follower. We doubt the calculated conversion factors for very high bias voltages to be right (Table 3.1). We put them in parentheses. We do not expect the conversion and thus the total capacity to change by a factor of 6. Considering the chip design, we would rather assume a maximum factor of 2 (Finger 2002). Obviously, the assumption to be shot noise dominated is not true anymore for these voltages. We can verify the consistency of such small conversion factors investigating the flux of the corresponding linearity plot (Fig. 3.11, left plot at the bottom). Although the photon flux is constant, the detected flux in ADU/sec is supposed to change with the conversion factor. The flux is expressed by the slope. Comparing the points at the origin and close to the FWC, we find a variation of the slope by about a factor of 2 and *not* a factor of 6. Hence, the values of conversion for high bias voltages are not correct.

As consequence of the investigation of the detector characteristics summarized in Table 3.1, three standard settings (detector modes) concerning the reverse bias voltage for VLT operation are defined: HighSensitivity (0.2 V), HighDynamic (0.4 V) and HighBackground (0.6 V).

3.3.5 Readout noise

The detector is readout by the ESO data acquisition system IRACE (Meyer et al. 1998). Seven different readout modes are offered: Uncorrelated (Uncorr), Double, Double.RdRstRd⁶, non-destructive (NonDest), non-destructive subpixel sampling (NonDestNsamp), a Fowler and a Fowler with subpixel sampling readout mode (FowlerNsamp). The Fowler mode is a non-destructive multiple sampling mode in which the sampling points are not distributed equally over the integration ramp, but they are located in pairs at the beginning and the end of the ramp. The number of the Fowler sampling points is determined by the parameter NDSAMP. Reasonable values range from 4 up to 64 samples, depending on the required DIT and the window size. Additionally to the multiple sampling of the integration ramp, the mode FowlerNsamp further improves the RO noise by multiple digital analogue

⁶In contrary to the common way for a correlated readout, the readout sequence is: read - reset -read.

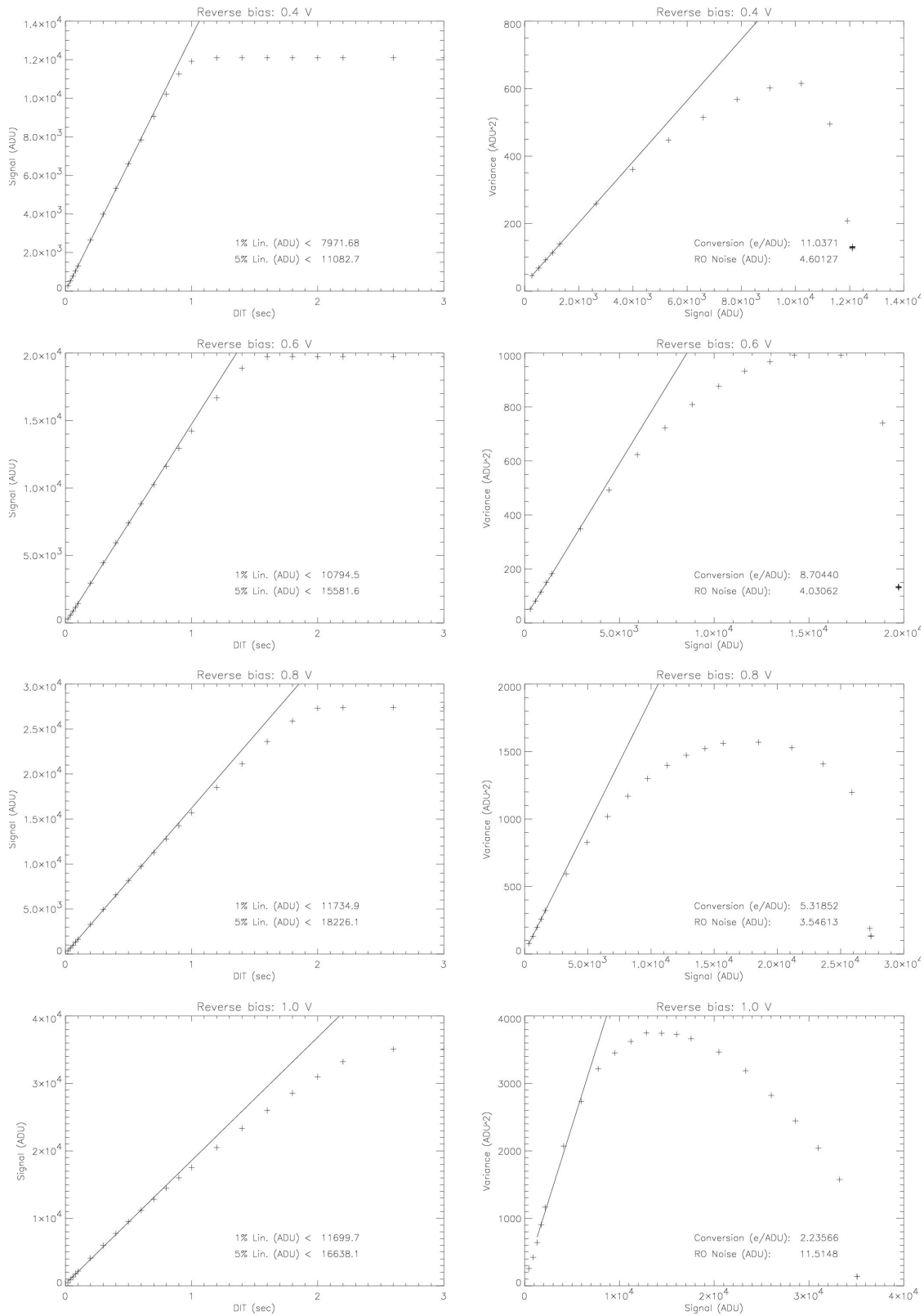


Figure 3.11: Measurement of linearity and conversion factor at different reverse bias voltages.

Table 3.2: The noise of all provided RO modes. In multiple sample modes the standard parameters are $\text{NDSAMP} = 8$ and $\text{NSAMPPIX} = 4$. They are indicated as $(\text{NDSAMP}/\text{NSAMPPIX})$.

Readout mode	RO noise (ADU)	RO noise (e)
Uncorr	5.1	65.8
Double	4.7	59.7
Double_RdRstRd	4.6	58.4
NonDest (8)	3.8	48.3
NonDestNsamp (8/4)	2.8	35.6
Fowler (8)	2.5	31.8
FowlerNsamp (8/4)	1.8	22.9
FowlerNsamp (64/64)	0.82	10.4

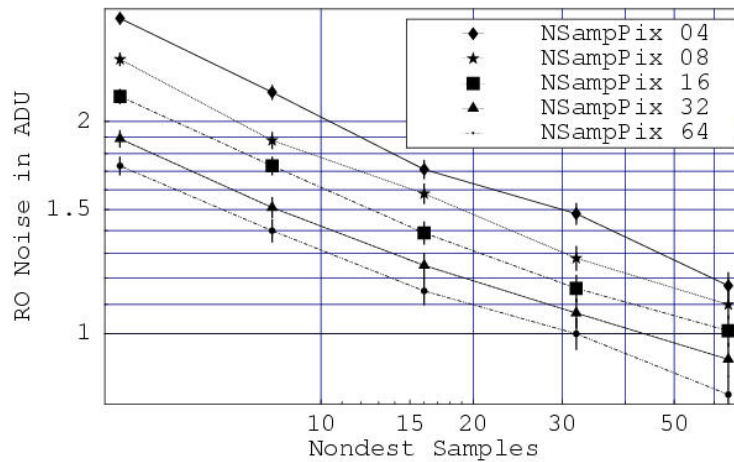


Figure 3.12: RO noise in RO mode FowlerNsamp. Reverse bias 0.2 V.

conversions. The number of conversions is determined by the parameter NSAMPPIX. Reasonable values range from 4 up to 64 conversions.

The readout noise of all modes is measured in the cold dark position. The DIT for all frames is 1 sec. Only in case that the minimum possible DIT value exceeds 1 sec, then the DIT is set to 2 sec. Small DIT values should be used to keep the dark current negligible. Be aware that for multiple sampling modes high sampling numbers will increase the minimum DIT significantly and dark current starts playing a role. For each mode the standard deviation ([STDEV??]) frame of 20 single frames is stored. A central 400x400 sub-frame is used for RO noise calculation. The mean of the STDEV frame yields the results presented in Table 3.2. The corresponding RO noise values in electrons are given, as well. Since the detector has been operated in the HighSensitivity mode (0.2 V), the used conversion factor is 12.7 e/ADU (compare Table 3.1).

A separate series of measurements has been performed to characterize the RO noise in the multiple sample mode FowlerNSamp dependent on the parameters NDSAMPLES and NSAMPPIX. Fig. 3.12 shows the behaviour of the RO noise for an appropriate set of parameters in a double logarithmic scale. DIT is set to 3 sec. This ensures the dark current to be sufficiently small not to affect the RO noise measurement. To keep the minimum DIT values for all combinations of sampling values below 3 sec, a HW window of 128x128 is applied. The RO noise is determined by a STDEV frame of 30 exposures.

In Table 3.2 the measured RO noise for the different detector modes of the Aladdin array are summarized. In addition, we observe the expected lowering of noise for the multiple sampling modes. We may annotate that the high value for the RO noise in the uncorrelated mode (Uncorr) is not astonishing. Though the frame is only readout once contrary to the other modes, an uncorrelated read out does *not* remove the kTC-noise (McLean 1997). This explains the inferior RO noise. The best value of 10.4 e is achieved in the mode FowlerNSamp.

3.4 Throughput

An important quantity of an astronomical instrument is the throughput, quantifying how many photons, that the instrument is fed with, will actually reach the detector. The aim is the highest achievable efficiency to keep the expensive integration time at the telescope as low as possible. According to CONICA's specifications, the losses due to optical components may not exceed 20% in total.

To be independent of any offset illumination⁷ we refer to a differential measurement method using a calibrated tunable blackbody source.⁸ The temperature of the surface of the blackbody source can be varied from -30°C to 120°C . The surface of the blackbody source must be placed directly in front of CONICA's entrance window and should cover the whole FOV.

For the measurement the K-filter and Camera 25S are selected. The blackbody source is tuned from 10°C to 120°C in steps of 10°C . During the measurement the environment radiation must not change. For each temperature the signal is integrated with constant exposure time. Having background corrected the raw frames with dark frames⁹ to prevent artifacts from detector features, the detected

⁷This is of particular relevance since in case of an infrared camera it is not sufficient to darken the laboratory environment.

⁸Extended area blackbody SR80 manufactured by CI-Systems.

⁹The optical train can be closed within the cryostat. By this means, we obtain "cold" dark frames.

signal is extracted in taking the mean of a central detector region. To convert the detected signal from ADU to the number of photoelectrons we need to multiply by the conversion factor. The determination of this conversion factor is described in Sect. 3.3. The conversion factor depends on the applied bias voltage of the detector and ranges between 7 and 13. In this particular case a conversion factor of 12.0 applies.

Referring to Planck's formula we can calculate the number of photons ρ emitted from a blackbody at a certain temperature:

$$\rho(T) = \int \frac{2c}{\lambda^4} \cdot \frac{1}{\exp(\frac{hc}{\lambda kT}) - 1} d\lambda. \quad (3.5)$$

Taking into account the geometric etendue¹⁰

$$G = A \cdot \Omega \quad (3.6)$$

for CONICA's specific optical setup, we can calculate the expected number of photons arriving at the detector. The surface A is given by the pixel size of the detector. The solid angle Ω is determined by the aperture diameter and the f-ratio of the chosen camera. In Fig. 3.13 the number of detected photoelectrons is plotted versus the calculated number of photons provided by the blackbody source. The slope of the regression line yields $67\% \pm 4\%$ for the total efficiency of CONICA in the K-band. The error of the detector gain may be neglected. The three highest intensity data points are excluded, since they are affected by saturation yet. All losses due to optical components as well as due to the quantum efficiency of the infrared array are included to the derived value.

Fig. 3.14 shows the data points of the same measurement, but corrected for the transmission of the K-filter and for the quantum efficiency of the detector (Fig. 3.4). Hence, the slope of the regression line reflects the transmission of CONICA in the K-band including the losses of all optical components from the cryostat entrance window to the detector. In agreement with the transmission expected from the specifications of the optical components (Lenzen 1995e, Tech. Rep.), a transmission of $87\% \pm 4\%$ is found.

3.5 Direct imaging

CONICA provides two sets of camera systems: One for the near infrared 1 - 2.5 μm region and a second for the thermal infrared region from 2.0 to 5.0 μm . Four different scales are available, each scale in both regions (Short and Long) except for the high resolution camera 50S. Scale and distortion tests and the measurement of point spread functions are performed for the different cameras.

3.5.1 Scale and distortion

An array of 17x17 100 μm pinholes served for the determination of the camera scales and the distortion. The data are plotted in a real-distance-versus-measured-distance diagram (not shown). The linear term of a second order polynom fit yields the image scale, the quadratic term is a measure for the distortion. The results that are summarized in Table 3.3 go back to the Preliminary Acceptance

¹⁰Geometric extend.

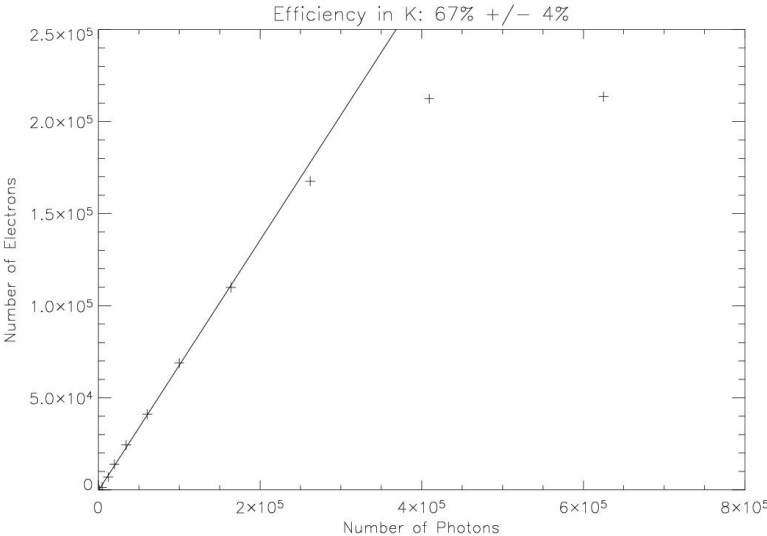


Figure 3.13: Total efficiency in K-band of CONICA.

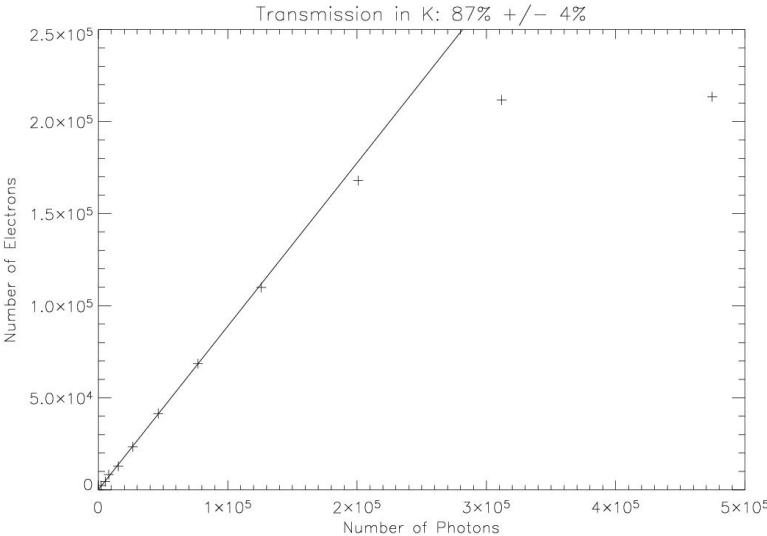


Figure 3.14: Total transmission in K-band of CONICA.

Table 3.3: Comparison of theoretical and measured values for scale and magnification. The measured distortion is given, too. Measurements for Preliminary Acceptance in Heidelberg, Spring 2000.

Camera	F-ratio	Scale (theor.) (mas/pix)	Scale (measured) (mas/pix)	Magnification (theoretical)	Magnification (measured)	Distortion (10^{-3})
50S	51.0	13.6	13.5	3.4	3.45	-0.3
25S	25.5	27.3	27.0	1.7	1.72	-0.2
25L	25.5	27.3	27.4	1.7	1.70	-0.3
12S	12.8	54.6	54.1	0.85	0.86	-0.3
12L	12.8	54.6	59.6	0.85	0.78	-0.4
06S	6.38	109.2	108.2	0.425	0.427	1.5
06L	6.38	109.2	108.9	0.425	0.430	2.5

Table 3.4: Pixel scales for all cameras measured for J and K-band. Measurements for Preliminary Acceptance Europe in Bellevue, Summer 2001.

Camera	Band	F-ratio (measured)	Scale (measured) (mas/pix)	Magnification (measured)
50S	J	52.65	13.21	3.510
50S	K	52.49	13.26	3.499
25S	J	25.77	27.00	1.718
25S	K	25.72	27.05	1.715
25L	K	25.65	27.12	1.710
12S	J	12.82	54.29	0.8544
12S	K	12.81	54.31	0.8540
12L	K	12.73	54.67	0.8484
06S	J	6.363	109.3	0.4242
06S	K	6.363	109.3	0.4242
06L	K	6.329	109.9	0.4219

Review in Heidelberg.¹¹ Theoretically expected magnifications and scales in mas/pixel are compared with the measured ones.

Table 3.4 compiles scale measurements performed just before the instrument was shipped to Paranal. For the S-cameras (short wavelength band from 1 to $2.5 \mu\text{m}$) the scales are determined for the bands J and K. The differences in scale do not exceed 0.3%.

¹¹Spring 2000.

3.5.2 Point Spread Functions

Using a $10\ \mu\text{m}$ pinhole at the entrance focal plane position a sequence of CONICA internal point spread functions were measured and compared to the theoretical point spread functions (PSF). In Table 3.5 the resulting images are compiled for different camera scales using the filters J, H, K, L and M. The PSFs are shown in a logarithmic intensity scale. The theoretical expected Airy disk (Born and Wolf 1999) radii are given by

$$r_{\text{Airy}} = 1.22 \frac{f}{D} \lambda, \quad (3.7)$$

where f/D is the focal ratio of the corresponding camera system and λ the central wavelength of the applied filter. The theoretical expected Airy disk radii are in good agreement with the measured images. Nevertheless, a naked eye inspection makes us suspect an indication of small optical aberrations seen at the shorter wavelength bands. E.g, a slight astigmatism shows up for the C12S/H-band combination, and the PSF for C25S/J-band seems to be affected by some coma. Even if the achieved SR do not violate the instruments specifications¹², we describe in Chapter 4 the method to calibrate for these remaining aberration, developed during the integration phase in France.

3.6 Long slit spectroscopy

Taking into account the conclusions of the pilot study for CONICA's spectroscopic modes conducted by Müller (1995), the instrument has been equipped with four gratings which can be combined with three different slit widths ($25\ \mu\text{m}$, $50\ \mu\text{m}$, $100\ \mu\text{m}$) depending on the required sensitivity and resolution. The four gratings are optimized for the different bands (JHKLM) within the spectral range from 1 to $5\ \mu\text{m}$. In general, the first four orders are used, even though Grating 1 diffracts up to eight orders into the field of view of the detector. The calibration is performed by means of the lines of a spectral Argon lamp (Penray), which is mounted to the integrating sphere on the adapter flange (Chapter 2). The most important Argon lines used for this calibration are compiled in Tab. A.1. Broadband filters select the spectral range to avoid overlap of different orders.

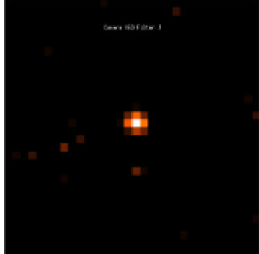
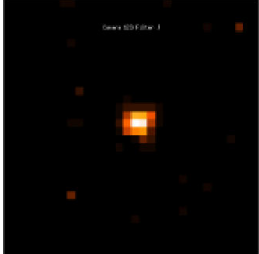
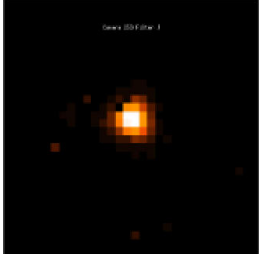
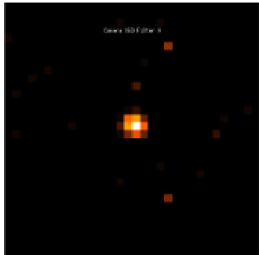
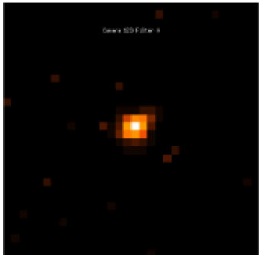
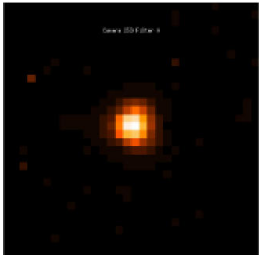
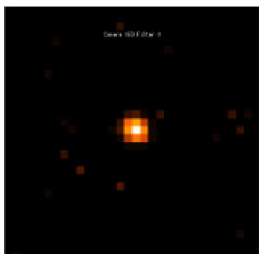
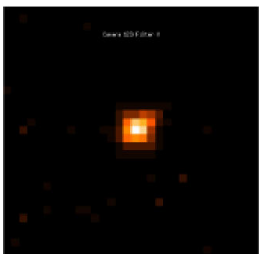
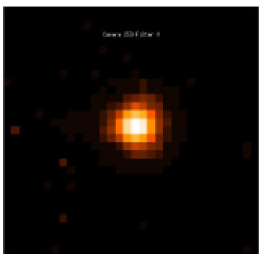
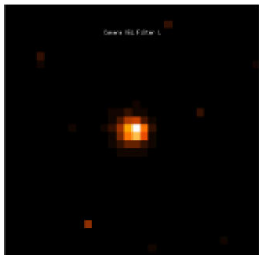
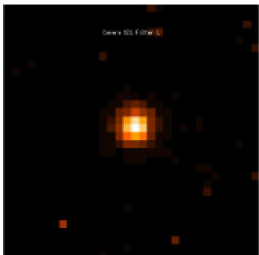
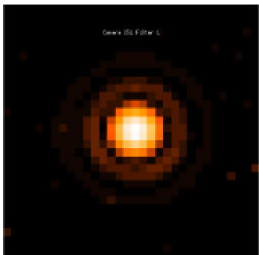
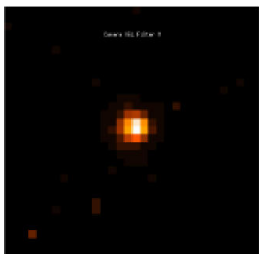
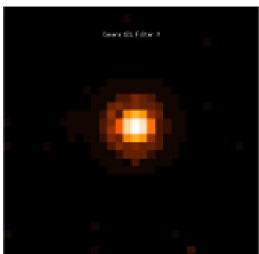
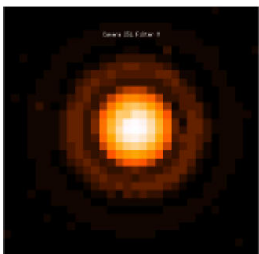
In Fig. 3.15 the calibration is performed for all four gratings in the bands J, H and K. For each band the registered Argon lines are fitted with a straight line in a pixel-position-over-wavelength diagram. The small deviation (1-2 nm) over the whole range of all three band, is explained by the variation of the refraction index with the wavelength. A fine calibration of the grating's dispersion relation including a quadratic order term is presented in Sect.3.8.2.

A rough calibration (not shown here) within the bands L and M has been performed by using adequate narrow band filters which are integrated in CONICA. For later application it is recommended to use sky absorption lines for these wavelength bands. If desired the Argon lamp can be exchanged for a Xenon lamp.

Figure 3.16 shows an example of a typical calibration line spectrum taken with CONICA. Above the detector image an intensity plot with some of the identified lines is shown. The FWHMs are varying between 1.5 and 2 pixels. In Table 3.6 the slopes of the linear regressions and their corresponding order is given. The last row illustrates the relative intensities of the spectral lines belonging to different orders as they appear on the detector. In accordance with the design of the gratings and their blaze angles, the lines near the middle of the detector are the strongest.

¹²SR > 80% in J and SR > 90% in K.

Table 3.5: A sample of registered PSFs in JHKLM using a $10\mu\text{m}$ pinhole. For JHK the S cameras and for LM the L cameras are used.

Band	Cam 06S	Cam 12S	Cam25S
J			
H			
K			
Band	Cam 06L	Cam 12L	Cam25L
L			
M			

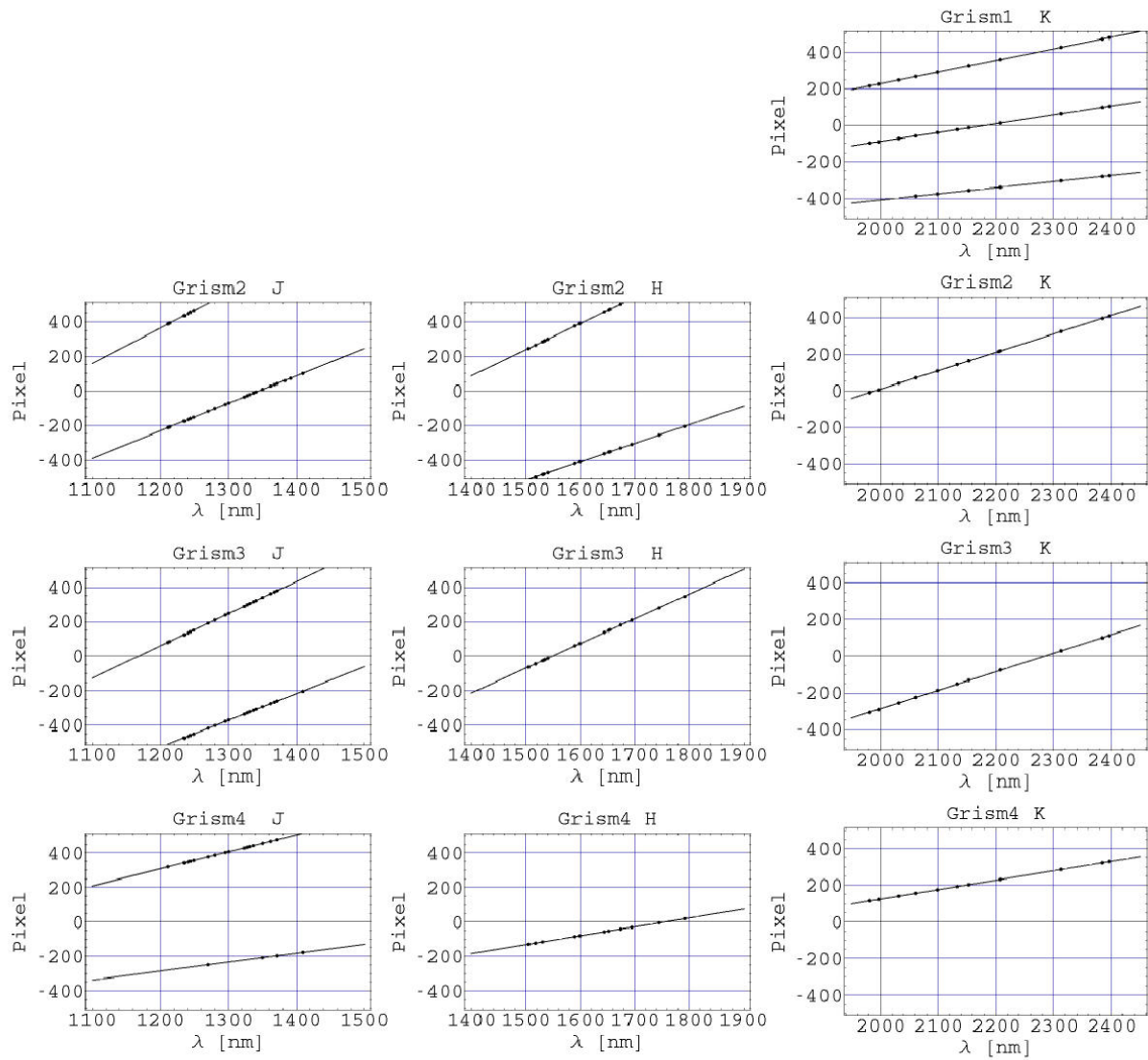


Figure 3.15: Calibration of Grism 1 to 4 in JHK. The dots are corresponding to Argon emission lines.

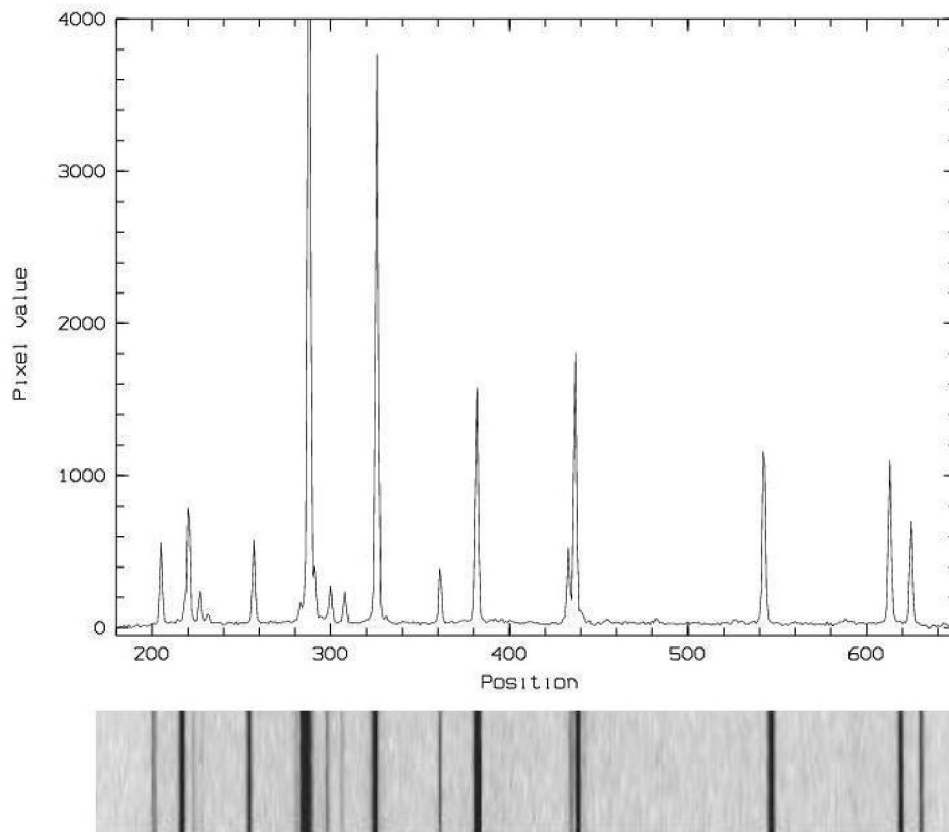


Figure 3.16: Line spectrum of grism 2 in the K-Band. The second order is visible.

Table 3.6: Summary of the grism specifications. For the different orders the central wavelengths λ_c and the resolution power $\lambda_c/\Delta\lambda$ per 2 pixel are given.

Grism	Band	Order	λ_c (nm)	$\lambda_c/\Delta\lambda$ (per 2 pix)	Slope (pix/nm)	rel. Intensity (%)
Grism 1 (optimized for LM)	K	2	3237	533	0.33	17
		3	2183	528	0.48	100
		4	1644	523	0.64	38
Grism 2 (optimized for KL)	J	3	1346	1070	1.59	100
		4	1022	1046	2.05	26
	H	2	1984	1063	1.07	93
		3	1343	1016	1.51	100
	K	2	1991	1001	1.01	
Grism 3 (optimized for HK)	J	3	1539	1195	1.55	100
		4	1168	1087	1.86	11
	H	3	1549	1106	1.43	
	K	2	2284	1155	1.01	
Grism 4 (optimized for JH)	J	1	1751	454	0.52	100
		2	889	439	0.99	4
	H	1	1756	452	0.52	
		K	1	1756	450	0.51

3.7 Polarimetry

The diffraction limited imaging mode can be combined with the application of linear polarization analyzers: Two Wollaston prisms (MgF2) are mounted into the collimated beam for providing imaging polarimetry for compact sources.¹³ Fixed positioning angles of 0° and 45° are used. For each positioning angle a corresponding stripe mask can be inserted into the focal plane to reduce the background by a factor of two for each beam. As an example, the resulting double PSF is shown in Fig. 3.17 for K and M, observed with Camera 12L through the 45° Wollaston prism. The beam splitting has been measured all over the region of sensitivity. As shown in Fig. 3.18, the result coincides nicely with the expected one if the measured imaging scale is taken into account. For extended sources, alternatively the wiregrid analyzers can be used. The imaging quality of these filters has been checked.

A more extended study of CONICA's polarimetric modes had been performed during Commissioning and Science Verification at Mount Paranal (Ageorges et al. 2002).

3.8 The Fabry-Perot Interferometer

CONICA is equipped with a cold, tunable Fabry-Perot Interferometer (FPI) manufactured by Queensgate Instruments Ltd. (1995, Manual). This is a rather unique sub-device.¹⁴ The FPI is mounted in

¹³A pilot study of CONICA's polarimetric is found in Müller (1995).

¹⁴Meanwhile, this type of ready-made, cryogenic tunable Fabry-Perot is not produced anymore by Queensgate.

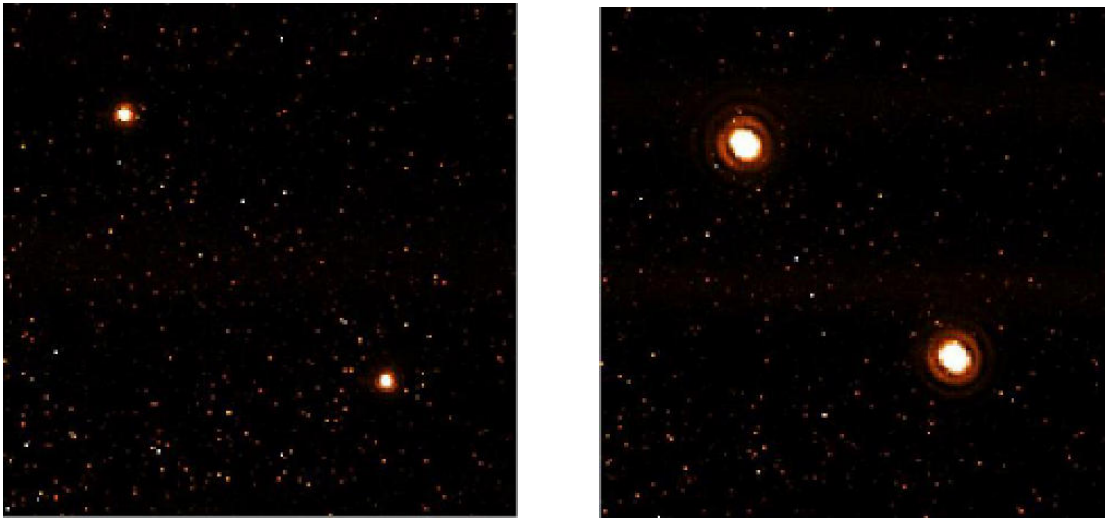


Figure 3.17: Image of a $10\ \mu\text{m}$ pinhole by camera 12L applying the 45° Wollaston prisma in K and M.

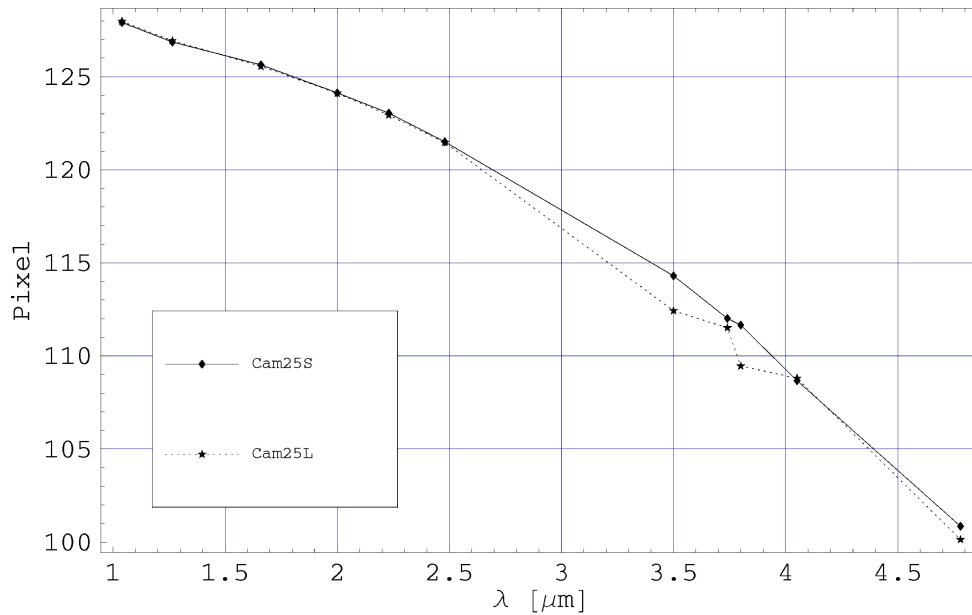


Figure 3.18: Beamsplitting of 45° Wollaston prism imaged by cameras 25S and 25L corresponding to the wavelength region. To allow for a direct comparison of the curves, the pixel scales of camera C25S and C25L are corrected.

the collimated beam, and can be tuned in the K-band. The spectral resolution is approximately 1100 and the best finesse reaches 33 (Klare 1996). A summary of test results, performed before the FPI was mounted into CONICA’s cryostat, can be found in Klare (1996).

3.8.1 Principles

The theory of Fabry-Perot interferometers is based on multiple reflections at planar surfaces (Born and Wolf 1999). The transmission is described by the Airy formula:

$$\frac{I_t}{I_i} = \frac{1}{1 + F \sin^2 \frac{\delta}{2}}, \quad (3.8)$$

where I_i and I_t denote the intensity of the incoming and the transmitted beam respectively. The quality of the spectral separation is described by

$$F = \frac{4R}{(1 - R)^2}, \quad (3.9)$$

with R being the reflectivity of a simple plate. The phase shift δ is given by

$$\delta = \frac{4\pi}{\lambda} n d \cos \theta, \quad (3.10)$$

where λ represents the wavelength, n the refractive index, d the plate thickness (or separation), and θ the inclination angle. The finesse

$$f = \frac{\pi\sqrt{F}}{2} \quad (3.11)$$

measures the ration of the separation of two peaks from adjacent orders to their FWHM (Fig. 3.21). Since the distance between two adjacent orders decreases with increasing order, the finesse will drop with increasing order, too.

3.8.2 Wavelength and order calibration

The astronomer who selects the observing wavelength λ needs to know at what order m the FPI provides the best performance, and what plate separation d he needs for an optimal scan of the FOV (Hartung et al. 2000, 2002b). The FOV must be scanned because of the inclination dependent interference condition, i.e., only a ring-shaped part of the FOV is transmitted for a selected wavelength. Hence, care must be taken regarding the sampling of the wavelength channel as well as the completeness of the data cube. A spatial calibration of the phase-shift dependence for the whole FOV is undertaken via a phase map. The construction of the phase map and its application on a set of calibration data is explained later on (Sect. 3.8.3).

To calibrate the wavelength dependency of the plate separation d (controlled with the “ z -value” given in Fabry-Perot Control Units (FCU)), we direct continuum light into the 86-mas Slit dispersed with Grism 3. Undesired orders from the grism are suppressed by the K-band filter, and we use Camera 25S (27 mas/pix) for a higher sampling. Switching in the FPI will cut out the images of the slit according to the interference condition for a parallel beam:

$$m\lambda = 2d. \quad (3.12)$$

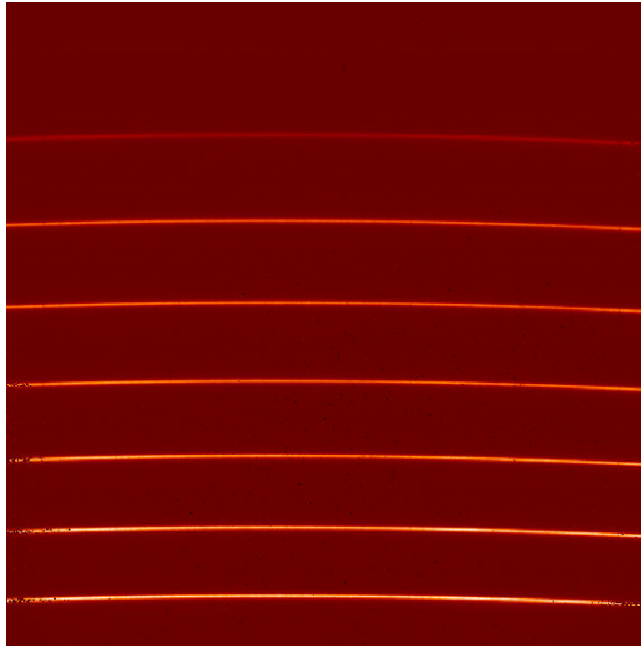


Figure 3.19: An example frame from the calibration cube to determine the relation between wavelength and plate separation. The direction of dispersion is vertical. The image of the entrance slit is seen in seven successive orders ranging from $m = 33$ (top) to 40 (bottom). Increasing the plate separation during the scan will shift the lines further upwards and higher orders will appear from the bottom. The bending of the lines is due to the phase shift at different inclination angles. *Instrument configuration: C25S, Slit 86 mas, Grism 3, FPI in ($z = 0$), K-filter. Illumination with continuum light.*

In this configuration, a set of exposures for different z -values forms the calibration data cube. An example frame from this data cube appears in Fig. 3.19. With this camera scale, typically six to eight different orders can be seen. The image is taken at $z = 0$ position, in the middle of the Fabry-Perot's tuning range. The slight bending of the dispersed slit images is due to the phase shift, according to the interference condition dependent on the inclination angle (Eq. 3.10). The higher the inclination angle, the shorter the wavelength which the FPI transmits.

First, we want to focus on the calibration of the $\lambda(z)$ -relation for the perpendicular case (zero inclination angle). Since the FPI is very sensitive to small wavelength shifts, we need to refer to a precise grism calibration.

3.8.2.1 Fine calibration of the Grism's dispersion relation

An exhaustive reference of Argon I lines can be found in Whaling et al. (2002). Some prominent Argon lines that are important for the calibration of CONICA's long slit spectroscopy modes are compiled in Table A.1. Vacuum wavelengths must be applied, since spectral analysis occurs in CONICA's cold and pumped cryostat.

A reliable calibration of the FPI depends on an accurate calibration of the grism dispersion. The precision of describing the grism dispersion by a linear model is not sufficient for the FPI calibration. Fig. 3.20 demonstrates the residual deviations for a linear model. Here, maximum systematic errors of up to 1 nm are to be expected. The residual is obviously due to a square term. In Tab. 3.7 both the

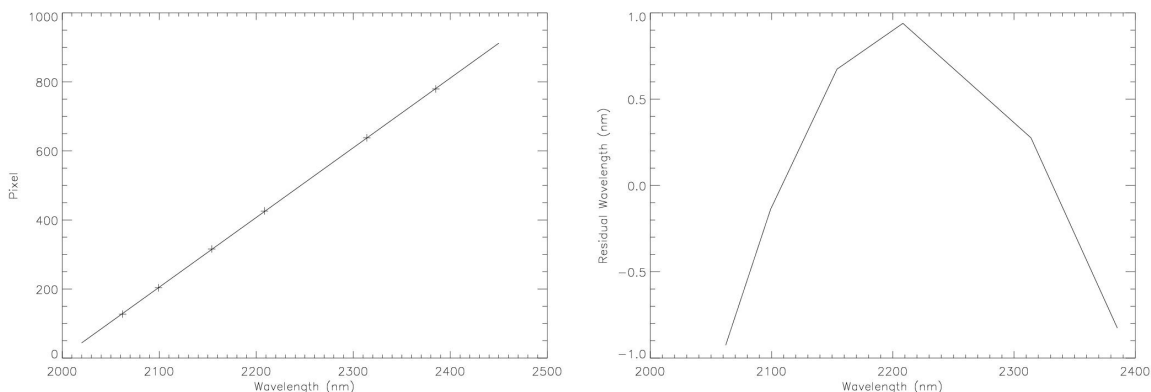


Figure 3.20: Linear grism calibration (left) and its residual deviation (right). *Grism 3, K-Filter, C25S*.

Table 3.7: Comparison of linear and square modelling for the grism dispersion (Grism 3, C25S). The position y is given in pixel units and λ in nm.

Model	1σ error
Linear fit: $\lambda = 1998.15 + 0.495226 y$	0.77
Square fit: $\lambda = 2220.06 + 0.495065 (y - 450) + 1.71885e-5 (y - 450)^2$	0.05

linear and the squared model are shown together with their residual errors. By describing the grism dispersion with a quadratic model, the error drops to 1/500 of a nanometer. The remaining residual deviations are randomly distributed.

3.8.2.2 Finesse

The finesse is directly determined from the calibration data set. We use one frame in the middle of the scan region. Towards the limits of the scan region, we might expect a somewhat lower finesse, since a possible plate alignment error increases towards the limit positions of the piezo stage. Taking the frame with $z = 0$ (Fig. 3.19) from the calibration data cube, we extract the spectral information for two neighbouring orders, at both edges of the accessible spectral regime. Comparing Fig. 3.19 and Fig. 3.22, we can determine the orders: 35 and 36 for the pair of orders at the top, and 39 and 40 for the pair of orders at the bottom. To determine the proper FWHM of the peaks, we have to take into account the convolution with the spectral response. The spectral response is measured using a reference spectrum with the same scale. The Argon line at 2062.2 nm is selected to determine the FWHM. This line width is negligible with respect to the spectral response of the instrument and can be regarded as a delta function. The wavelength FWHM ϵ of the instrumental response (*86-mas Slit, C25S*) is:

$$\epsilon = 1.4 \text{ nm} \hat{=} 2.9 \text{ pix} \quad (3.13)$$

Approximating the spectral peaks with Gaussians, the relation

$$\eta_{conv}^2 = \eta_{deconv}^2 + \epsilon^2 \quad (3.14)$$

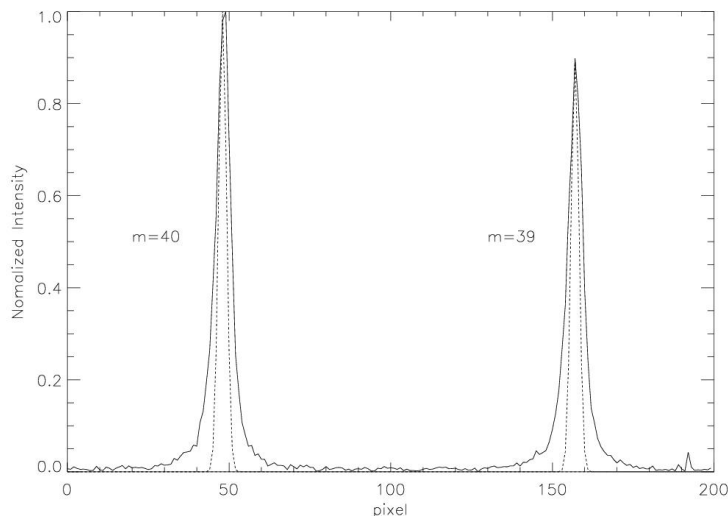


Figure 3.21: A vertical cut extracted from the spectrum in Fig. 3.19. The highest visible orders 39 and 40 are shown. The dotted line represents the spectral response of this long slit configuration (*Slit 86 mas, Grism 3, C25S*). 1 pixel (27 mas) corresponds to 0.50 nm. It is obvious that the spectral response may not be neglected in determining the finesse of the Fabry-Perot.

Table 3.8: Determination of the range of the finesse. FWHM given after deconvolution.

Order	FWHM (pix)	Separation (pix)	Finesse
33	4.78	109.0	23.6
34	4.93		
39	5.54	136.5	22.5
40	6.02		

serves to determine the FWHM η_{deconv} of the deconvolved peak. To determine the finesse, each FWHM of the pairs of peaks is averaged (Tab. 3.8). A dotted line in the enlarged cut of the spectrum shown in Fig. 3.21 demonstrates that the instrument response may not be neglected in determining the finesse.

3.8.2.3 Calibration of FPI Scan Units

With the grism dispersion calibrated properly, we can extract the wavelength belonging to the different orders. This has to be done for each frame of the data cube. The data cube contains the scan positions ranging from $z = -800$ FCU to $z = +800$ FCU in steps of 100 FCU. We extract the wavelength information in the center of the FOV, to avoid any inclination of the beam passing the FPI. Inclination introduces an additional wavelength shift, since the interference condition changes (see Eq. 3.10, Eq. 3.20 and Fig. 3.19). To assign the correct order to the extracted wavelength, we calculate a number of regression lines for different hypothetical values of m_0 , whereby the n extracted wavelengths are denoted by λ_0 through λ_n . Then we can find the m_0 that fulfills

$$\lambda_n \cdot m_0 = \lambda_{n-1} \cdot (m_0 + 1) = \lambda_{n-2} \cdot (m_0 + 2) = \dots = \lambda_0 \cdot (m_0 + n) \quad (3.15)$$

Table 3.9: Calibration of plate separation. Only frames from $z = -500$ FCU to $z = +500$ FCU are used. Phase jump is not corrected.

$\lambda(z) = a + b \cdot z$		
Order	a (nm)	b (nm/FCU)
34	2400.72	0.169535
35	2331.93	0.165318
36	2266.74	0.160888
37	2205.04	0.156624
38	2146.58	0.152577
39	2091.09	0.148728
40	2038.36	0.145114
41	1988.16	0.141695

Table 3.10: Calibration of plate separation. Only frames from $z = -500$ FCU to $z = +500$ FCU are used. Phase jump is corrected. Compare with Table 3.9.

$\lambda(z) = a + b \cdot z$		
Order	a (nm)	b (nm/FCU)
34	2398.96	0.168556
35	2330.62	0.164304
36	2265.88	0.159812
37	2204.63	0.155466
38	2146.62	0.151353
39	2091.59	0.147453
40	2039.29	0.143840
41	1989.51	0.140441

with the least square deviation. This ‘order fitting’ is repeated for each of the scan frames. From frame to frame, the orders shift successively upwards (Fig 3.22). Now, we can determine for each order a linear relationship between z and λ using a regression line. These regression lines are plotted in Fig. 3.22 (top).

The same procedure is repeated confining ourselves to a smaller scan region. The corresponding regression lines are plotted in Fig. 3.22 (bottom), and Tab. 3.9 summarizes their parameters. Fig. 3.23 compares the derived plate separation using all frames of the scan ($z = -800$ FCU to $z = +800$ FCU) with that using the smaller scan region ($z = -500$ FCU to $z = +500$ FCU), centered in the accessible tuning range.

The striking improvement in the deviations of the derived plate separation strongly suggests that we confine ourselves to the central scan region, thereby yielding a much more consistent separations for the different orders. Obviously, when scanning beyond $|z| > 500$, we leave the linear region of the piezo stack control.

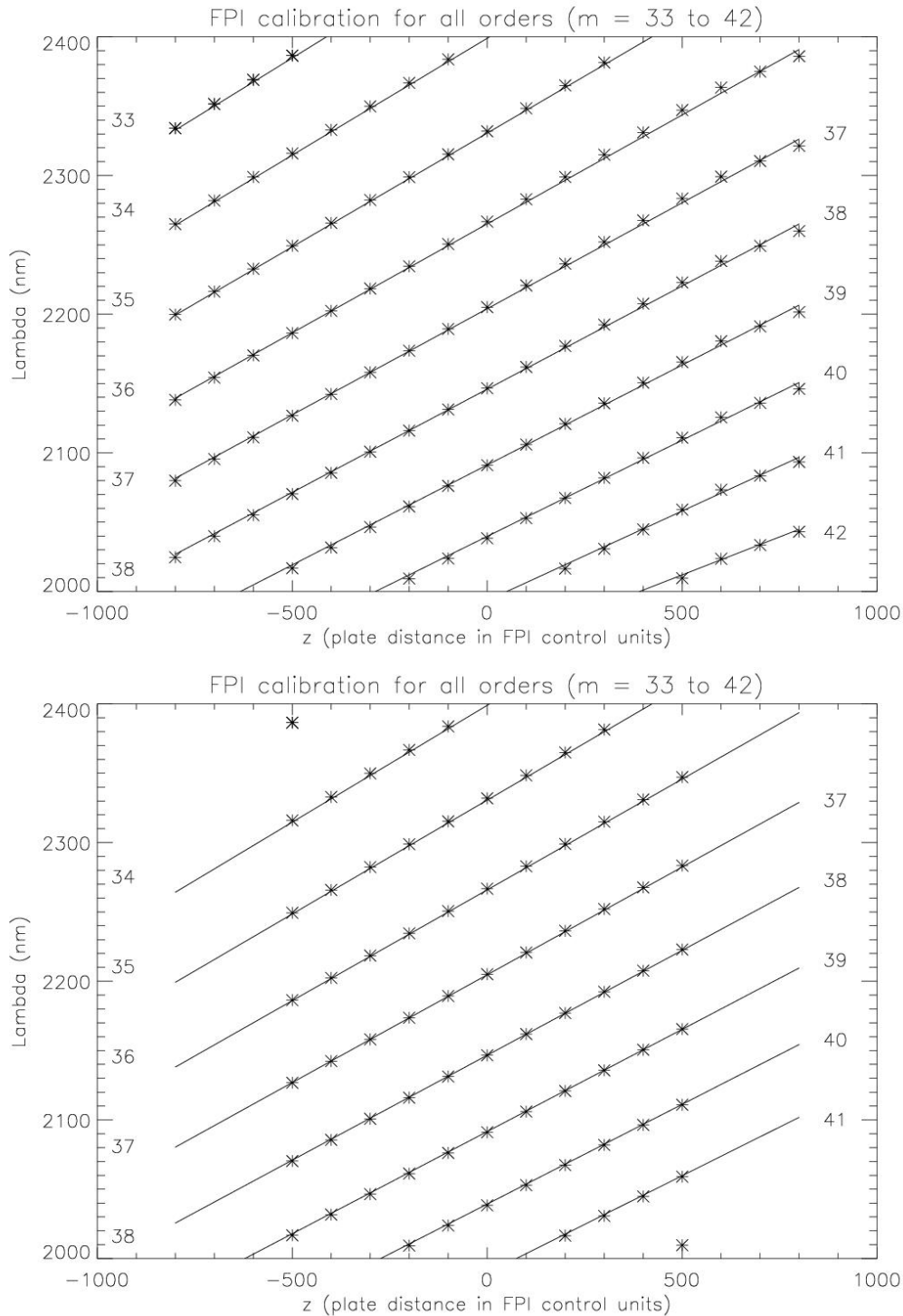


Figure 3.22: FPI calibration of all orders using scan frames ranging from $z = -800$ FCU to $z = +800$ FCU (top) and from $z = -500$ FCU to $z = +500$ FCU (bottom). The wavelengths of each line from the individual frames is extracted, assigned to its order and plotted versus the z -separation. Each set of vertical wavelengths corresponds to one frame of the (x, y, z) -cube.

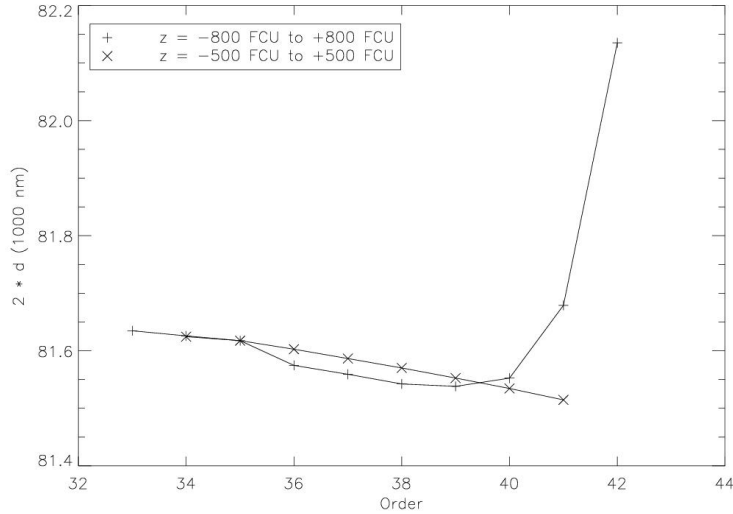


Figure 3.23: The plate separations derived from the regression parameters for different orders (compare with Fig. 3.22) are plotted versus their order. This is done for the regression lines determined over the total scan region (-800 FCU to $+800$ FCU) and over a smaller scan region in the center of the tuning range (-500 FCU to $+500$ FCU). The strong deviation of the plate separations from a horizontal straight line for the first case is caused by a non-linear behaviour of the piezo stage approaching its limit positions. The small residual deviations in the second case reveal the wavelength-dependent phase jump occurring during the multiple reflections within the cavity.

3.8.2.4 The phase jump correction

The plate separation derived from different orders is expected to be independent of the order (Eq. 3.12). Even if we constrain ourselves to a smaller scan region (Fig. 3.23), a slight monotone drop remains, so the determination of the plate separation seems to be order dependent. The same data points shown in Fig. 3.23 are re-plotted in Fig. 3.24 substituting the order by the corresponding wavelength at $z = 0$. The mean separation is subtracted to point out the residual deviation from a constant. This residual deviation is of the order of 100 nm for the whole wavelength region, or approximately $\pm 2.5\%$ deviation from the central wavelength. This effect is explained by a wavelength dependent phase jump in the complex coating of the FPI plate surfaces:

$$m \cdot \lambda + 2\delta(\lambda) = 2d = ma + mb \cdot z, \quad (3.16)$$

where $\delta(\lambda)$ describes the effective total phase shift per plate, which may involve multiple reflections. To enhance the precision of the z -calibration, we shall model this effect and take it into account. Using a second-order polynomial, a good model is

$$2\delta(\lambda) = \alpha \cdot (\lambda - \lambda_0) - \beta \cdot (\lambda - \lambda_0)^2, \quad (3.17)$$

with its parameters summarized in Tab. 3.13. Correcting the parameters shown in Tab. 3.9 with the wavelength-dependent phase jump, produces the results in Table 3.10.

Having modelled the small effect due to the phase jump, we express the calibration results independent of the order. Therefore, the parameters a and b in Tab. 3.10 are multiplied by the corresponding

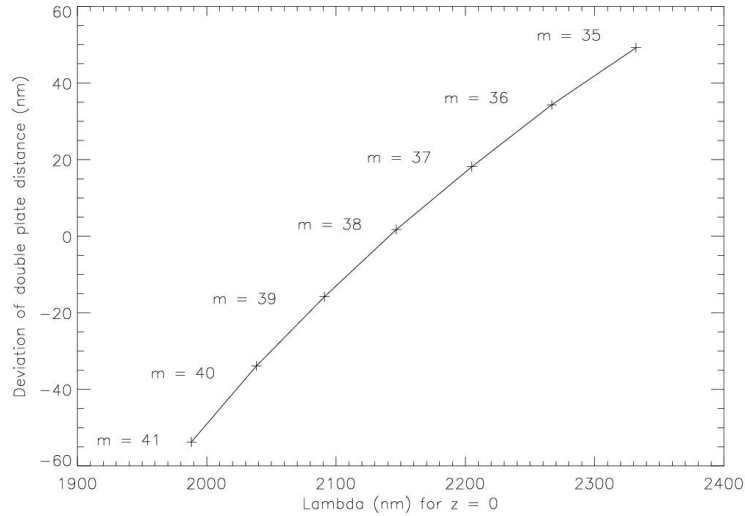


Figure 3.24: The plate separation determined via the regression line parameters for different orders plotted versus wavelength. The small deviation from a horizontal straight line is explained by a wavelength-dependent phase jump occurring in the FPI coating during the multiple reflections within the interference spacing.

Table 3.11: The order dependence of the results of Table 3.10 is removed by multiplication with the corresponding order. To indicate the difference, the corresponding coefficients are labeled with upper case letters.

Order	$m \cdot \lambda(z) + \delta(\lambda) = A + B \cdot \lambda$	
	A (nm)	B (nm/FCU)
34	81564.6	5.73090
35	81571.7	5.75064
36	81571.7	5.75323
37	81571.3	5.75224
38	81571.6	5.75141
39	81572.0	5.75067
40	81571.6	5.75360
41	81569.9	5.75808

Table 3.12: Error of z -calibration with and without correction for the phase jump (PJ).

	A (nm)			B (nm/FCU)		
	max - min	σ	σ_{rel}	max - min	σ	σ_{rel}
Without PJ correction	110.0	39.6	4.9e-04	0.045	0.014	2.4e-03
With PJ correction (m = 34 .. 41)	7.4	2.5	3.1e-05	0.027	0.0081	1.4e-03
With PJ correction (m = 35 .. 40)	0.71	0.23	2.8e-06	0.0030	0.0013	2.3e-04

Table 3.13: Compilation of all FPI calibration coefficients.

$z(\lambda)$			$2\delta(\lambda)$		
A	B	C	α	β	λ_0
81572.	5.75	10.	3.02994e-1	2.67029e-4	2150.

order. The order independent parameters are denoted as A and B , respectively. They are given in Tab. 3.11. The coefficients A directly represent the plate separation at zero position of z . With these corrections they stay constant with a very high precision.

One might want to adjust for a small remaining offset with a constant C :

$$z = \frac{1}{B}(m\lambda + 2\delta(\lambda) - A) + C \quad (3.18)$$

The fine tuning of the constant C should be carried out with phase map corrected frames (see Section 3.8.3). The accuracy of the calibration results is demonstrated by the comparison of the coefficients with and without correction for the phase jump (Table 3.12). The absolute and relative 1σ errors, and the maximum absolute deviations are given. The precision increases drastically when we omit the orders that show up only with a few data points at the corners of Fig. 3.22. Then the separation determined with the regression line parameters of the different orders (i.e., different wavelengths) deviate only 0.23 nm from each other. Regarding the double separation $2d$ being approximately $80\ \mu\text{m}$, a relative error of $\sigma_{rel} = 2.8\text{e-}6$ is very small. Nevertheless, according to the σ_{rel} for the coefficients A and B in Table 3.12, the precision of finding the z -value for a certain wavelength is determined by the slope B . Thus, as long as we are not very close to the zero position of z ,

$$\Delta z = \frac{z(\lambda)}{B} \cdot \Delta B = z(\lambda) \cdot \sigma_{rel}^B \quad (3.19)$$

describes the error for z . With a proper model for the phase jump, the error is only a fraction of an FCU within the scan region ($-500 \leq z \leq 500$). This precision is easily enough to allow for a correct tuning of the plate separation for the desired observing wavelength.

3.8.3 The phase map

A major purpose of applying the FPI to astronomical observations is the generation of velocity maps with high angular resolution. For each FPI exposure, the interference condition varies radially over

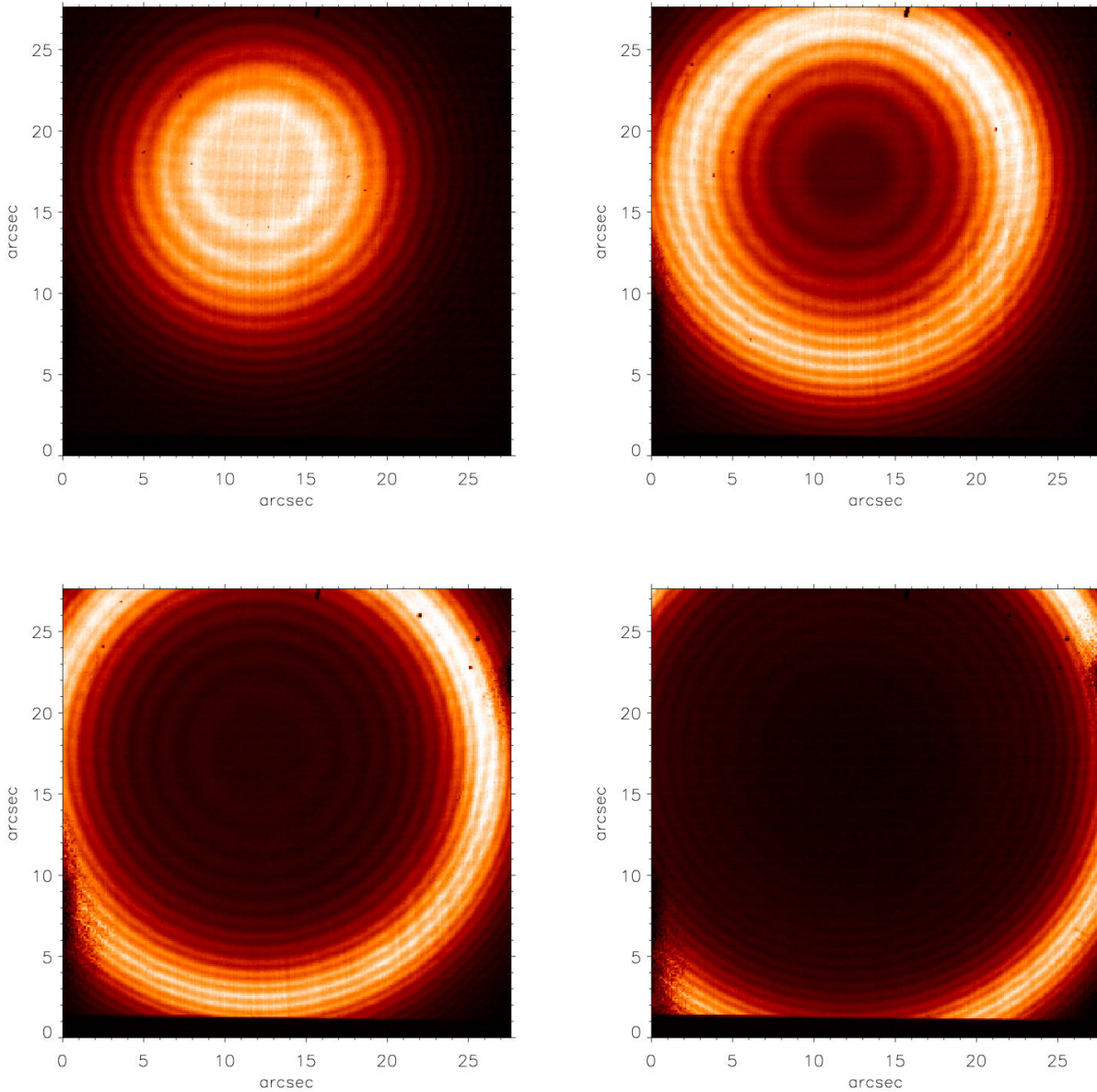


Figure 3.25: Calibration of the phase shift map via transmission rings from the 2062.18 nm vacuum Argon line. The frames were extracted from the cube for z ranging from 165 FCU through 195 FCU in steps of 10 FCU. According to the interference condition the FPI transmits the calibration line in a ring-shaped part of the FOV. These rings spread out over the FOV while the plate separation is varied. The substructure of the rings (narrow circular wiggles) reflects high order interference of the etalon plates itself. They are independent of the tunable interference spacing (Sect. 3.8.4).

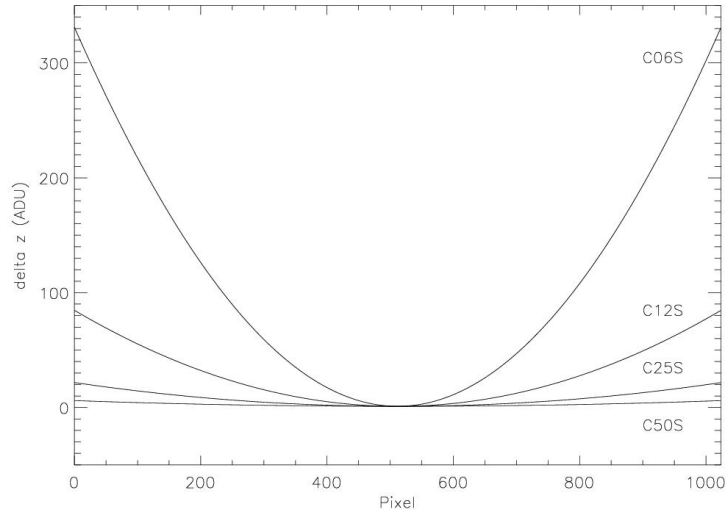


Figure 3.26: Phase maps for all cameras (vertical cut): z -correction versus pixel coordinate.

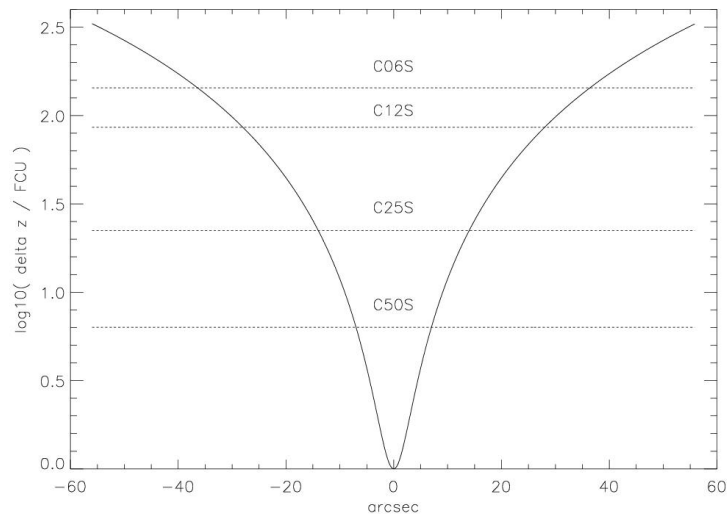


Figure 3.27: Phase maps for all cameras (vertical cut): z -correction versus angle (arcsec).

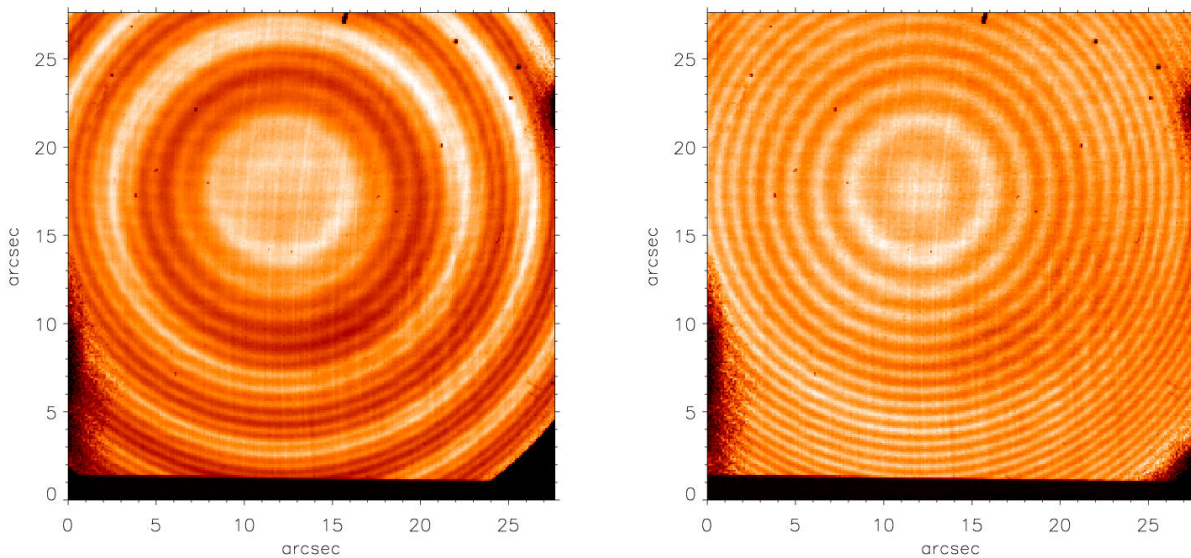


Figure 3.28: After transformation of the (x, y, z) -cube to the (x, y, λ) -cube, the frame for $\lambda = 2061.12 \text{ nm}$ is extracted. Since this is the central wavelength of the calibration line that was used to generate the phase-shift map, we expect to obtain a frame with constant intensity over the FOV. The frame to the left is extracted from (x, y, λ) -cube without convolving the spectral channel with the spectral response of the FPI. Thus, modulations due to the spectral sampling appear. The right frame is corrected for the sampling of the wavelength channel in convolving with the spectral FPI response. The remaining effects are a smooth large scale intensity variation indicating the lack of a flat field cube and small scale variation (circular wiggles) analogous to the ones in Fig. 3.25. Both frames are displayed with a linear intensity stretch.

the field. Thus the phase is shifted over the FOV.¹⁵ The equation

$$m \cdot \lambda + 2\delta(\lambda) = \frac{2d}{\sqrt{1 + (\frac{r}{f})^2}} \quad (3.20)$$

describes how the interference condition changes for different inclination angles. The effective phase shift per plate $\delta(\lambda)$ must not be neglected, since this would cause significant deviations over the full wavelength range, in particular for the cameras with a larger FOV. The radial variation of the interference condition makes the calibration line appear as a ring that is described by radius r and focal length f in consistent units. In a typical FPI observation, images at different plate separations are stored in a data cube. For example, Fig. 3.25 shows four frames taken from such a data cube. According to the inclination dependent interference condition, the transmission ring spreads out over the FOV for different plate separations, i.e, the FOV is scanned by the moving transmission ring while the plate separation is modified. In the case of this calibration cube, the shown intensity profiles indicate the spatial position in the FOV dependent on z (plate separation) where the corresponding z -frame transmits the vacuum calibration line (2061.2 nm). The rings show a substructure, i.e. the intensity wiggles at a smaller scale than the FWHM of the ring. This small-scale intensity variation is due to interference emerging from the plates of the FPI itself (Sect. 3.8.4), and *not* from the tunable cavity. These small intensity variations (maximum 5% of total intensity) that are independent of the actual spacing, could be avoided using wedge-shaped plates. Nevertheless, this artifact does not influence the calibration procedure. Also, it seems that astronomical data are not afflicted by this effect either, since the intensity variations are small and the wiggles are expected to smear out for broader lines.

The actual wavelength information is restored by performing a phase correction that, after all, allows for the construction of a velocity map (Chapter 5). Here, we focus on the construction of the phase shift map through the calibration data.

Equation 3.20 is graphically presented in Fig. 3.26 and Fig. 3.27 using the parameters determined before (Tab. 3.13). A vertical cut through the phase maps for all cameras is shown. In Fig. 3.26 the necessary phase shift correction in FCU is plotted over the detector position in pixels. Figure 3.27 shows the same curves, but the abscissa in arcseconds. Thus, one curve describes the phase shift for all cameras. The FOV is indicated by the horizontal dotted lines. The pixel scales of the cameras differ from each other by a factor of 2 (see Chapter 2). Camera C06S is the only pupil limited camera, explaining the downward shift horizontal line in Figure 3.27. In the second representation of Eq. 3.20, the ordinate is plotted logarithmically. Here, the deviation from a parabolic approximation of the phase map (straight line in a logarithmic plot) stands out.

Using Eq. 3.20 and Eq. 3.18, the z -value is determined for a certain position (x, y) and the selected wavelength. Since the data cube is taken at discrete z -values, intermediate positions of the (x, y, z) -cube have to be linearly interpolated. This interpolation must be done for all (x, y) -coordinates (all pixels of the frame) to cover the whole FOV. In this way, a frame at the spectral center of the calibration wavelength ($\lambda_{\text{cal}} = 2061.18$ nm) is generated (Fig. 3.28). The dark edge at the right bottom of the frame belongs to the part of the FOV where the transformation of the (x, y, z) - to a (x, y, λ) -frame has no data.

In addition, the left frame in Fig. 3.28 shows a radial intensity variation with a frequency corresponding to the wavelength sampling of the (x, y, z) -cube. We can use Fig. 3.25 to estimate the sampling of the wavelength channel. Comparing the shift of the peak and the FWHM of the transmission

¹⁵Useful up-to-date hints and ideas for FPI data reduction are found in, e.g. Gordon et al. (2000); Moiseev (2002).

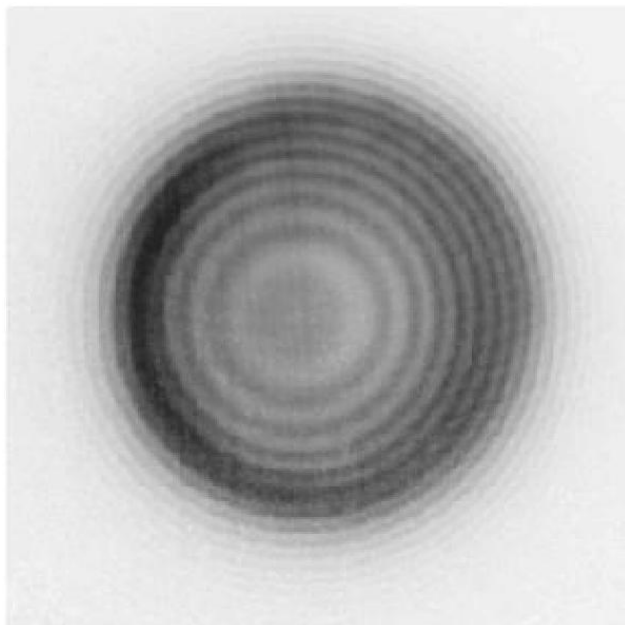


Figure 3.29: Direct spectroscopy imaging of a $2.06 \mu\text{m}$ Argon line. The broad ring is due to interference in the plate gap and can be manipulated by alternating the plate space. The small rings represent interference within the plates itself.

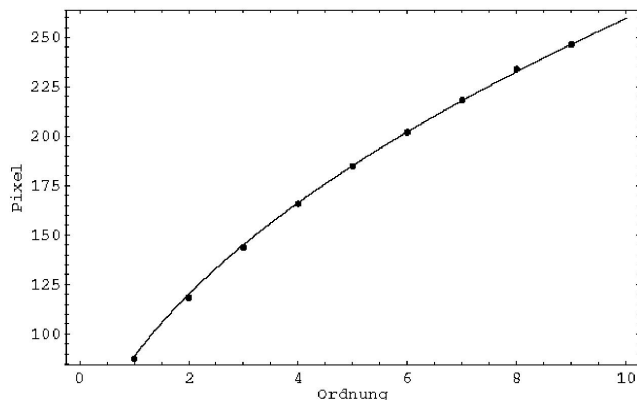


Figure 3.30: The points represent the radii in pixels of the narrow rings. The radii are plotted over the order Δm . The fit yields a plate thickness of 9.9 mm.

ring, we find a sampling value of 1.6 - which means, the wavelength channel is slightly undersampled. A value of 2 would be required for Nyquist sampling. Hence, we can trace back the intensity undulations to poor spectral sampling. To account for this, we need to convolve the wavelength channel ($x, y = \text{const}$) with the spectral response $H(z)$ of the FPI:

$$I^*(z) = I(z) * H(z) \big|_{x,y=\text{const}} \quad (3.21)$$

The spectral response $H(z)$ of the FPI is assumed to be constant over the FOV (good approximation for slow cameras) and is constructed by a Gaussian with the appropriate FWHM. $I(z)$ and $I^*(z)$ denote the intensity in the wavelength channel before and after the correction for the spectral resolution of the FPI. Again, this process to be done for each pixel of the frame to cover the full FOV. In theory, this convolution is needed in any case, but in practice the intensity modulation will only cause difficulties when the sampling is close to Nyquist or worse.

3.8.4 Narrow fringes

The narrow interference rings (circular small scale wiggles) seen in Fig. 3.25 and Fig. 3.28 are due to interference within the plane parallel plates themselves. This high order interference is independent of the tunable interference spacing, but accords to the fixed plate separation of the interference etalons (approximately 1 cm) and the refractive index of the medium.

With the aid of Fig. 3.29 we try to determine the orders of the narrow fringes and to verify the consistence of the proposed origin. The interference pattern shown in this figure is one of the first images

taken with the FPI in the laboratory period in Heidelberg. The assymetry of the broad interference ring hints a slight misalignment. For an optimal detection of the narrow interference rings with the smallest radii, the interference spacing is tuned such that the Argon calibration line ($2.062 \mu\text{m}$) just emerges. The use of an adequate narrow band filter avoids any perturbation by neighbouring lines. With the relation

$$2d\sqrt{n^2 - \sin^2 \phi} = m\lambda \quad (3.22)$$

for interference curves of plane parallel plates (Born and Wolf 1999) we can identify the orders and radii of the narrow interference rings in Fig. 3.29. The thickness of the plate is referred by d , the refraction index by n and the entrance angle by ϕ . (Note: According to the refractive index the angle inside the medium differs from the entrance angel ϕ .) To perform a fit at the radii (given in pixels) in Fig. 3.29 the expression is solved for ϕ and transferred into pixel coordinates, taking into account the f-ratio of Camera 12S (f/12.7) and the pixel size ($27 \mu\text{m}$):

$$\phi(\Delta m) = \arcsin \sqrt{n^2 - \frac{(m_0 - \Delta m)\lambda}{2(d - s)}} \cdot \frac{127}{27 \cdot 10^{-3}}. \quad (3.23)$$

The order of the the smallest interference ring is m_0 and s corrects d in the range of half a wavelength. The refraction index of silicate glass amounts to 1.436 by a temperature of 60 K. The fit shown in Fig. 3.30 yields a plate thickness of $d = 9.9 \text{ mm}$ ($m_0 = 13802, s = 0.05\lambda$), in agreement with the specifications of the manufacturer (Queensgate Instruments Ltd. 1995).

Chapter 4

Calibration of static aberrations of NAOS and CONICA

The essential parts of this chapter are published in
Blanc et al. and Hartung et. al. (2003), *Astron. Astrophys.*, 399, p.373-394.

This chapter is dedicated to the presentation of a technique that benefits of the AO system to correct not only for atmospheric turbulence but also for the internal optical aberrations of the high-resolution camera and the beam splitters of NAOS. The aberrant optical components in the light path of CONICA as well as the beam splitters are outside of the AO loop and therefore no self-acting correction is possible. Independently of the AO wavefront sensor, a separate measurement of these aberrations using a method called phase diversity (PD) allows one to predict for a certain instrument configuration the corresponding aberrations. They are quantified by sets of Zernike coefficients that are rendered to the adaptive optics. This technique turns out to be very flexible and results in a further improvement of the optical overall performance.

The implementation of a phase diversity wavefront sensor to the instrument, data acquisition and the error budget are described in the first section of this chapter (Sect. 4.1). Details concerning particular hardware features and software architecture are beyond the scope of this thesis and can be found in Hartung (2003, Manual). In the second section (Sect. 4.2) we present the obtained calibration results, the allocation of wavefront error to their original components, and the achieved gain in optical performance.

NAOS-CONICA may be the first instrument having a higher-order static calibration technique fully implemented and there is no doubt that future high performance AO systems cannot ignore static aberration. On the way to the ultimate optical performance every percentage point of loss in Strehl has to be tackled. The concept of design should comply with the needed requirements from the beginning.

The multi-conjugate Adaptive optics Demonstrator MAD (Marchetti et al. 2003) may serve as an example for a next generation AO system being currently developed, where the presented PD approach is intended to be implemented. The reader may be reminded that the following calibration procedure strictly applies only on-axis, but off-axis corrections are negligible for the NAOS-CONICA case due to the restricted FOV. Hence, off-axis corrections are not explicitly included to the calibration method, but they are taken into account in the error budget. For MAD, designed for a FOV of 2 arcmin, reasonable correction must probably include an explicit angle dependency.

4.1 Application of the phase diversity technique

To retrieve the maximum possible performance of the system in terms of Strehl ratio¹ (SR) a method has been developed to calibrate the remaining degradation of the image quality induced by its optical components. Defaults of the wavefront attributed to any degradation within the AO loop (common path) are seen directly by the AO wavefront sensor (WFS) and thus the AO system can correct for these aberrations automatically. This is not the case for a degradation of image quality induced by components outside the AO loop. An experimental setup has been applied which allows one to sense the wavefront of the light which has passed the whole system *without* making use of the AO wavefront sensor. Therefore we draw on a well-known method called phase diversity (Gonsalves 1982; Paxman et al. 1992). It turns out that a number of theoretical and experimental constraints have to be examined before reliable results can be obtained in sensing the wavefront via phase diversity (PD). In this section the main limitations of this phase diversity approach are compiled. The systematic errors due to the experimental implementation and the design restriction are investigated. Further error sources stem from the imperfect knowledge of the system, and from algorithm limitations. The essential verifications and calibrations needed to obtain accurate results are highlighted and a practical guideline for the application of a phase diversity wavefront sensor is given.

First, we describe the phase diversity concept along with the specific algorithm used in our particular case (Sect. 4.1.1).

4.1.1 Estimation of static aberrations by Phase Diversity

4.1.1.1 Phase diversity principle

The estimation of the aberrations from the sole focused image does not ensure the uniqueness of the solution. This indetermination is due to the relationship between the point spread function (PSF) h and the aberrated phase: a couple (ϕ, ϕ') exists such that $h(\phi) = h(\phi')$. Phase diversity (Gonsalves 1982; Paxman et al. 1992) was proposed to add information and thus removes this indetermination. The idea is to collect at least one additional image, which differs from the focused one by a known phase variation. Figure 4.1 illustrates the phase diversity principle. One can note that there are several ways to introduce the known aberration:

- simultaneously using a beam splitter and two detectors as presented in Figure 4.1;
- introducing a beam-splitter and a prism and recording the focused and defocused images on the same detector (Gates et al. 1994);
- sequentially using a translation of the detector or introducing the known aberration in the optical path (see Sect. 4.1.1.3). In this case, it is assumed that the aberrations and the object do not evolve between the two acquisitions (which is the case of the NAOS-CONICA static aberrations for instance).

This technique has been successfully used by some authors to determine aberrations (Carreras et al. 1994; Kendrick et al. 1994; Lee et al. 1997; Thelen et al. 1999; Löfdahl et al. 2000) and also to

¹The SR ratio is a common way to describe the quality of the point spread function. It is given by the ratio of the measured and the theoretical diffraction-limited peak intensity (see Appendix C).

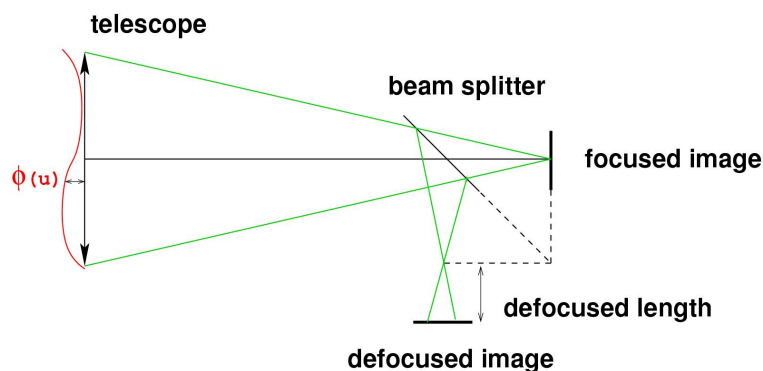


Figure 4.1: Phase diversity principle

restore images, as in solar imaging through turbulence (Restaino 1992; Löfdahl and Scharmer 1994; Seldin and Paxman 1994). It uses a low-cost, optically simple wavefront sensor which consists in the imaging camera itself, but it requires a complex numerical and iterative processing to restore the unknowns from the images.

4.1.1.2 Imaging model

In the isoplanatic patch of the imaging system, the image is the noisy convolution of the PSF h in the observation plane and the object o :

$$i(\mathbf{r}) = (h * o)(\mathbf{r}) + n(\mathbf{r}) \quad (4.1)$$

where \mathbf{r} is a two-dimensional vector in the image plane and n is an additive noise. The PSF associated with the focused image is given by:

$$h_1(\mathbf{r}) = |FT^{-1}[P(\mathbf{u}) \cdot \exp(i\phi(\mathbf{u}))]|^2 \quad (4.2)$$

where \mathbf{u} is a two-dimensional vector in the pupil plane, ϕ is the unknown aberrated phase function, P is the aperture function and FT^{-1} denotes the inverse Fourier transform. The phase function is expanded on a set of Zernike polynomials. Indeed, aberrations in an optical system can be mathematically represented by Zernike polynomials (Noll 1976).

$$\phi(\mathbf{u}) = \sum_{i=1}^k a_i Z_i(\mathbf{u}) \quad (4.3)$$

Theoretically, k should tend to infinity to describe any wave form, but in the particular case of static aberration estimation, the first polynomials (typically the first twenty) are enough to describe the aberrations. In the following, we will note $\mathbf{a} = (a_1, \dots, a_k)^T$ the unknown aberration coefficients, where T denotes transposition.

In the defocused plane, the PSF is given by :

$$h_2(\mathbf{r}) = |FT^{-1}[P(\mathbf{u}) \cdot \exp(i(\phi(\mathbf{u}) + \phi_d(\mathbf{u})))]|^2 \quad (4.4)$$

where ϕ_d is the known diversity phase function. In our case, $\phi_d(\mathbf{u}) = a_4^d Z_4(\mathbf{u})$ where Z_4 is the defocus Zernike polynomial.

In practice, data are discrete arrays because of the spatial sampling of the images. Equation 4.1 takes the form:

$$\mathbf{i} = \mathbf{H}\mathbf{o} + \mathbf{b} \quad (4.5)$$

where \mathbf{H} is the Toeplitz matrix corresponding to the convolution by h (Ekstrom and Rhoads 1974), and where \mathbf{i} , \mathbf{o} and \mathbf{b} are the discrete forms of the previous variables.

The problem is to estimate the aberration parameters \mathbf{a} (the set of a_i) from the data (focused \mathbf{i}_1 and defocused \mathbf{i}_2 images) and the defocused distance, without knowing the object \mathbf{o} .

4.1.1.3 Aberration estimation principle

Using a Joint Maximum A Posteriori (JMAP) approach (Little and Rubin 1983), an estimator can be defined as

$$\begin{aligned} (\hat{\mathbf{o}}, \hat{\mathbf{a}})_{\text{JMAP}} &= \arg \max_{\mathbf{o}, \mathbf{a}} p(\mathbf{i}_1, \mathbf{i}_2, \mathbf{o}, \mathbf{a}) \\ &= \arg \max_{\mathbf{o}, \mathbf{a}} p(\mathbf{i}_1 | \mathbf{o}, \mathbf{a}) p(\mathbf{i}_2 | \mathbf{o}, \mathbf{a}) p(\mathbf{o}) p(\mathbf{a}) \end{aligned} \quad (4.6)$$

where $p(\mathbf{i}_1, \mathbf{i}_2, \mathbf{o}, \mathbf{a})$ is the joint probability density function of the data $(\mathbf{i}_1, \mathbf{i}_2)$, of the object \mathbf{o} and of the aberrations \mathbf{a} . $p(\mathbf{i}_1 | \mathbf{o}, \mathbf{a})$ and $p(\mathbf{i}_2 | \mathbf{o}, \mathbf{a})$ denote the likelihood of the data \mathbf{i}_1 and \mathbf{i}_2 , $p(\mathbf{o})$ and $p(\mathbf{a})$ are the *a priori* probability density function of \mathbf{o} and \mathbf{a} . The noise is modelled as a stationary white Gaussian noise with a variance σ^2 (the same for the two images). In our case, we do not use an explicit probability density function for \mathbf{a} ($p(\mathbf{a}) = 1$) since the regularization is brought by the small number of estimated Zernike coefficients. Consequently, this joint estimation will be called a Generalized Maximum Likelihood (GML) approach. We choose a Gaussian prior probability distribution for the object with a covariance matrix R_o . The maximization of the a posteriori probability law defined in Equation 4.6 is equivalent to the minimization of its neg-logarithm (J_{GML}) defined as

$$\begin{aligned} J_{\text{GML}}(\mathbf{o}, \mathbf{a}) &= \frac{1}{2\sigma^2} \|\mathbf{i}_1 - \mathbf{H}_1 \mathbf{o}\|^2 + \frac{1}{2\sigma^2} \|\mathbf{i}_2 - \mathbf{H}_2 \mathbf{o}\|^2 \\ &\quad + \frac{1}{2} \mathbf{o}^t \mathbf{R}_o^{-1} \mathbf{o} \end{aligned} \quad (4.7)$$

It is important to note that the derivative of $J_{\text{GML}}(\mathbf{o}, \mathbf{a})$ with respect to the object gives a closed-form expression for the object $\hat{\mathbf{o}}(\mathbf{a})$ that minimizes the criterion for a given \mathbf{a} (Paxman et al. 1992). This expression is that of a bi-frame Wiener filter:

$$\hat{\mathbf{o}}(\mathbf{a}) = (\mathbf{H}_1^t \mathbf{H}_1 + \mathbf{H}_2^t \mathbf{H}_2 + \sigma^2 \mathbf{R}_o^{-1})^{-1} (\mathbf{H}_1^t \mathbf{i}_1 + \mathbf{H}_2^t \mathbf{i}_2). \quad (4.8)$$

Substituting $\hat{\mathbf{o}}(\mathbf{a})$ into the criterion yields a new criterion that does not depend explicitly on the object:

$$J'_{\text{GML}}(\mathbf{a}) = J_{\text{GML}}(\hat{\mathbf{o}}(\mathbf{a}), \mathbf{a}). \quad (4.9)$$

The interest of this new criterion is the reduction of the solution space.

Furthermore, using a periodic approximation (which corresponds to approximate a Toeplitz by a circulant matrix) (Demoment 1989), the criterion can be expressed in the discrete Fourier domain:

$$J_{\text{GML}}(\mathbf{o}, \mathbf{a}) \propto \sum_f \left[\frac{|\tilde{h}_1(f) \tilde{o}(f) - \tilde{i}_1(f)|^2}{\sigma^2} + \frac{|\tilde{h}_2(f) \tilde{o}(f) - \tilde{i}_2(f)|^2}{\sigma^2} + \frac{|\tilde{o}(f)|^2}{S_o(f)} \right] \quad (4.10)$$

where $\tilde{\cdot}$ stands for a Discrete Fourier Transform (DFT), f the spatial frequency and S_o the power spectral density (PSD) of the object.

Using the same periodicity approximation, $\tilde{\mathbf{o}}(\mathbf{a})$ can be written as :

$$\tilde{\mathbf{o}}(\mathbf{a}) = \frac{\tilde{h}_1^*(f) \tilde{i}_1(f) + \tilde{h}_2^*(f) \tilde{i}_2(f)}{|\tilde{h}_1(f)|^2 + |\tilde{h}_2(f)|^2 + \sigma^2/S_o(f)}. \quad (4.11)$$

$\tilde{\mathbf{o}}(\mathbf{a})$ can be introduced in Equation 4.10 so that, the new criterion $J'_{\text{GML}}(\mathbf{a})$ only depends on the unknown phase aberrations (\mathbf{a}) and can be minimized using an iterative algorithm (for instance a conjugate gradient).

Object regularization The *a priori* information required on the object consists in the choice of the object power spectral density model. In our case a focused and a defocused image are acquired with high Signal to Noise Ratio (SNR) and the object is close to be a Dirac function. Consequently the phase estimation can be obtained without any knowledge or estimation of the prior object spectral density. The ratio $\sigma^2/S_o(f)$ is simply set to a small arbitrary constant (10^{-6} in our case) in order to avoid numerical problems due to computer precision. Notice that, in the case of lower SNR, the use of a marginal estimator which estimates the sole aberration parameters, gives better results than this ad-hoc regularization (Blanc et al. 2000; Blanc 2002).

Choice of the defocus distance The choice of the known defocus distance is essential to obtain accurate results. The RMS defocus coefficient a_4^d depends on the defocus distance d of the second image, the telescope diameter D and the focal length F through:

$$a_4^d = \frac{\pi d}{8\sqrt{3}\lambda(F/D)^2} \text{(in radian)} \quad (4.12)$$

The corresponding peak-to-valley optical path Δ is equal to

$$\Delta = \frac{\sqrt{3}\lambda a_4^d}{\pi} = \frac{d}{8(F/D)^2} \text{(in m)} \quad (4.13)$$

In the following sections, a_4^d will be given in nanometers. For NAOS+CONICA, $F/D = 15$. It has been shown (Lee et al. 1999; Meynadier et al. 1999) that a defocus Δ equal to λ provides accurate results. In our case, this corresponds to a defocus distance equal to 4 mm for $\lambda = 2.2 \mu\text{m}$. In fact the “optimal” defocus distance depends on the object structure, the phase amplitude ϕ and the signal to noise ratio (SNR) on the images. In practice a large domain around this value (typically $\lambda \pm \lambda/2$) still provides accurate results (Meynadier et al. 1999). In the case of NAOS-CONICA static aberration estimation, two different procedures are applied to introduce the defocus. They are explained in detail in Sect. 4.1.2.

Table 4.1: The required defocus distances for a phase diversity of 2π rad (peak to valley) ($\lambda = 1\mu\text{m}$) are listed corresponding to the f-ratios (pixel scales).

Camera	f/D	Pixel scale	d (mm)
C50S	51	13.3 mas/pixel	20.8
C25S/C25L	25.5	27.1 mas/pixel	5.2
C12S/C12L	12.8	54.6 mas/pixel	1.3
C06S/C06L	6.38	109 mas/pixel	0.33
Entrance focal plane	15	1.72 mas/ μm	1.8

4.1.2 Phase diversity setup

Our input for phase diversity wavefront estimation are two images: one of them in focus and the other one out of focus. In this manner we introduce the well-known phase diversity which is an obligatory input parameter for PD. One should recall that best phase diversity estimates are to be expected applying a peak to valley phase diversity $\Delta\phi$ between 1π and 3π and the input images must be at least Nyquist sampled. The corresponding defocus distance d depending on the applied wavelength is obtained by

$$d = \frac{4\lambda}{\pi}(f/D)^2\Delta\phi. \quad (4.14)$$

In the next two subsections we describe in detail two ways of introducing this phase diversity. Both ways are essential to enable us to separate the wavefront error and to assign it to different contributors. This disentanglement is described in Section 4.2.1.1.

4.1.2.1 CONICA stand-alone: focus shift by object

First, we regard the possibilities to obtain the necessary input images with CONICA stand-alone. The CONICA detector is mounted on a tunable stage which is software controlled and can be driven in the cold environment. This allows us in principal to obtain a defocused image but the focus drive spans only a region of 2mm. Using Equation 4.14 we compile for all available camera objectives the necessary defocus distances in the detector plane corresponding to a diversity of 2π at a wavelength of $1\mu\text{m}$ in Table 4.1. Only for the low magnification cameras (C06, C12) is the defocus distance sufficient. But these very cameras undersample in K and at shorter wavelengths so that the focus stage mechanism finally fails in every case. For that reason we swerve to the entrance focal plane. Here a phase diversity of 2π corresponds to 1.8mm at a wavelength of $1\mu\text{m}$ or 3.6mm at $2\mu\text{m}$, which is small enough to be implemented in the entrance focal plane.

In this plane a wheel is located carrying different field limiting masks, coronagraphic masks and the slits for spectroscopy. On the wheel we implement four different pinholes at different axial positions. The pinhole diameter is $10\mu\text{m}$. One pinhole is placed exactly in the entrance focal plane and yields a focused image on the detector (0mm), and three other pinholes are located 1mm, 2mm and 4mm out of the entrance focal plane. The four pinholes are mounted onto a plate fitting in a socket of the mask wheel. This device will be referred to as a Zernike tool later on. Impacts on the PD estimation

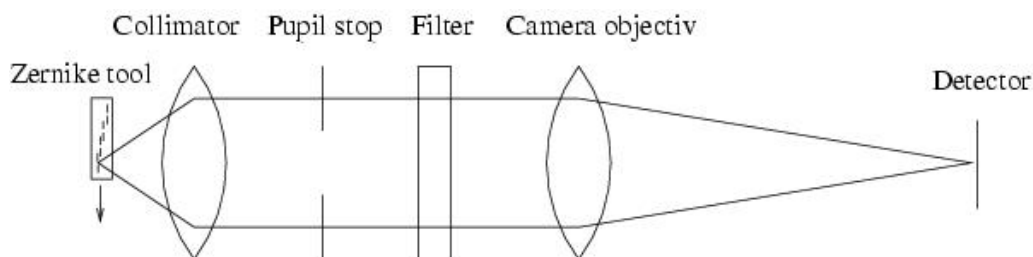


Figure 4.2: The Zernike tool with its pinholes in the light path of CONICA.

due to the mechanical precision of the pinhole positions and possible deviations of their shape are investigated in Sect. 4.1.4.1.

Fig. 4.2 depicts the setup for the CONICA internal phase diversity measurements. The leftmost component carries the four pinholes, which are shifted against each other, with the values given above. In rotating the wheel holding the Zernike tool we are able to select a pinhole in the field of view. After a collimating lens and a pupil stop, a filter selects the wavelength range and finally the camera objective forms the object image on the detector. The chosen camera objective determines the f-ratio and the pixel scale.

To center the image of the pinholes on the detector, the whole pinhole mount is shifted by turning the mask wheel. In principal PD needs the input images to be on the same spot to ensure that the same aberrations are sensed. The horizontal position of the pinholes can be controlled by adjusting the rotation angle of the wheel. In vertical direction there is no degree of freedom, but the four pinholes are mounted circularly to compensate for the circular movement. By this means a vertical precision of 50 mas (C50S) can be reached². This is easily sufficient not to see any influence due to field aberration effects. PD measurements taken at different detector positions and calculations performed with an optical design software showed that even at the corner of the field of view (13 arcsec) the field aberration is negligible (Sect. 4.1.4.1). Note that for some preliminary measurements in an earlier version of the Zernike tool was used with a design not optimized for the circular movement of the pinholes. The worst separation that could occur with the former Zernike tool was about 1.3 arcsec. But even with this tool no relevant impact on the precision of wavefront sensing was detected.

Apart from the fact that the Zernike tool with its pinholes at the entrance focal plane provides the required focus shifts, it is convenient that the required focus shifts do not depend on the camera objective (pixel scale) anymore. But note: defocusing by moving an object in the entrance focal plane does not correspond exactly to a defocus due to a shifted detector plane. An investigation of this effect is done in Sect. 4.1.4.1 and turns out to be negligible.

The compilation in Table B.1 is helpful to select the adequate pinhole pair and to verify that the Nyquist criterion is fulfilled at a given wavelength. The level of oversampling is quantified in the last two columns. For a number greater than one the Full Width Half Maximum (FWHM) of the point spread function (PSF) covers at least two pixels. Only these input images can be handled properly by the PD routine we use. Indeed it is possible to modelise the wavefront error even at undersampled images (Jefferies et al. 2002). In our case there is no forfeit to be constrained by the Nyquist criterion because we can rather select the appropriate filter or we deal with a camera used in L- and M band where static wavefront aberrations are negligible.

²1 pixel corresponds to 13.3 mas (C50S)

Table 4.2: Defocus distances induced by the use of various pinhole pairs. 0-2 and 0-4 pairs are recommended for J-H and K filters respectively.

pinhole pairs	0-1	0-2	0-4	1-4	2-4
Defocus distance (mm)	1	2	4	3	2

The necessity of introducing enough diversity between the two images and the higher SNR of images obtained with the pinhole 0 (which is in the focal plan) lead us to choose the pair 0-2 for J and H filters and the pair 0-4 for K filters. Note that the use of pinholes in the entrance focal plane is not optimal for the phase diversity algorithm since

- the known aberration is not a pure defocus (a longitudinal translation in the entrance focal plane of the camera is not completely equivalent to a detector translation in the imaging focal plane) – see Sect. 4.1.4.1,
- the use of different pinholes may induce errors in the aberration estimation (the PD algorithm assumes that the same object is used to obtain focused and defocused images, see Sect. 4.1.4.1). Shape differences between two pinholes can induce phase estimation errors,
- the focused and defocused images are not at the same position on the detector and need to be re-centered – see Sect. 4.1.5.2 – since PD can not estimate relative tip-tilt greater than λ between the two images. The phase is estimated modulo 2π – see Equations 4.2 and 4.4,
- last, there may be field aberrations due to the different pinhole position in the beam – see Sect. 4.1.4.1.

To summarise: the PD input data to derive the total CONICA internal aberrations are obtained by object defocusing in the CONICA entrance focal plane. The object defocusing is realized by four $10\mu\text{m}$ pinholes at different axial positions. Note that since the entrance focal plane of CONICA is located inside the cold cryostat, aberrations accrued from the CONICA entrance window are not included in this wavefront estimation. The procedure described in Sect. 4.1.1.3 allows us to estimate the set of aberrations for each CONICA configuration.

4.1.2.2 NAOS-CONICA: focus shift by the deformable mirror

Now, we describe how the PD input images are obtained which are used to sense the wavefront aberrations of the whole instrument, i.e., the adaptive optics NAOS together with its infrared camera CONICA. In this case we can take advantage of the AO system’s capabilities to itself introduce an adequate focus shift and thus there is no need for the implementation of a special tool or a modification of the design.

In the entrance focal plane of NAOS, which coincides with the VLT Nasmyth focal plane, a calibration point source can be slid in and imaged by CONICA. This point source is realized by the output of a fiber with a diameter of $10\mu\text{m}$ fixed on a movable stage. On the same stage a second source much larger in diameter ($400\mu\text{m}$) is mounted. It is only seen by the WFS and serves as a reference source to close the loop. The extended source is needed to improve the feedback signal in case of no

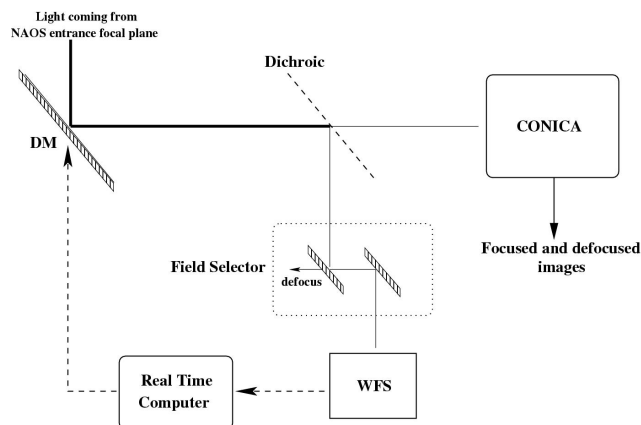


Figure 4.3: Defocusing in closed loop using the NAOS Field Selector

atmospheric turbulence. By this means the AO control loop is adjusted for any aberrations emerging in the common path. To obtain the focus shift affecting the entire instrument, we introduce the desired amount of defocusing in the WFS path by moving the mirrors of the field selector. During this process the loop is kept closed. Instantly, the arising focus shift is detected by the WFS. Correspondingly, the real time computer commands the DM to compensate for the detected defocus. Finally, the spots on the Shack-Hartmann WFS are centered again, but the defocus of the DM takes effect in the imaging path. For a pure defocus the DM will take a parabolic shape. The maximum achievable defocus by this method is limited by the DM's stroke and turns out to be about 20 mm. Referring to Table 4.1, this is enough to introduce the needed diversity for an f/15 beam.

The procedure is shown in Fig. 4.3 and provides us with the PD input data to estimate the NAOS-CONICA overall wavefront errors. In comparison with the procedure described in Section 4.1.2.1 we deal with the same object now, and we must not care about any deviations in the position of the image pairs. This simplifies data acquisition for the measurement and diminishes the number of possible error sources.

4.1.3 Simulation results

In order to validate the algorithm and to quantify its precision, we first consider simulated images. The conditions for this simulation are given by a point-like object, an imaging wavelength of $2.166 \mu\text{m}$ and a pure defocus equal to λ (peak to valley) between the two images, corresponding to a defocus coefficient a_4^d of 641.5 nm RMS. We degrade the PSF by a wavefront deformation described by its Zernike coefficients. The coefficients are arbitrary but chosen to have comparable values as observed in the calibration procedure (see Sect. 4.2). The phase is generated with the first 15 Zernike polynomials, note that the estimated phase will be expanded on the same polynomials. We add white noise to each image in order to obtain a SNR of 200 which corresponds roughly to the SNR of the CONICA data. The SNR is defined as the ratio of the maximum flux in the focus image over the RMS noise. The same noise statistics is applied to the defocused image. That results in a lower SNR on this image since the defocus spreads the PSF and reduces its maximum. The focused and defocused images are presented in Figure 4.4. In this example only two possible limiting parameters (see Sect. 4.1.4) have been taken into account: noise and image re-centering. The system is assumed to be perfectly adjusted and the images to be perfectly pre-processed without having any residual background features.

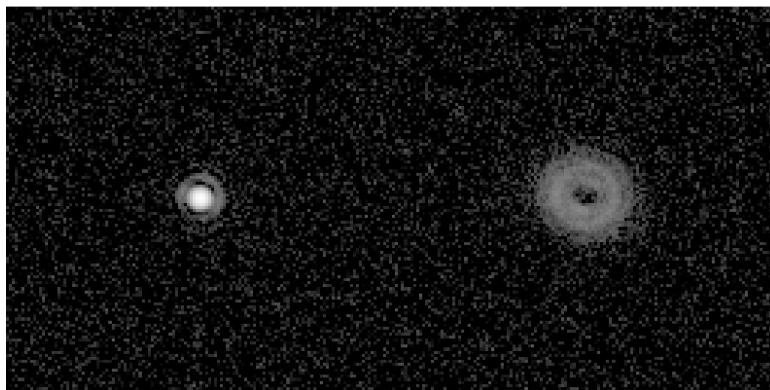


Figure 4.4: Simulated focused and defocused images (logarithmic scale). Noise is added to obtain a $\text{SNR} = 200$.

Table 4.3: Comparison between true and estimated Zernike coefficients applying phase diversity to simulated data with an image SNR equal to 200. The absolute value of the error is given for each coefficient. The total error is equal to 9.3 nm RMS.

Zernike number	4	5	6	7	8	9	10	11	12	13	14	15
true (nm)	60.5	-39.3	58.1	-16.2	-14.1	-2.5	13.7	-24.3	0.5	-3.2	2.8	-2.4
estimated (nm)	61.5	-46.7	61.7	-15.9	-10.9	-3.6	12.9	-26.0	1.2	-4.9	3.3	-2.2
error (nm)	1.0	7.4	3.6	0.3	3.1	1.1	0.7	1.7	0.7	1.7	0.4	0.2

Figure 4.5 shows a comparison between the input images of the simulation and the PSFs being reconstructed by the estimated aberrations and visualizes the quality of the aberration estimation. This visualization is helpful to judge real calibration data when only in-focus and out-of-focus images are available. Table 4.3 quantifies the performance of wavefront estimation through comparing the true and the estimated Zernike coefficients. On each coefficient a good accuracy is obtained; the errors are less than a few nanometers. The maximum error is for the two astigmatisms. Be recalled that the accuracy increases with the SNR. In the present simulation we considered a pessimistic case of SNR compared to the experimental NAOS-CONICA data. The influence of SNR on estimation results is analyzed in Sect. 4.1.4.

The slight tip-tilt introduced between the two input images (70 nm along X axis and -103 nm along Y) are estimated with a high precision, too. The error amounts to less than 1% (the tip-tilt values are not shown in Table 4.3.). In the next section, we focus on the possible sources for losses of estimation accuracy.

4.1.4 Error budget

The PD algorithm is based on several assumptions which must be well verified to obtain a good accuracy on the results. A list of possible error sources is given below. Quantitative results are essentially given on experimental data and with additional simulation data when necessary. The global procedure of data reduction can be found in Sect. 4.1.5. The error sources can be decomposed in three

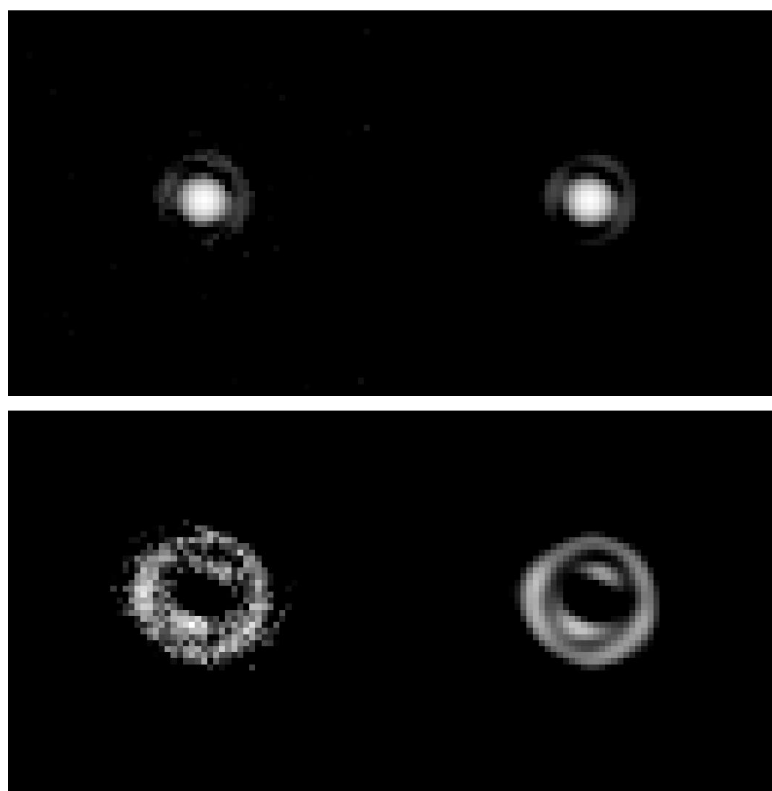


Figure 4.5: Comparison between images (left) and reconstructed PSFs (right) from estimated aberrations. On top the focused images, at the bottom the defocused images (logarithmic scale and zoom $\times 2$ are considered for each image).

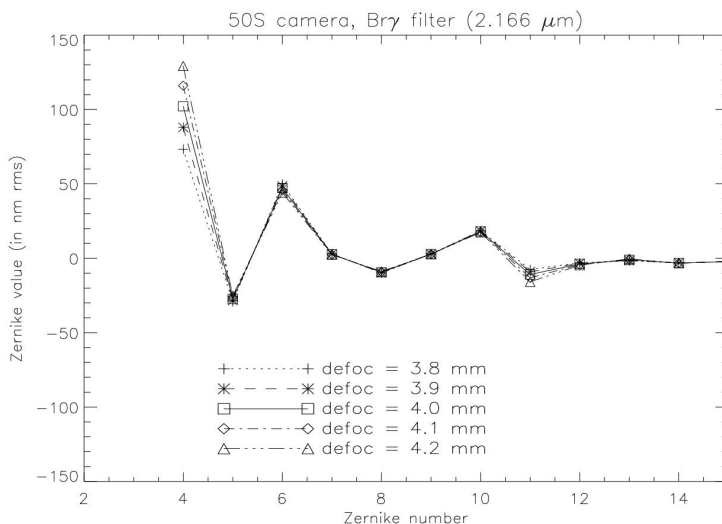


Figure 4.6: Influence of the error on defocus distance on estimated aberration by phase diversity. The CONICA camera C50S and the narrow band filter Br_γ are used. The focused and defocused images are obtained using the 0-4 pinhole pair (that is a theoretical defocus of 4 mm between the two images). For the same couple of images several defocus distances (from 3.8 to 4.2 mm) serve as input parameters.

parts: the errors due to a non-perfect knowledge of the system (calibration errors or uncertainties), the errors due to the image acquisition and pre-processing (noise, residual background, etc.) and the errors due to limitation of the algorithm (spectral bandwidth, amplitude of the estimated aberrations, etc.).

4.1.4.1 System limitations

First, we focus on the errors due to the imperfect system knowledge.

Defocus distance The major assumption of the PD principle is the addition of a *known* distortion (defocus in our case) between two images. An error on the defocus induces an error on the coefficients of radially symmetric aberrations, with a main part on the estimated defocus itself (see Figure 4.6).

In addition one can show in Figure 4.7 that for reasonable errors on the known defocus, the propagation error coefficient is equal to one. Hence, the uncertainty on the known defocus distance yields directly the uncertainty on the estimated defocus aberration.

This uncertainty on the defocus distance can be due to:

- an uncertainty on the physical position of the CONICA pinholes in the entrance focal plane. This uncertainty is estimated to ± 0.15 mm corresponding to $\Delta a_4 = \pm 24$ nm RMS,
- a systematic uncertainty on the F/D ratio (estimated to be less than two percent),

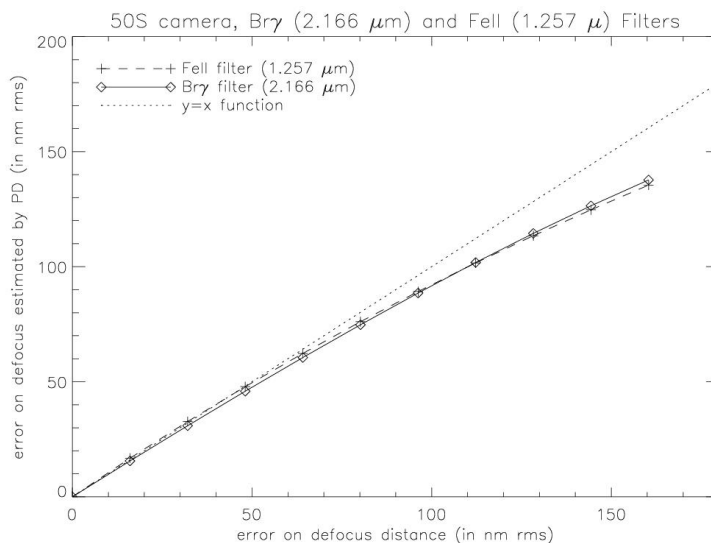


Figure 4.7: Influence of the error on defocus distance on the estimation of the defocus. Experimental data have been used. The results are given for the CONICA camera C50S and two narrow band filters: FeII ($1.527 \mu\text{m}$) and $\text{Br}\gamma$ ($2.166 \mu\text{m}$). The pinhole pair 0-2 (that is a theoretically defocus of 2 mm) and 0-4 (that is a theoretically defocus of 4 mm) are respectively used for FeII and $\text{Br}\gamma$ filters. For each couple of images several defocus distances (respectively from 1.5 to 2.5 mm and from 3.5 to 4.5 mm for FeII and $\text{Br}\gamma$ filters) serve as input parameters.

- the precision of a focus adjustment with the NAOS deformable mirror for the dichroic aberration estimation. This error is estimated to less than a few percent.

All these items lead to a precision of the estimated defocus roughly equal to a $\pm 30 \text{ nm}$. It will be shown in the following that the error on the defocus distance is by far the dominant error for our application.

Camera pixel scale The camera pixel scale is needed to calculate the oversampling factor. An error on this factor induces an error on the coefficients of all radially symmetric aberrations (defocus, spherical aberration ...) as shown in Figure 4.8.

An error of the pixel scale is essentially propagated to the defocus aberration estimation. A slight error can be seen on spherical aberration but remains negligible in comparison to the one on the defocus. In Figure 4.9 the evolution of the estimation error of the defocus coefficient is plotted as a function of a pixel scale measurement error. It is assumed that the true value is 13.25 mas as measured during the first on-sky tests of the AO system. Since the accuracy on the pixel scale measurement is better than 0.2 mas , one can estimate the wavefront error (WFE) due to this uncertainty to be less than a few nanometers and therefore to remain negligible.

Pupil shape An exact knowledge of the pupil shape (diameter, central obstruction, global shape) is required. In particular, few percent of mis-alignment of the pupil leads to an error of a few tens nanometers on the phase estimation.

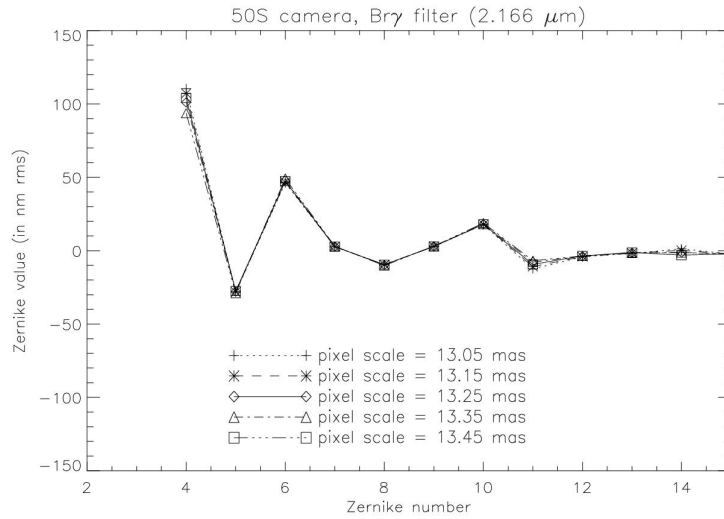


Figure 4.8: Influence of the pixel scale error on estimated aberration by phase diversity. Experimental data have been used. The CONICA camera C50S and the narrow band filter Br γ are used. The focused and defocused images are obtained using the 0-4 pinhole pair. For the same couple of images several pixel scales (from 13.05 to 13.45 mas) serve as input parameter for the PD algorithm.

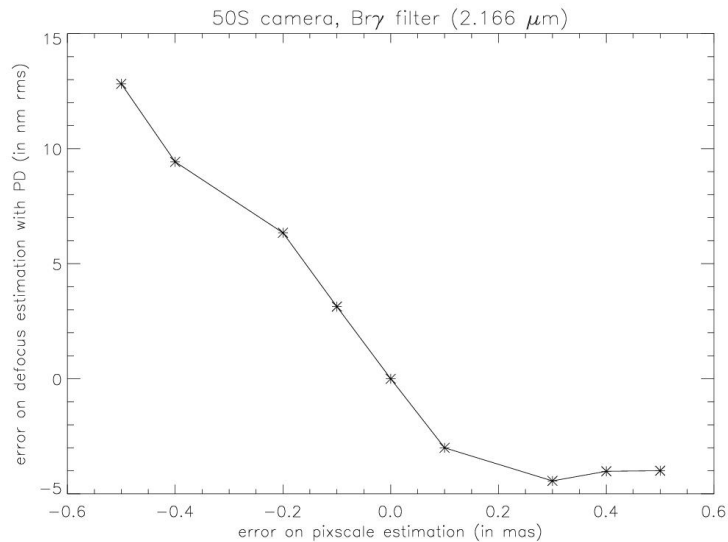


Figure 4.9: Influence of the pixel scale error. The reference value is set to 13.25 mas. For this value it is *assumed* that the error on the defocus coefficient estimation is zero (the experimental conditions are the same as in Figure 4.8).

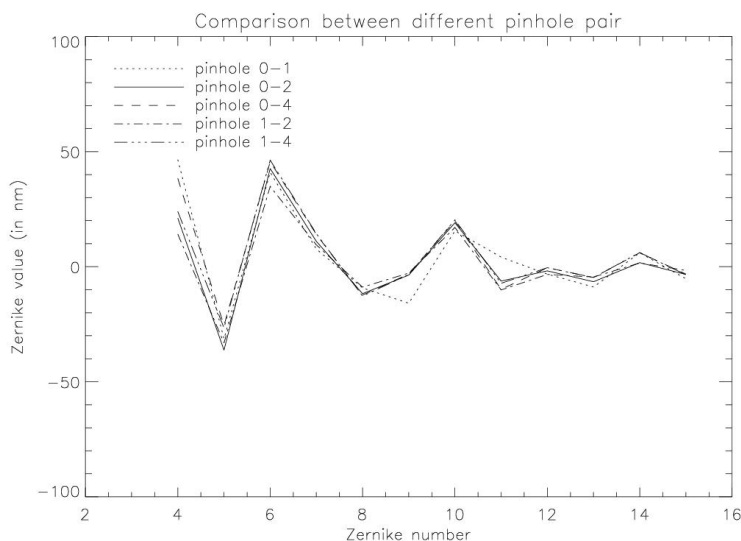


Figure 4.10: Comparison of the estimated aberrations of various pinhole pairs. Camera C50S with FeII narrow band filter ($1.644 \mu\text{m}$).

Differential object structures The algorithm is based on the assumption that the same object is used to obtain the focused and the defocused image. If two different objects are used (case of CONICA pinholes), errors could be induced if they are not completely identical.

Figure 4.10 shows for the narrow band filter FeII ($1.64 \mu\text{m}$) and the objective C50S the estimated aberration for different pinhole pairs. It shows a good agreement between all the pinholes, except for the pinhole pair 0-1. The discrepancy in the estimated aberrations can probably be attributed to the small defocus distance. Disregarding the pair 0-1, the good agreement of all the other pairs leads us to assume the pinholes close to be identical. Indeed, the main part of the WFE is due to the defocus coefficient and highlights the uncertainties on pinhole positions as already mentioned in Sect. 4.1.4.1.

Translation in the entrance focal plane The maximal detector translation along the optical axis is not enough to introduce significant diversity between focused and defocused images. For the calibration of CONICA aberrations, we introduce defocus by translating “the object” in the entrance focal plan. As we said before (Sect. 4.1.1.3), this implementation does not create exactly a pure defocus. In order to quantify the deviation from a pure defocus, we estimate the effect of a translation of 4 mm in the entrance focal plan by using the optical design software ZEMAX. The object shift induces a defocus $a_4^d = 641.5 \text{ nm}$ and a negligible spherical aberration $a_{11} = 0.14 \text{ nm}$. The deviation from a pure defocus is very small and thus can be neglected.

Field aberrations The images obtained by the pinhole 1 and 2 are not located at the same position on the detector than those obtained by the pinhole 0 and 4 (separation of 100 pixels in y). It induces that some focused and defocused images (for example pair 0-1 and 0-2) do not see exactly the same aberrations. The evolution of the field aberrations are evaluated by optical calculations using ZEMAX. The comparison of the aberrations at the center and at the upper left corner of the detector (separation of 500 pixels in x and 500 pixels in y) shows that the main influence concerns the astigmatism a_5 which

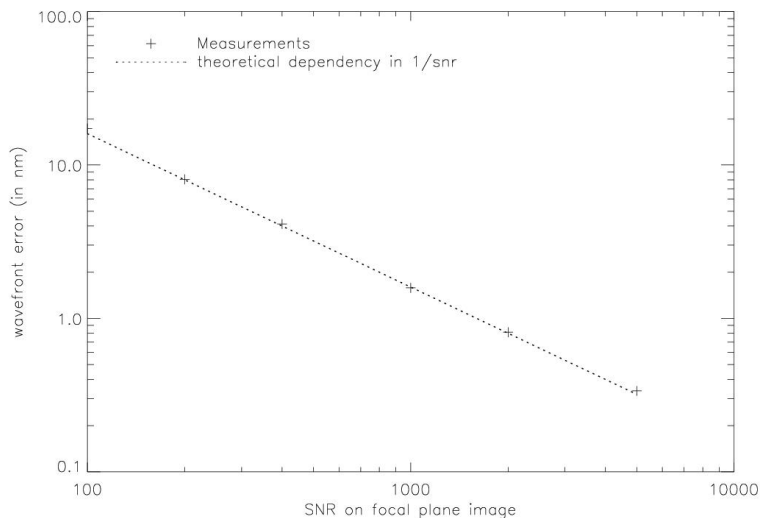


Figure 4.11: Evolution of the wavefront error as function of SNR on focal plane image. Simulation presented in Sect. 4.1.3 have been used. A $1/\text{SNR}$ theoretical behavior is plotted for comparison.

increases by 20 nm (the variation of all other aberrations are less than few tenth nanometers). The focused and defocused images are separated by 100 pixels (this distance is five times fewer than the one uses for the theoretical calculation), thus even for the astigmatism, the influence of the field aberration evolution is negligible.

4.1.4.2 Image limitations

Signal to Noise ratio The accuracy of the PD algorithm is directly linked to the signal to noise ratio in the images (the definition of SNR is given in Sect. 4.1.3).

We present in Figure 4.11 the WFE error evolution as a function of image focal plane SNR. This figure, obtained on simulated data, shows the perfect agreement between simulation and expected (theoretical) $1/\text{SNR}$ behavior (Meynadier et al. 1999). For the NAOS-CONICA aberration estimation it has been checked that the SNR is high enough to make this error source negligible in comparison to the others since the typical values of SNR are greater than a few hundred. That leads to a WFE of a few nanometers due to signal to noise ratio. This has been experimentally checked on one set of data. Four pairs of focused-defocused images have been recorded sequentially in the same CONICA configuration (FeII filter and camera C50S). The SNR on these images is 400. Aberrations are then estimated for each couple and the WFE fluctuation on this four set of coefficients is equal to 2.2 nm RMS, which is in perfect agreement with Figure 4.11 (obtained on simulation).

Residual background features The principle of the PD method is the minimization of a criterion (Equation 4.10) which is based on a convolution image model (Equation 4.1). Thus the image should be perfectly corrected for all instrumental features (background, dead pixels, etc.) in order to match the model. In practice, residual features are still present. In particular, in the case of CONICA images, a background fluctuation due to pick-up noise can induce residual features on the images even

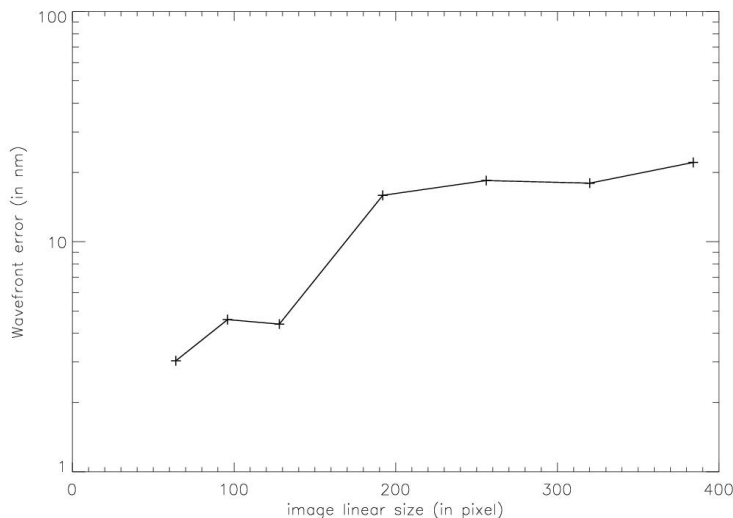


Figure 4.12: Evolution of the wavefront error as a function of the image size. Experimental data have been used.

after a proper background calibration (see Sect. 4.1.5.2). These features are interpreted as signal by the phase-diversity algorithm. Therefore they induce bias on the aberration estimation. The effect of such fluctuations is highlighted in Figure 4.12 on experimental data. The difference of the PD results obtained with and without residual background features yield the WFE which is plotted as a function of the image size. This can be understood as a function of the residual background influence, too, because it obviously depends on the image size: the smaller the images, the less important the residual background in comparison to the signal. Nevertheless, the image size should be large enough to contain the whole signal. Furthermore, the modelisation of the pupil shape (see Sect. 4.1.4.3) must also be taken into account to choose the right image size. In Sect. 4.1.5.2 we describe a pre-processing algorithm which allows to remove these residual background features.

Number of estimated Zernike polynomials As presented in Sect. 4.1.1.3, the phase regularization in our algorithm is provided by a truncation of the solution space through the use of a finite (and small) number of unknowns (typically the first twenty Zernike coefficients). Figure 4.13 shows, on experimental data, the influence of the number of estimated Zernike on the reconstruction quality.

There exists a limit to the number of Zernike polynomials that can be estimated with a reasonable accuracy. Of course this limit depends on the signal to noise ratio on the images. In the present case, this number is equal to 36. Note that if a more sophisticated regularization term is introduced in the PD algorithm both on the object and the aberrations this limitation should be overcome. Nevertheless such a regularization is not needed here since the aberration amplitudes are negligible (less than a few nanometers) for Z_i above $i = 11$ (i.e the spherical aberration). Note that the WFE between Zernike number 15 and 36 is about 1.3 nm RMS, which is a very good precision.

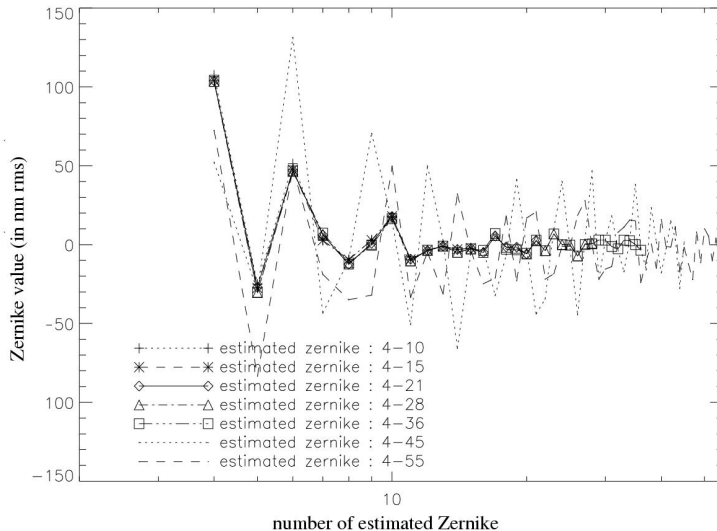


Figure 4.13: Evolution of the aberration estimation as a function of the number of Zernike in PD algorithm. Experimental data have been used.

4.1.4.3 Algorithm limitations

Spectral bandwidth The phase diversity concept proposed here is a monochromatic wave-front sensor (theoretically the concept can be applied on polychromatic images but it induces an important modification of the algorithm to model the data (Seldin and Paxman 2000)). Nevertheless it has been shown (Meynadier et al. 1999) that the use of broadband filters does not significantly degrade the accuracy as long as $\frac{\Delta\lambda}{\lambda}$ is lower than a few tens of percents (typically $\frac{\Delta\lambda}{\lambda} \leq 0.15$)

Image centering As mentioned above, the PD algorithm can not estimate a tip-tilt between the two images larger than 2π . Therefore, a fine centering between focused and defocused images must be done before the aberration estimation (see Sect. 4.1.5.2).

Pupil model Since we consider here experimental data (see Sect. 4.1.5), the modelisation of the pupil shape in the algorithm is critical, in particular the pixelisation effects. Indeed, in PD algorithm the pupil definition depends on the image size and on the oversampling factor. For example, images of camera C50S in K band oversample with a factor of 2 and a 32×32 image will lead to a pupil diameter of 8 pixels (see Figure 4.14). In this case, the pixelisation effects on the shape of the pupil will induce aberration estimation error. These effects are illustrated in Figure 4.15.

Therefore, large images are recommended to well model the pupil and to obtain accurate results. Nevertheless, two problems may occur with the processing of large images:

- a residual background problem (see Sect. 4.1.4.2). The larger the image, the more important the effects of residual background unless the images are tapered outside their central region.



Figure 4.14: Pupil shape in the PD algorithm for three numbers of pixel used in the pupil sampling [8, 32, 64 and 256]. The oversampling factor of 2 in K band leads to corresponding image sizes equal to [32, 128, 256 and 1024].

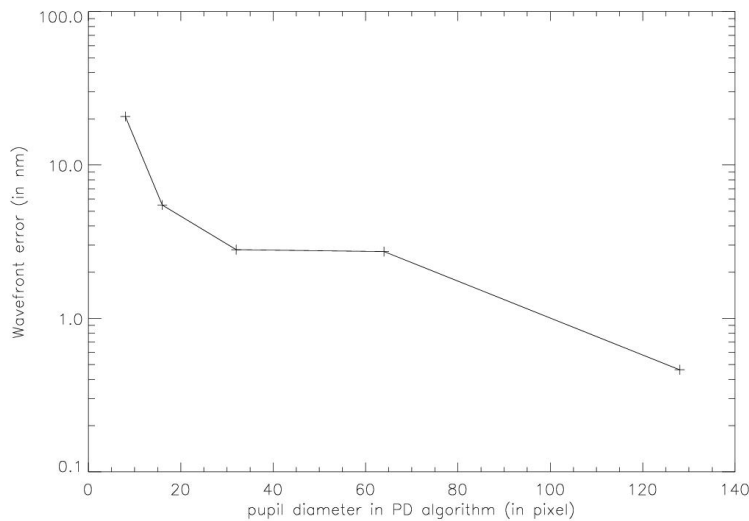


Figure 4.15: Evolution of the wavefront reconstruction error as function of pupil sampling in PD algorithm. The x axis gives the pupil diameter in pixel in the PD algorithm.

- a computation time problem. Because of the iterative resolution of criterion defined in Equation 4.7, the increase of images size will lead to a increase of computation time.

This highlights the choice of a good compromise between pupil model in the PD algorithm to avoid phase reconstruction error and a reasonable image size.

The evolution of the reconstruction error as a function of pupil sampling is presented in Figure 4.15. To minimize the residual background effects, all the background pixels (that is pixels with no PSF signal) has been put to zero in the images.

Considering the results shown in Figures 4.15 and 4.12 along with the computation load lead us to choose an image size equal to 128×128 pixels for the K band and 64×64 pixel for the J band.

4.1.4.4 Conclusion

In this part, we have analyzed and quantified, on experimental and simulated data, the possible sources of errors in the static aberration estimation for NAOS-CONICA. It is shown that the main source

of errors is due to an imperfect knowledge of the system (that is calibration errors). In particular a precise knowledge of the defocus distance between focused and defocused planes is essential.

If very high precisions are required on the estimation and on the correction of static aberrations (for instance in the case of a future very high SR AO for exo-planet detection), the PD must be taken into account in the early design of the system in order to optimize with respect to the constraints and error sources listed above.

4.1.5 Practical example

In this section we give a detailed description on a practical example of the global procedure used to estimate NAOS-CONICA static aberrations. This procedure is quite general but the particularities of the CONICA and NAOS dichroic aberration measurements are underlined. All the illustrations are obtained for the following configuration of CONICA: objective C50S (pixel size equal to 13.25 mas) and Br $_{\gamma}$ filter.

4.1.5.1 Input data

The input data are a focused and a defocused image ($\mathbf{i}_{1,2}$) with their associated backgrounds ($\mathbf{b}_{1,2}$) and a known defocus distance expressed in mm in the entrance focal plane of CONICA. This distance is given by the pinhole choice in the case of CONICA measurements (see Table 4.2) or by the defocus introduced by the DM in the case of the NAOS dichroic aberration measurements. In the example we consider the first approach and introduce the defocus by the pinhole choice.

4.1.5.2 Pre-processing

The pre-processing of the images is required before the wavefront can be estimated. We split the pre-processing in several steps:

- Conventional background subtraction in order to remove the main part of detector defects (bad pixels, background level, possible background features, etc.):

$$\mathbf{i}_{1,2}^{corr} = \mathbf{i}_{1,2} - \mathbf{b}_{1,2} \quad (4.15)$$

The division by a flat-field pattern is recommended to increase the accuracy of the results even if it is not done in this example.

- The focused and defocused images are re-centered by a correlation procedure. For each filter we computed the relative shifts of the PSFs against each other. The median of these shifts was determined and serves to re-center the defocused images. This procedure ensures that re-centering is accurate enough to obtain a relative tip-tilt between the two images lower than 2π .
- Removing of the residual background feature: the most important feature is a residual sine function in vertical direction due to pick-up noise. Its amplitude is greater than the noise level. An estimation of the residual background features is necessary and performed directly on the images using a median filter in horizontal direction applied to each image column. A comparison of the images before and after this residual feature removal is presented in Figure 4.16.

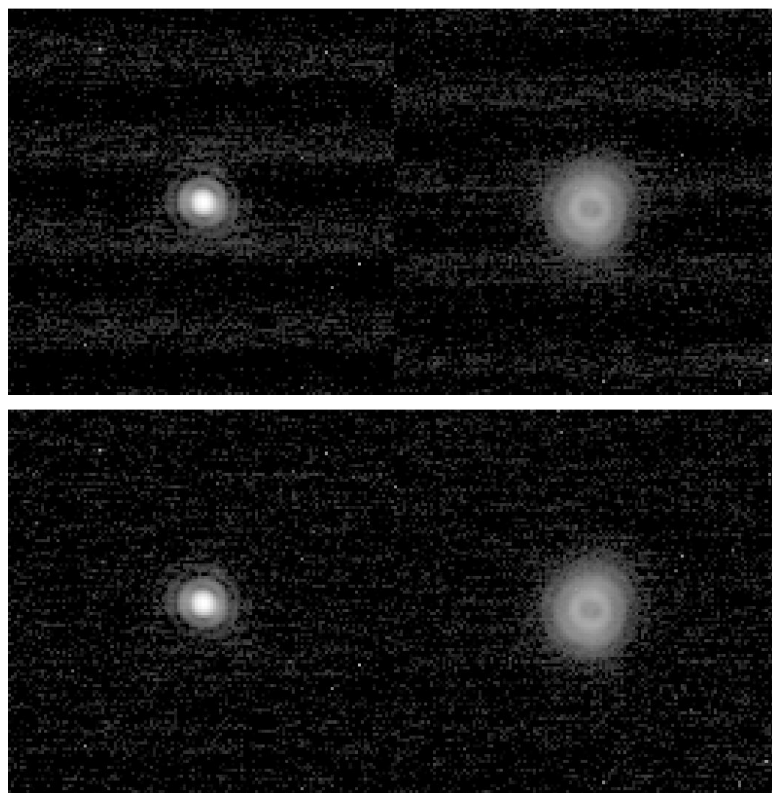


Figure 4.16: Comparison of focused and defocused images before (on top) and after (at the bottom) the application of an algorithm which removes residual background features (log scale). The estimated SNR is equal to 400.

Table 4.4: Measured aberrations (in nm RMS) for the CONICA camera C50S and the Br γ filter. The defocus distance between the two images is 4 mm and the estimated SNR is 400. Only the 12 first Zernike 4-15 are given. The raw values are obtained without residual background subtraction. The corrected ones are obtained after subtraction of the residual background features.

Zernike coefficient (nm)	4	5	6	7	8	9	10	11	12	13	14	15
Raw	91	-27	48	3	-9	-4	19	-20	-5	-1	1	-2
Corrected	112	-24	47	1	-5	-1	17	-19	-3	-2	-3	-3

- Image windowing: the image size is a trade-off between a good numerical pupil modeling and a reasonable computation time. We achieve reliable results by using 128 \times 128 frames.

Note that we have assumed that all the bad pixels have been removed by the background subtraction. If some of them are still present in the pre-processed images, they must be removed by hand to ensure that they do not induce reconstruction errors in the PD algorithm.

4.1.5.3 CONICA aberration estimation

When both focused and defocused images have been pre-processed as described above, the PD algorithm can be applied. The inputs of the PD algorithm are:

- pixel scale: 13.25 mas (camera C50S),
- central obstruction given by the fraction of the pupil diameter: 0 (full pupil),
- wavelength (in μm) : 2.166 (Br γ filter),
- highest estimated Zernike number: 15 (estimation of Zernike polynomials from 4 up to 15),
- defocus coefficient a_4^d (in nm RMS): in the present example, $d = 4$ mm which leads to $a_4^d = -641.5$ nm,
- the focused and defocused images obtained after pre-processing.

The results obtained are summarized in Table 4.4. A bad background correction leads to an important error on the defocus ($\simeq 20$ nm). A comparison between focused and defocused images and reconstructed PSFs from the estimated Zernike is proposed in Figure 4.17. The estimated SR on the 12 estimated Zernike is equal to 87%. It compares nicely to the SR directly computed on the focal plane image, which is equal to 85%.

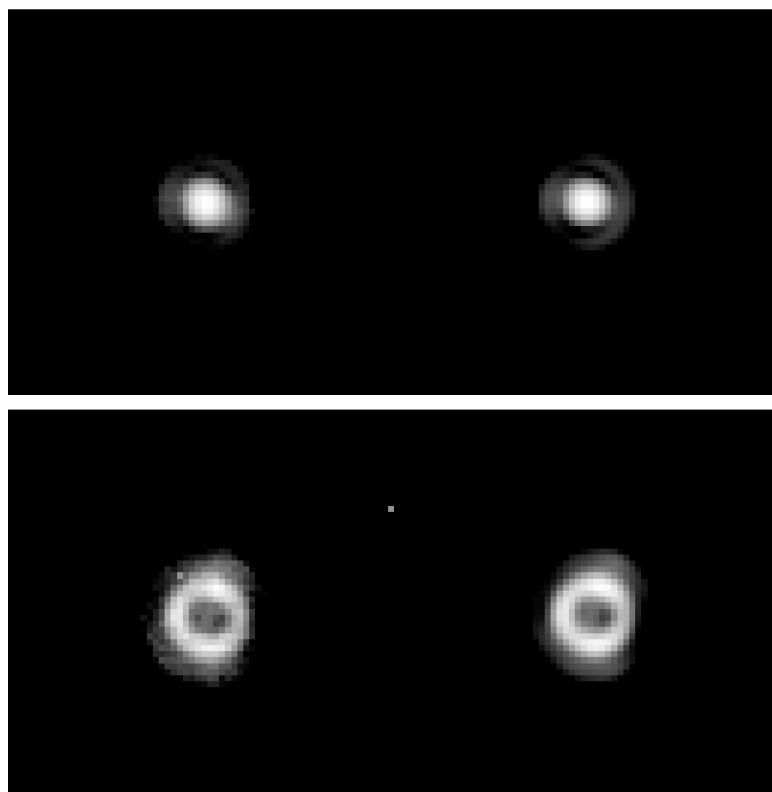


Figure 4.17: Comparison between images (left) and reconstructed PSF from estimated aberrations (right). [up] focused image, [down] defocused image (log scale are considered for each image).

4.2 Experimental Results

In this section we focus on the experimental setup which enables us to calibrate the variety of beam splitters, filters and camera objectives of NAOS-CONICA. The design constraints for the implementation of PD are illustrated, and the resulting setup as well as the procedure to obtain the appropriate input data for PD are described (Section 4.1.2). Because of the huge number of instrument modes it is not feasible to perform the PD calibration for each possible configuration. We explain how the wavefront degradations of the different optical components are disentangled. Then, the individual parts of the optical train can be calibrated separately and it is no longer required to do this for every possible combination. In detail, we will allocate the wavefront error to the dichroic mirrors of NAOS (beam splitter between wavefront sensor and imaging path), to the CONICA filters and camera objectives (Section 4.2.1).

Thereafter, the sensed wavefront errors are used to calculate the corresponding SRs. These are compared to the SRs directly determined from the images and the consistency is verified (Section 4.2.2). Finally, after presentation of the complete calibration procedure and its results, the measured wavefront errors are rendered in terms of Zernike coefficients to the AO system to demonstrate the gain in overall performance after closed loop correction (Section 4.2.3).

4.2.1 Calibration of NAOS and CONICA static aberrations

We have chosen Zernike polynomials to describe the shape of the wavefront in the telescope pupil (Noll 1976). A set of Zernike coefficients indicates the linear combination describing the present wavefront. As a matter of course, we can regard this set of coefficients as a vector. We refer to the Noll notation (Noll 1976) which labels the focus with 4, the tangential and sagittal astigmatism with 5 and 6, coma with 7 and 8, and so on. Since the coefficients for piston (1), and tip-tilt (2, 3) are extraneous to the image quality they are dropped. Figure 4.18 depicts the first basis functions up to coefficient 14. The images were acquired with NAOS-CONICA during integration period in Paris. A calibration point source in the entrance focal plane of NAOS was imaged on the CONICA detector in K-band. Then a wavefront aberration of 500 nm RMS was applied to the DM for each appearing coefficient. The resulting distorted PFSs constitute the basis functions of the chosen coordinate system.

An extensive examination of the variety of error sources due to the practical and instrumental constraints was done in Sect. 4.1.4. The induced aberrations due to defocusing by a shifted object in the CONICA stand-alone case have been simulated and proven to be negligible. The influence of the pupil shape and its numerization have been evaluated, errors taken into account with regard to the camera pixel scale and the defocus distance deviations have been simulated and the problem of different object structure was considered. Furthermore we focused in detail on the handling of data reduction, e.g. the influence of the different noise sources such as readout noise or pickup noise. We stated that all these error sources accumulate to ± 35 nm RMS for the focus coefficient (4). Since the presented calibration data are acquired with an optimized Zernike tool, the expected error should be well below this number. The accuracy of the higher order coefficients has not changed and amounts to about ± 5 nm RMS.

In this section we describe how the overall wavefront error can be decomposed and assigned to its corresponding optical components. Then we present the experimental results for one camera objective and some selected filters of CONICA as well as the results for the dichroics of NAOS.

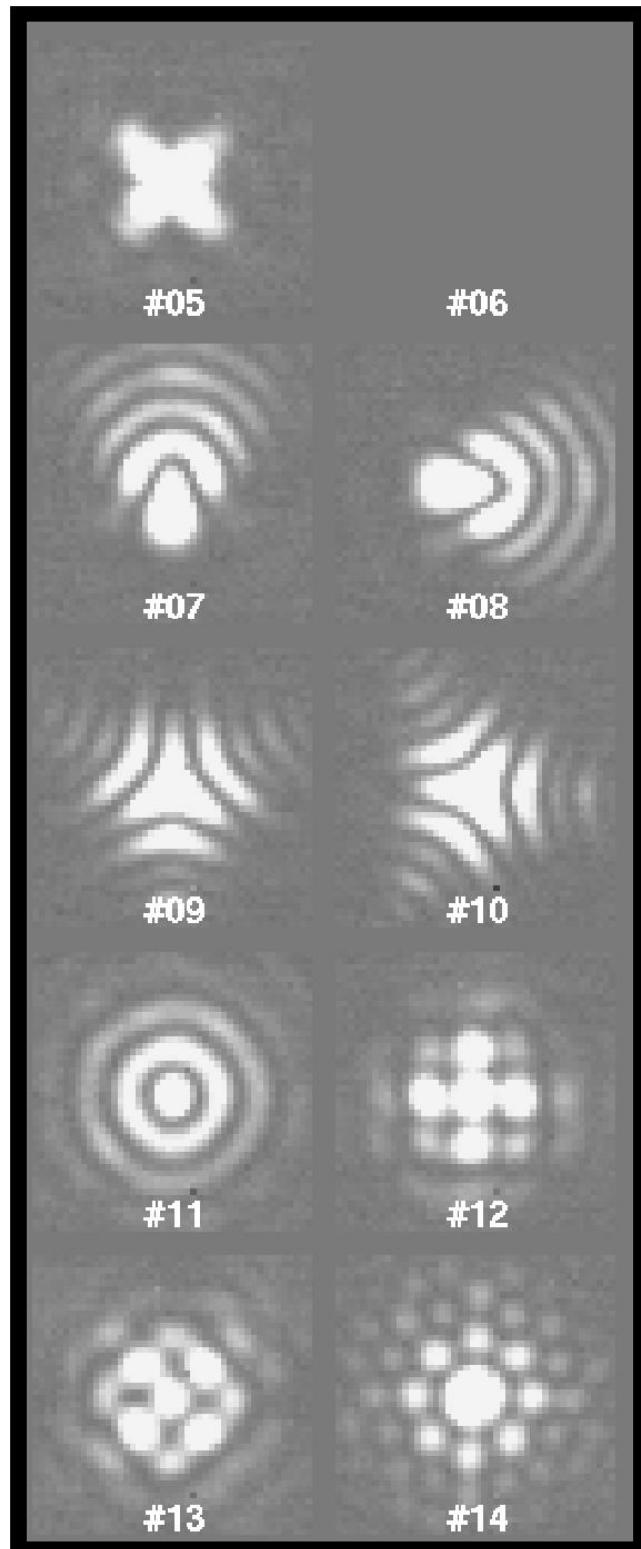


Figure 4.18: CONICA images a point-like source distorted through NAOS. For each shown PSF all Zernike coefficients are zero except for the indicated coefficient that is set to 500 nm RMS. The missing PSF (#6, astigmatism) looks like PSF #5 turned by 45°.

4.2.1.1 Disentanglement of the wavefront errors

In the preceding sections we described how the static non-common-path wavefront error can be measured, whether for CONICA stand-alone or for the entire instrument NAOS-CONICA. However, each determination of the wavefront error is only valid for the particular instrument configuration in which it was measured. The tremendous number of instrument configurations³ makes it impractical to perform these calibrations for any possible instrument setup. For a practical application we need to split up the measured wavefront aberrations and assign the corresponding contributions to the divers optical components. This allows the construction of a configuration table⁴ with entries for each optical component of the instrument. When a special instrument configuration is selected, the corresponding wavefront error contributions can be read out, added together and delivered to the AO system. This enables the DM to pre-correct for the current static wavefront aberrations. Even if this procedure applies only on-axis in a strict sense, we have proven the field dependencies to be negligible (Sect. 4.1.4.1), and may thus compensate with a constant wavefront for the whole FOV.

In principal, we have to differentiate between three categories of optical components in the imaging path: the NAOS dichroics, the CONICA filters and the camera objectives.

The contribution of the NAOS dichroics a_i^{dichro} can be determined by subtracting the overall NAOS-CONICA instrument aberrations a_i^{NCtot} from the total CONICA instrument aberrations a_i^{Ctot} :

$$a_i^{\text{dichro}} = a_i^{\text{NCtot}} - a_i^{\text{Ctot}} \quad (4.16)$$

The vector components are labeled by the Zernike number i running in our case from 4 to 15. Regarding the PD estimations of the different CONICA filters for one camera objective (see Fig. 4.19 and Section 4.2.1.2) we ascertain that generally the filter aberrations a_i^{fil} are small and mainly the achromatic camera objective aberrations are seen. In any case the filter aberrations are not correlated with each other nor with the camera ones. This suggests that we can deduce the camera objective contribution by applying the median to the total CONICA internal aberrations $a_i^{\text{Ctot,fil}i}$. We prefer the median instead of the mean to avoid taking into account highly aberrant filters. The filter i which was used to determine the corresponding total CONICA internal aberration a_i^{Ctot} is indicated by $\text{fil}i$. The camera objective and the residual filter contributions are obtained by these relations:

$$a_i^{\text{cam}} = \text{median}(a_i^{\text{Ctot,fil1}}, a_i^{\text{Ctot,fil2}}, \dots, a_i^{\text{Ctot,fil}n}) \quad (4.17)$$

$$a_i^{\text{fil}} = a_i^{\text{Ctot}} - a_i^{\text{cam}} \quad (4.18)$$

The separation of the wavefront aberration into the contributions associated with the three categories of optical components (NAOS dichroics, CONICA filters and camera objectives) is only possible when we make use of *both* ways to introduce a focus shift, i.e. the DM to determine the NAOS-CONICA overall aberrations and the Zernike tool to determine the total CONICA aberrations. In addition, we note that even if we refer to these three categories by the notation dichroics, filters and objectives, the other components in the optical path are included, as well, even when they are not mentioned explicitly. E.g., the aberrations of the CONICA entrance window are included in the dichro aberrations and the aberrations of the CONICA collimator are an inextricable part of the camera aberrations.

³Given the combinations of 5 NAOS dichroics, 40 narrow and broad band filters and 7 camera objectives!

⁴In fact, a configuration file is generated. The instrument control software takes care of what coefficients have to be applied for the selected instrument setup. These processes are hidden and completely automatic.

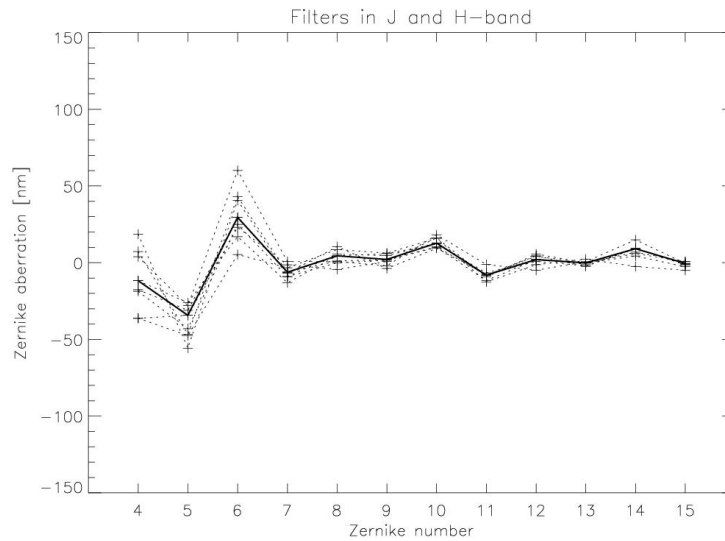


Figure 4.19: CONICA internal aberrations measured by 8 NB filters in J- and H-band with camera objective C50S and pinhole pair 0/2 mm. The thick line indicates the median representing the camera aberrations.

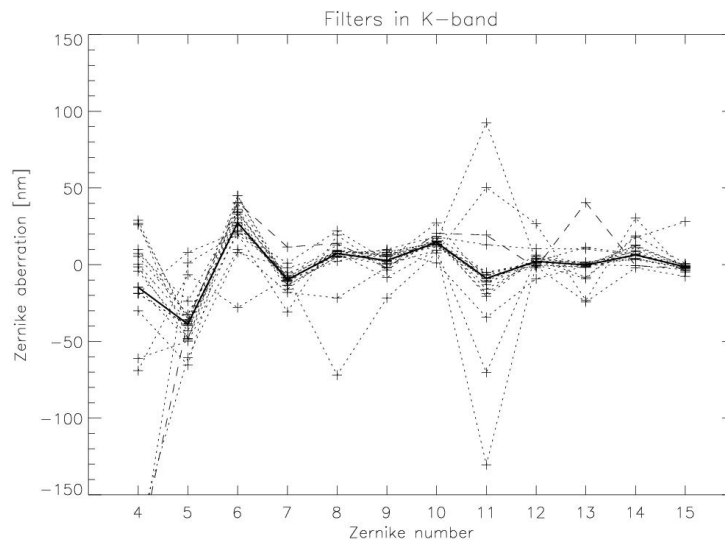


Figure 4.20: CONICA internal aberrations measured by 19 NB filters in K-band with camera objective C50S and pinhole pair 0/4 mm. The thick line indicates the median representing the camera aberrations. The dashed line highlights the aberrant filter NB2.09 which is picked out for the demonstration images in Fig. 4.21.

4.2.1.2 Calibration of CONICA: camera and filters

Fig. 4.19 shows the aberrations for all eight narrow band filters in J- and H-band of CONICA. The camera objective C50S and the pinhole pair (0/2 mm) is used to obtain the calibration data. The fourth coefficient $a_4^{\text{Ctot,fil}}$ expressing the defocus shows a peak-to-peak variation of up to 60 nm. This

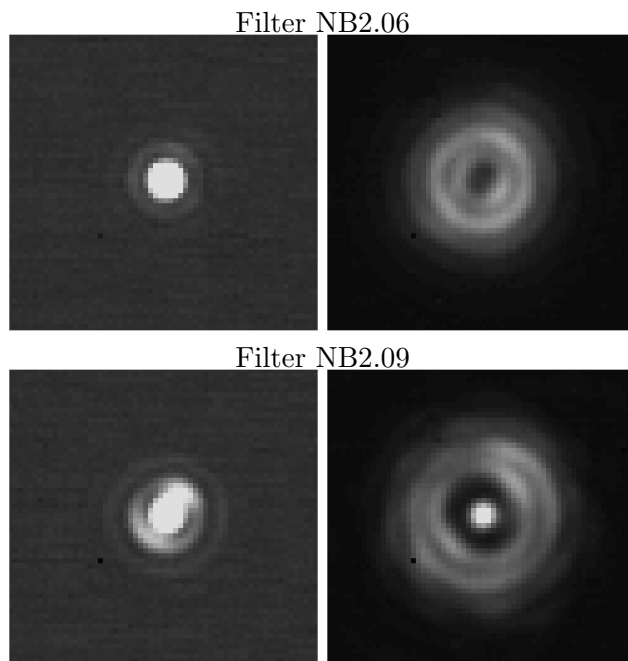


Figure 4.21: Comparison of PD input images of a filter with small aberrations (NB2.06, on the top) and a filter with high aberrations (NB2.09 at the bottom). The in-focus images are placed on the left side, the out of focus images on the right side. The defocus distance is 4 mm for both filters ($f/15$).

implies a slight imprecision of coplanarity of the filters in the cold environment. The other measured coefficients associated with the different filters noticeably resemble each other. This is evidence that these narrow-band filters contribute little to the total aberration of the system and mainly the camera objective aberration is seen.

Fig. 4.20 displays the calibration results in the K-band. In total, 19 filters have been calibrated using the pinhole pair 0/4 mm. One of the strongly aberrant filters (NB2.09) is highlighted by a dashed line. A large defocus in comparison to the other ones is detected. This filter is expected to have a striking error of coplanarity. It is not surprising that the strong defocus comes along with a particularly high spherical aberration ($i = 11$). The other highly aberrant filters show the same behavior in comparison with the common filters of minor aberrations. The spherical aberration expresses the next order of a radial symmetric Zernike mode. The probability that a strong default of coplanarity induces only a defocus and does not concern higher orders is small. The PD input images of this aberrant filter is depicted at the bottom of Fig. 4.21. The right image shows the PSF registered in focus, and the left image a PSF having introduced a defocus of 4 mm. Already the in-focus image reveals a strong degradation, but especially the phase inversion due to the high defocus can be clearly seen in the out of focus image. A bright spot emerges in the center of the “donut”. On the top of this couple of images another couple of images is depicted. These are the PD input data of a filter (NB2.06) with normal behavior and without strong aberrations.

As described in Section 4.2.1.1 the median of each Zernike number of the whole set of vectors yield the vector describing the camera contribution.

The accuracy of separating the camera aberrations from the raw aberrations (filters including camera) by the method described above is striking. The median aberrations for the filters of the

Table 4.5: Camera aberrations in nm RMS by the median over the filter + camera aberrations in the bands J, H (pinholes 0/2 mm), K (pinholes 0/4 mm) and all bands (J, H, K).

Bands for	4	5	6	7	8	9	10	11	12	13	14	15
Median												
J, H	-12	-34	30	-6	4	2	13	-8	2	0	9	-1
K	-15	-39	27	-10	7	3	15	-9	2	0	6	-1
J, H, K	-15	-39	27	-9	6	2	13	-9	2	0	7	-1

two different wavelength regions plotted in Fig. 4.19 and Fig. 4.20 are compiled in Table 4.5. The deviations of both median values are clearly below the expected error (see Sect. ??). Table 4.5 lists these median coefficients taken from all NB filters in J-, H- and K-band. Keeping in mind that the achievable precision is a few nm we state that the camera aberrations are very small. The highest contributions arise from the focus term (4) and the astigmatism (5, 6). Section 4.2.2.3 gives an idea of the impact on the image quality dealing with Zernike mode aberrations in this order of magnitude. The residual filter aberrations are obtained by Equation 4.18. In general, besides the focus coefficient and a few deviating filters these values are close to zero, too.

4.2.1.3 Calibration of NAOS: dichroics

The calibration data are obtained with the fiber at the entrance focal plane of NAOS using the adaptive optic system itself for defocusing (see Sect. 4.1.2.2). Since the Zernike coefficients for the NAOS dichros are determined differentially, i.e. by subtraction of the total CONICA aberrations from the NAOS-CONICA overall aberrations, we can choose any reference camera and filter to perform the measurements as long as the components stay the same. A good choice is camera objective C50S and filter FeII1257. This objective oversamples even in the J-band and the filter has a small wavelength and therefore yields a higher accuracy in sensing wavefront errors. A suitable distance for the focus shift at this filter wavelength in the f/15-beam is 2 mm. We can calculate suitable defocus distances using Equation 4.14.

In the following the properties of the five NAOS dichroics are itemized:

- VIS: Visible light to WFS; J, H, K, L and M to CONICA
- N20C80: 20 % of the incoming light to WFS; 80 % to CONICA (J, H, K)
- N90C80: 90 % of the incoming light to WFS; 10 % to CONICA (J, H, K)
- K: K to NAOS; J and H to CONICA
- JHK: J, H and K to NAOS; L and M to CONICA

Four of these five dichroics have been calibrated. The dichroic JHK is omitted since only light in L and M band reaches CONICA. It is unreliable to sense the small wavefront errors of NAOS-CONICA at these wavelengths. Furthermore there is no need to, because the small static aberrations become completely negligible in L and M.

Table 4.6: NAOS dichros, overall NAOS-CONICA aberrations in nm RMS, reference filter: FeII1257.

Dichro	4	5	6	7	8	9	10	11	12	13	14	15
VIS	15	-5	24	-6	23	5	-8	-9	7	-13	-7	3
N20C80	2	-1	42	-2	30	5	-4	14	-1	-19	-8	4
N90C10	-7	-3	36	-3	19	6	-5	-28	1	-9	-9	1
K	-8	14	-17	-4	18	3	-5	-6	7	-14	-10	2

Table 4.7: Separate NAOS dichro aberrations in nm RMS.

Dichro	4	5	6	7	8	9	10	11	12	13	14	15
VIS	-18	37	-5	3	16	2	-21	-44	6	-13	-14	6
N20C80	-32	41	13	8	23	1	-17	-21	-3	-18	-15	6
N90C10	-41	38	7	7	12	3	-18	-64	-1	-9	-16	4
K	-42	56	-47	5	11	-1	-18	-42	5	-14	-17	5

The calibration results are compiled in Table 4.6 and Table 4.7. The first table lists the direct PD results. Any correction performed by these coefficients would only apply to the instrument configuration that was used to obtain the calibration data. The second table lists the aberrations directly assigned to the dichroics. These were obtained by subtracting the total CONICA aberrations that have been measured with the same filter and camera objective using the Zernike tool. It is noteworthy that the sensed astigmatism (Zernike number 5, 6) in the separated case is higher than in the overall case. Obviously a part of the camera astigmatism is compensated by the dichroics.

It is noteworthy that this tendency applies for all dichroics. Different reasons can cause this behavior. First, the inclination of the dichroics artificially introduce an astigmatism. Even if the NAOS dichroics are designed for prism shape and do correct for this effect, a residual error cannot be excluded. Furthermore a certain amount of astigmatism can be introduced by components other than the dichroics lying in the same part of the light path, e.g. the parabolic output folding mirror or the CONICA entrance window (see Fig. 2.1). Nevertheless, it is not a limitation of the calibration method but only a question of assigning the contribution of the wavefront errors to the different optical components. In the end, only the sum of all aberrations has to be correct.

4.2.2 Image quality versus estimated aberrations

4.2.2.1 Strehl ratios by PD and focal plane image

The PD calibration data can be used to investigate the available image quality in different ways. First, the knowledge of the wavefront allows us to calculate a SR. After the reduction of the calibration data the wavefront is described by a set of Zernike coefficients. Furthermore, we can just refer to the in-focus image and calculate a SR with the measured point spread function. In the following we give a more detailed explanation of how these SRs are obtained.

Strehl by PD For small wavefront deviations the SR can be determined via the coherent energy referring to the wavefront variance σ^2 in radian. The PD estimation yield the wavefront expanded in terms of Zernike coefficients a_i . For small σ^2

$$SR \simeq e^{-\sigma^2} \simeq 1 - \sigma^2 \simeq 1 - \sum_{i=4}^m a_i^2 \quad (4.19)$$

allows us to calculate the SR directly by the output of PD estimation. In principal the sum runs to infinity ($m = \infty$) but for our purpose we stop at $m = 15$. We can compare these SR numbers to the ones that are directly determined by the in-focus images.

Strehl on image A straight-forward way to calculate a SR on the focus image (PSF) is to construct a theoretical diffraction-limited image PSF_{diff} taking into account the wavelength, the pixel scale, the aperture and the central obscuration.⁵ Having normalized the total intensity of the PSF and PSF_{diff} to 1, the fraction of these values yields the SR (see Equation C.1).

In particular, in the case of the PSF sampling being close to the Nyquist criterion this approach has the disadvantage of being sensitive to the exact position of the PSF peak with respect to the pixel center. Furthermore, since the total intensity has to be determined by the integrated signal over a wider region around the PSF, the reliability of the SR value depends on a precise background correction. If the background is overestimated, then the SR will be overestimated, too, and vice versa. The reliability of the SR values can be enhanced when we switch from the image space to the Fourier space by

$$SR = \frac{PSF(\alpha = 0)}{PSF_{\text{diff}}(\alpha = 0)} = \frac{\int OTF(f)}{\int OTF_{\text{diff}}(f)}, \quad (4.20)$$

where OTF is the optical transfer function. Since in Fourier space only spatial frequencies are considered, a shift of the PSF is of no importance anymore. Aside from that, an elegant and reliable background correction can be performed using the zero spatial frequency. We

calculate the SRs by the following procedure⁶:

- The image is corrected by its corresponding background.
- The OTF is calculated. It is given by the real part of the Fourier transform of the image.
- The residual background is corrected by the zero frequency. A fit of the very first spatial frequencies is used to extrapolate the true zero frequency value. The difference of the measured and the extrapolated value for the zero frequency yields the residual background.
- The noise level is subtracted using the high frequencies beyond the diffraction limit.
- A theoretical telescope OTF is constructed and multiplied by a Bessel function to account for the spatial spread due to the object size.
- The detector response is taken into account. This is done by a further multiplication of the theoretical telescope OTF with the Fourier transform of the detector response.

⁵The central obscuration which is caused by the secondary mirror will decrease slightly the central peak intensity and raise the side lobes of the Airy function.

⁶This routine was developed by T. Fusco, ONERA

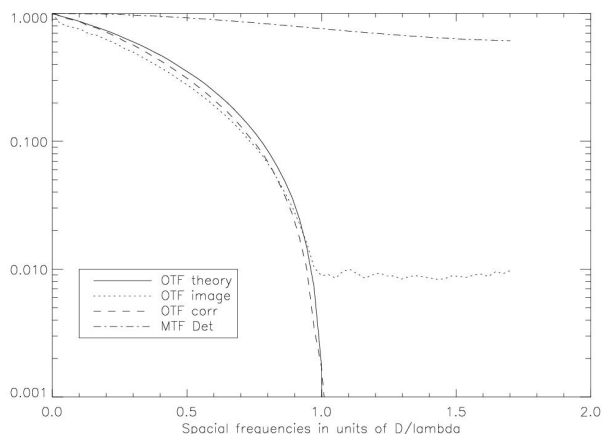


Figure 4.22: Visualization of the theoretical and measured OTF at the example of filter FeII1644.

- The SR is obtained by the division of the normalized integrals from the measured and the theoretical OTF. All points with spatial frequencies higher than the diffraction limit are excluded.

Figure 4.22 gives an example of how the described OTFs look for a PSF taken through the filter H2(1_0)S(7). To allow for a one dimensional representation, the circular mean of the two dimensional OTF is calculated. The raw, untreated OTF of the image is labeled “OTF image”. “OTF corr” displays the image OTF which is corrected for the residual background at zero frequency and for the noise level. The noise level of the uncorrected image OTF can be seen as plateau beyond the cutoff frequency D/λ and averages 1 % of the maximum value. The theoretical diffraction-limited telescope OTF includes the reduction due to the object size⁷ and the correction for the detector modulation transfer function (MTF). It is labeled “MTF Det” and is located at the top of the plot. The detector response is constructed by the assumption that roughly 3% of the total intensity is contained at each of the adjacent pixels and 1.5 % in the corner pixels. Here we refer to Finger et al. (2000). In this paper a measurement of the response of a comparable infrared array is described. Due to the lack of precise knowledge of the detector response it is constructed by a quadratic scaling in relation to the different pixel size.⁸ A quadratic scaling is implied by a linear behavior of the diffusion of the minority carriers in the detector material in one dimension for small distances.

4.2.2.2 Comparison of Strehl ratios

The resulting SRs for the narrow-band filters in J, H, and K are presented in Fig. 4.23 and Fig. 4.24. For each filter two SRs are given: the SR by PD and the SR on the image.

A number of error sources contribute to the error of the SR values on image. Beside of small error contributions due to uncertainties of the pixel scale and the flat-field, the remaining uncertainty of the background correction and the detector response lead us to estimate an absolute error of $\pm 4\%$. The expected wavelength dependency of the MTF error is minor with respect to the remaining background

⁷Since a $10\ \mu\text{m}$ pinhole is used which is barely resolved, the influence is small and amounts for the smallest wavelength ($1\ \mu\text{m}$) at most to 5%.

⁸The pixel size of the CONICA detector (Aladdin 1Kx1K) is $27.0\ \mu\text{m}$.

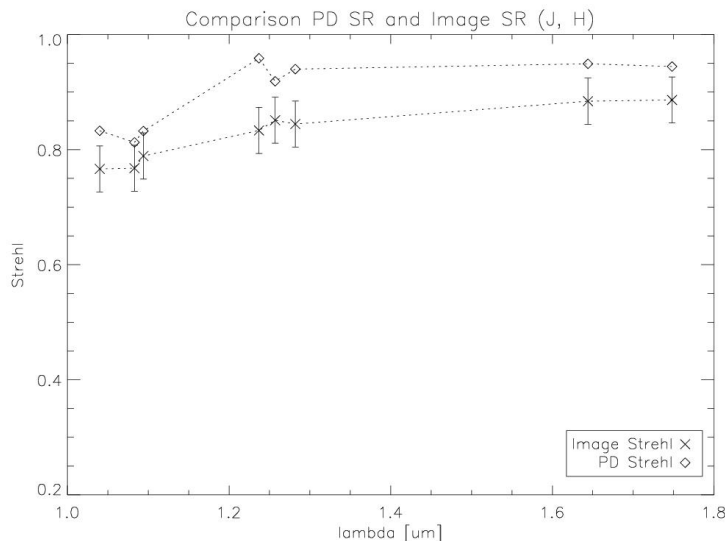


Figure 4.23: Comparison of SR versus wavelength in J and H band calculated directly and derived from PD results.

error. Therefore it is neglected and we use the constant value given above derived from experience in reducing the experimental data.

Recall that the SR by PD has a *maximal* wavelength-dependent error of $\pm 5\%$ at $1\mu\text{m}$ and $\pm 1\%$ at $2\mu\text{m}$ taking into account an error of $\pm 35\text{ nm RMS}$ for the focus estimation ($i = 4$). The main contributor to this error is a systematic error in the precision of the pinhole positions in the Zernike tool (see Section ??).

In general the PD SRs exceed the other SR values. This reflects the fact that the wavefront is expanded by a limited number of Zernike coefficients and the higher order aberrations are cut off. Note that it is not astonishing that in the case of very low SR values (worse than 50%) the PD SR value may lie below the image SRs (Fig. 4.24). Such strong wavefront errors violate the condition under which Equation 4.19 is valid. Thus, we expect Equation 4.19 to yield underestimated values.

The comparison of the SR values determined by the different methods turns out to be consistent. The longer the wavelength, the more the image and PD SR values approach each other. This shows that the influence of aberrations scale with the wavelength. In other words, the fact that we cut off at a certain Zernike number ($i = 15$) has a greater impact at short wavelengths.

4.2.2.3 Focus adjustment

Having in mind the small estimated wavefront errors that we presented in the previous sections we become conscious of the required precision of the most trivial aberration we regard: the focus. It is striking that even in the focus determination we depend on the precision of PD calibration. This becomes evident when we look at the conventional procedure of focus tuning and regard the loss of SR caused by the detected aberrations.

To tune the focus of CONICA, the in-focus pinhole of the Zernike tool is imaged on the detector. Now, a focus curve is obtained by taking images at different axial position of the detector stage (see

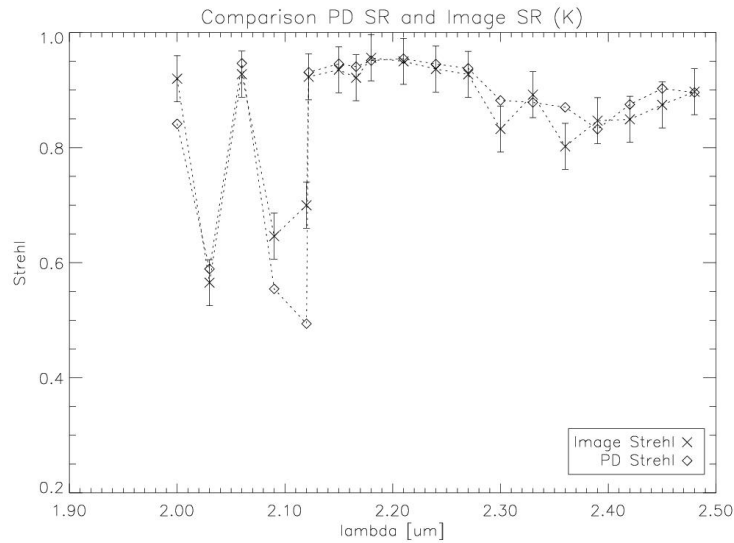


Figure 4.24: Comparison of SR versus wavelength in K band calculated directly and derived from PD results.

Section 4.1.2.1). The maximum of the SRs indicate the proper focus position of the stage. The maximum of the obtained focus curves for the different cameras can be located with an accuracy of about 50 nm RMS. For this wavefront error, Equation 4.19 yields a loss of SR of 2.5 % at a wavelength of $2 \mu\text{m}$ and almost 10 % at $1 \mu\text{m}$. Thus, in particular in the J- and H-band, the inaccuracy of determining the focus only by moving the detector stage gives reason for a significant loss of SR. Furthermore the whole effort of fine-tuning for the remaining static wavefront aberrations becomes irrelevant when the remaining focus error is in the regime of the highest higher-level aberrations (Zernike number $i \geq 5$). Compare the aberrations for focus with astigmatism in Fig. 4.19 and 4.20. The only way to achieve a significant improvement of the wavefront error, and therefore of the SR after closed loop compensation, is to ensure that the residual focus deviation is corrected properly, too. This is guaranteed by following the procedure:

- Determination of the rough nominal focus position of the CONICA detector for each camera with one reference filter. The in-focus pinhole of the Zernike tool serves as a reference.
- Determination of the nominal focus for the whole instrument. The calibration point source in the NAOS entrance focal plane serves as a reference. The data points for the focus curve are obtained by moving the field selector in closed loop. This has to be done for every NAOS dichroic.
- The corresponding data base entries are updated by the nominal focus positions (CONICA internal and NAOS). The nominal focus deviations are included in the data base. They are compensated for by moving the field selector in the case of switching the NAOS dichroics and by moving the CONICA detector stage in the case of switching the camera objectives.
- Then the PD estimation reveals the residual focus error for each configuration, in particular for each filter. They are entered into the data base together with the higher order aberrations. For a certain instrument configuration the corresponding values are fetched automatically and delivered to the AO system. The DM corrects for the residual focus deviations.

4.2.3 Closed loop compensation of NAOS-CONICA static aberrations

4.2.3.1 Rendering of aberrations

Having explored in detail the application of phase diversity to calibrate NAOS and CONICA static aberrations, we presented above the experimental results applying PD as a wavefront sensor. We described how the contributions of the different optical components in the light path are separated to create a complete calibration configuration table. For each possible configuration of the instrument the corresponding correction coefficients are rendered to NAOS and are used to adjust the AO system. In this manner the DM will take the shape needed for compensation of the static wavefront aberrations. To demonstrate the final gain in optical quality we compare the originally acquired images without correction for static aberrations with the images obtained after closed loop compensation. The gain will be quantified in terms of SR numbers.

4.2.3.2 Full AO correction

The 10 μm calibration source in the entrance focal plane of NAOS simulates a star without turbulence. The visible WFS is used to correct for the common path aberrations. Therefore, the loop is closed on the 400 μm source as described in Section 4.1.2.2. The light is separated by the dichroic VIS, thus the WFS sees the visible part and the near-infrared is directed towards CONICA.

Fig. 4.25 shows two extreme cases of applying AO compensation. The upper pictures demonstrate the correction for a filter in J-band, the pictures below in K-band. In accordance with Fig. 4.19 and 4.20 the sensed aberrations in J and K band are very similar - recall that the main contribution arises from the achromatic camera objective and the NAOS dichroic. But even if similar correction coefficients are rendered to the AO system, the effect on the image is strongly wavelength dependent. This is due to the fact that the influence of the applied Zernike coefficients scales with the wavelength. Thus, we achieve a striking correction in J-band visible with the naked eye on the images before and after correction. The most important aberration, the astigmatism, vanishes and the PSF is contracted. In K-band the non-corrected image is already very close to the optimum and the improvement is hard to see directly on the image. But calculating the SRs shows that even in K-band the performed correction is still significant (Table 4.8). Note that the given error arises from a maximum estimate of all error sources as described in Section 4.2.2.2. The nature of the error is mainly systematic (e.g., caused by background correction) and affects the calculated SRs for the image pairs in the same way. SRs determined on experimental data are intrinsically afflicted by rather high error bars, but a direct inspection of the images (central intensity, shape of the diffraction rings) shows the relative gain of 2 to 3% in K-band to be true. Even this rather small appearing gain in K is of high importance. On the way to scientific goals such as e.g. planet detection, the total error budget must be tackled to eliminate every percentage point of loss in SR.

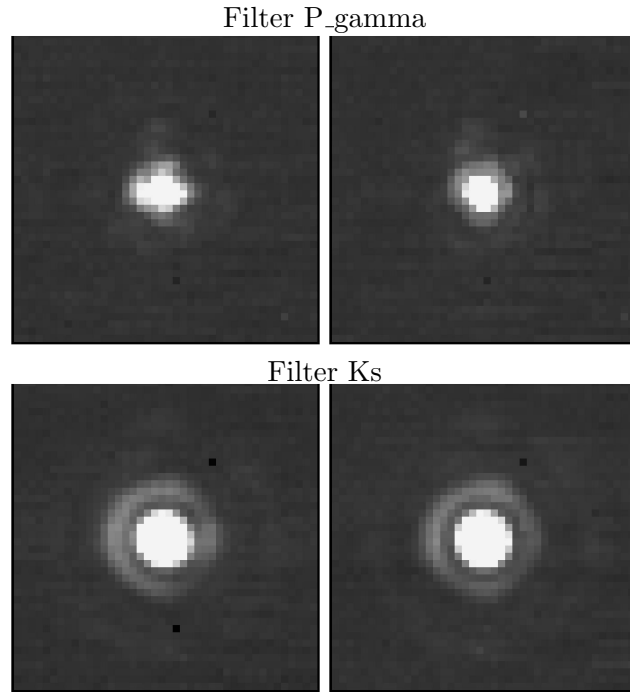


Figure 4.25: Comparison of PSFs before and after closed loop compensation. Above a couple of J-band images and at the bottom a couple of K-band images are shown. Left side: without AO correction. Right side: with AO correction. Especially in J-band, the sharpening of the PSF can be clearly seen.

Table 4.8: Comparison of SRs for two selected filters before and after AO compensation for static aberrations. The maximum mainly systematic error is given. Statistical errors are significantly smaller.

Filter	SR no corr (%)	SR with corr (%)
Pgamma	60 ± 4	70 ± 4
Ks	91 ± 4	93 ± 4

4.3 Conclusion

We have given a precise description of the phase diversity algorithm developed at ONERA and of its use for the calibration of NAOS-CONICA static aberrations. The concept of phase diversity has first been recalled and the expression of the criterion to be minimized was given. The essential parameters of the algorithm have been studied. This has allowed us to highlight the essential verifications and calibrations needed to obtain accurate results with PD.

We demonstrated a simulated example the precision of the estimation under typical SNR conditions of acquisition of NAOS-CONICA images. It turned out that for a SNR of 200, the error on the aberration estimation is less than few nanometers per polynomial. It has been shown that the main source of error is induced by the uncertainty on the pinhole distances which leads to an error on the defocus estimated to ± 24 nm. An other source of degradation is due to the bad knowledge of the pixel scale which contributes for a few nanometers on the defocus. Furthermore, an exact knowledge of the pupil alignment is required to ensure a good estimation of the aberrations. The residual background after compensation in the images is another important source of degradation, estimated to a few tens nanometers. In the case of the images of NAOS-CONICA, the SNR is high enough to make this error source negligible in comparison to the others.

All these error sources lead to an uncertainty on the aberration estimation: about 35 nanometers on the defocus and around few nanometers for the high order Zernike polynomials.

It has been shown that Phase Diversity is a flexible and powerful approach to compute unseen aberration of an AO system and we proposed a guideline for a practical implementation.

Focusing on the instrument NAOS-CONICA, we presented the experimental results of the calibration data for a variety of observing configurations. Especially, we turned our attention to the disentanglement of the measured overall wavefront errors which allows a convenient allocation to the divers optical components and makes the calibration procedure feasible for an instrument with a huge number of possible configurations. The sensed wavefront errors expanded in Zernike coefficients have been used to quantify the image quality in terms of SR and be proven to be consistent with the SRs directly determined with the image data. Finally we gave a striking example of the acquired improvement of optical performance in comparing images with and without AO correction for static wavefront errors. It turned out that even starting with a very good image quality, we still could achieve a significant gain in terms of the SR ratio.

The design of the instrument control software is harmonized with this calibration procedure and the AO loop parameters are automatically updated when the instrument setup changes. This ensures that the utmost optical performance is provided for all the configurations. Additionally, this implementation of wavefront sensing can be used to monitor the optical quality and to alert for small degradations of optical performance. In general, for future high performance AO systems, the presented technique is of great importance to achieve the challenging science goals of the astronomical community. It should be included in the instrumental design at a very early phase.

Chapter 5

A Fabry-Perot Scan of Eta Carinae

This chapter describes the reduction of an FPI scan of Eta Carinae. The data were taken during guaranteed observing time¹ allocated to the NAOS-CONICA instrument consortia. This was a high-risk approach since the Fabry-Perot is not offered by ESO to the astronomical community yet, and no support could be given on the part of the Paranal observatory. Nevertheless, with the expertise of the CONICA instrument team and remote-support, successful observations could be carried out. Even with the very constrained Fabry-Perot observing time, the science verification data demonstrate the exciting research possibilities that will be available with this device.

Just before the FPI sky observations started, the alignment of the FPI was checked and its parameters were calibrated. These technical data were taken in the same time slot and they were used in Sect. 3.8 to describe the calibration procedure and to derive the FPI calibration parameters.

On sky, a scan of the Br γ -line was performed using camera C25S (27 mas/pix). With the aid of Fig. 3.22 the 39th order was selected and the scan values z were predefined to range from 100 to 200 FCU in steps of 10 FCU. For sky subtraction, a data cube with the same parameters was acquired a few arcseconds away from the object. The smallest possible integration time was used (0.3447 sec), and for each FPI scan position, 50 readouts were accumulated. Even applying the minimum integration time, the central source still saturates. In principle, saturation could be avoided by reducing the read time using a small hardware window, or by switching in the shortband neutral density filter.

5.1 Data reduction

No flat-field data were taken, so the data cube is only sky-subtracted. Since accurate photometry is not our objective, we are not constrained by this. Having adjusted the parameters for the observing wavelength, we apply the phase-shift map derived from the argon line to transform the (x, y, z) -cube into the (x, y, λ) -cube as described in Sect. 3.8. Apart from the different central wavelength (2166.12 nm instead of 2062.18 nm) and order (39 instead of 40), the procedure is identical to the one used for the calibration data.

Using the (x, y, z) -cube we generate phase-shift corrected λ -frames with the wavelength ranging from 2160.50 nm to 2170.50 nm in steps of 1 nm. Generating phase-shift corrected λ -frames with shorter

¹GTO data, 14 to 17 Dec 2002, courtesy Tom Herbst.

or longer wavelengths creates frames with missing parts in the FOV. For shorter wavelengths, the interior of a circular region will be undetermined, for longer the exterior of a circular region, according to the deformation of the (x, y, λ) -cube. Intermediate spectral positions are linearly interpolated and the wavelength channel is convolved with the Fabry-Perot's spectral response to account for the undersampling of the wavelength channel.²

To reveal the pure line emission, the continuum must be subtracted from the phase-shift corrected frames. As continuum frame we use the average from the frames at 2160.50 nm and 2170.50 nm. These are the limiting frames of the scanned region (compare e.g. Herbst (1990)). The continuum is depicted in Fig. 5.1. The pure line emission phase-shift corrected frames appear in Fig. 5.2. The wavelength ranges from 2162.50 nm to 2171.50 nm in steps of 1 nm (140 km/sec).

With the aid of the line emission frames, we construct a velocity map. The maximum of the Br γ -line emission along the wavelength channel is determined for the whole FOV (each pixel). To improve the dynamic range of the derived wavelength maxima, a three point neighborhood quadratic fit is performed for the data points along the spectral channel. The maximum defines the relative shift to the center of the vacuum line in the laboratory frame (2166.12 nm, see Allen (2000)). This can directly be translated into projected velocities. Fig. 5.3 shows the resulting velocity map, using a colour scale representation from -3 nm to +7 nm relative to the central wavelength $\lambda_c = 2166.12$ nm (Br γ). To avoid wrong determinations of the wavelength shifts, spectra with maxima smaller than a 1σ error are excluded on the velocity map. These pixels of the FOV are set to -99 and appear black. The 1σ error is determined through the signal fluctuations in the wavelength channel averaged over regions well outside of the Homunculus nebula.

Apart from the velocity map, some examples for spectral analysis with the phase-shift corrected data cubes are given. For demonstration we extract the spectra along one dimension, indicated by the straight line shown in the velocity map (Fig. 5.4). Because of the weak SNR, the (x, y) -coordinates of the data cube are re-binned to 8x8 pixel bins. Having performed the re-bin, the spectra along the indicated line are visualized by the contour plot shown in Fig. 5.5. An abrupt shift of the emission line of about 1 nm (140 km/sec) is detected. Whether the clumpy structure of the contours is real or not cannot be decided for the poor data. It is possible that these are residuals stemming from small photometric differences of the columns of the detector. If this is true, it might be improved with a proper flat-field of the (x, y, z) -data cube.

Fig. 5.6 shows two additional spectra at positions in the field indicated by filled squares in Fig. 5.4. In this case, no re-bin is performed, and thus no artificial reduction of the spatial resolution is introduced. The error-bars of the two spectra represent the 1σ deviation of the wavelength channel, as described above. Recall that the wavelength channel is already convolved with the instrument response. This explains the smooth behaviour of the spectra within the range of the error-bars. Apart from the accommodation for the finite spectral sampling, this will automatically smooth out the spectra, too. Thus, the point-to-point variation appear to be smaller than the error bars. Smooth oscillations of the order of the given error must be interpreted with care. Thus, the right spectrum of Fig. 5.6 clearly represents the line emission and, in this spectrum, no significant Doppler shift is seen. Whereas, from one single spectrum of the type shown in the left of Fig. 5.6, it is not clear whether the double peak is real or not.

²The sampling of the wavelength channel is the same as for the technical calibration data. A value of 1.6 was derived from the argon line rings, significantly below 2 for Nyquist sampling.

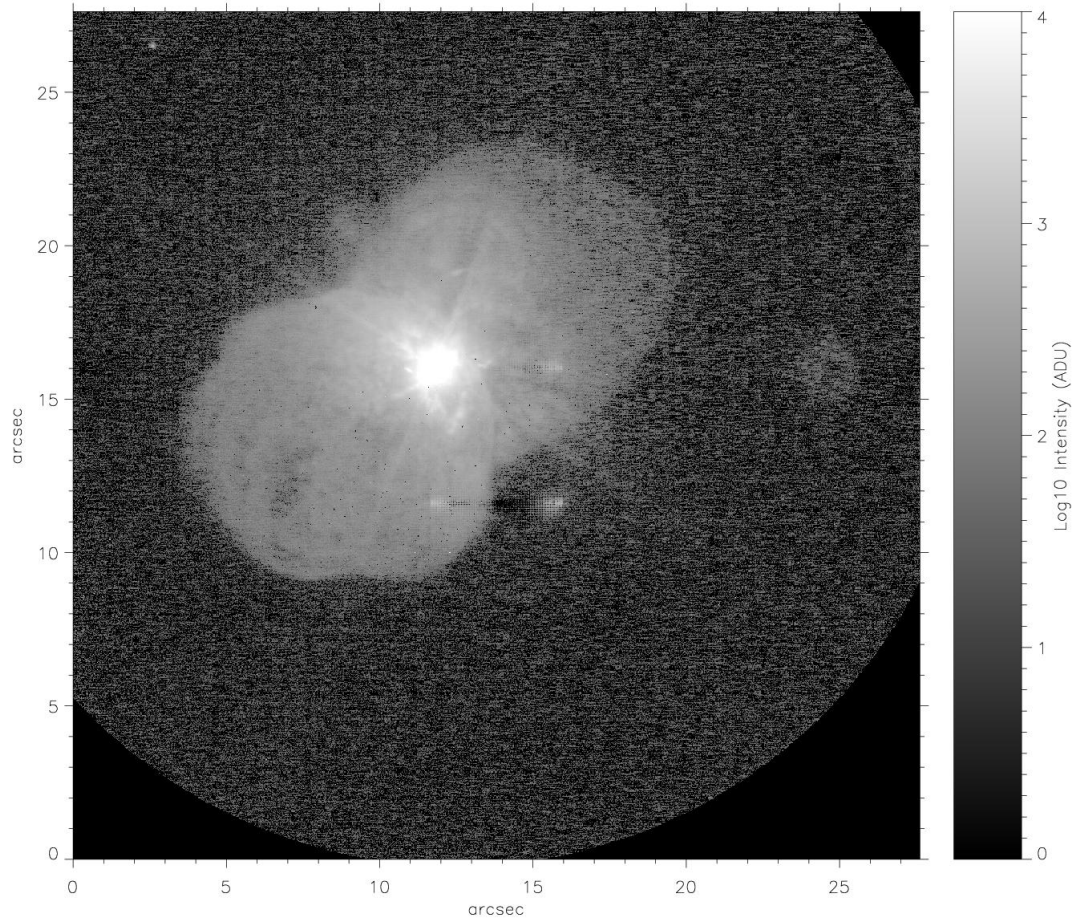


Figure 5.1: Continuum emission displayed with a logarithmic intensity stretch. The continuum frame is created by averaging the limiting frames of the x, y, λ -cube. The three brighter pointlike sources that form a rectangle together with the central object are artifacts produced by crosstalk of the ADC converters due to the highly saturated star. The center of this rectangle coincides with the center of the chip.

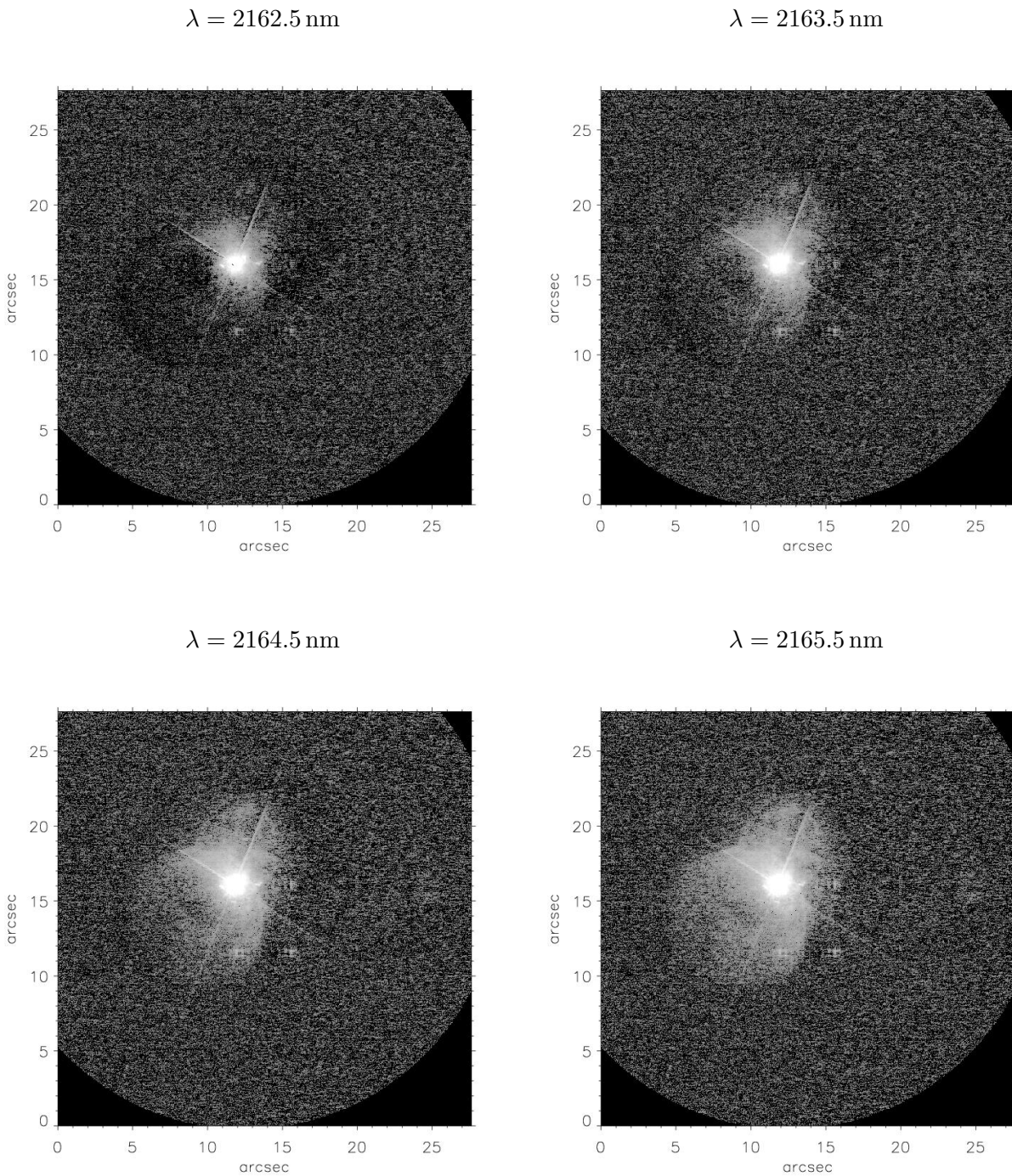


Figure 5.2: Compilation of 10 frames extracted in steps of 1 nm from the (x, y, λ) -cube. The center of the line emission in the rest frame is 2165.5 nm.

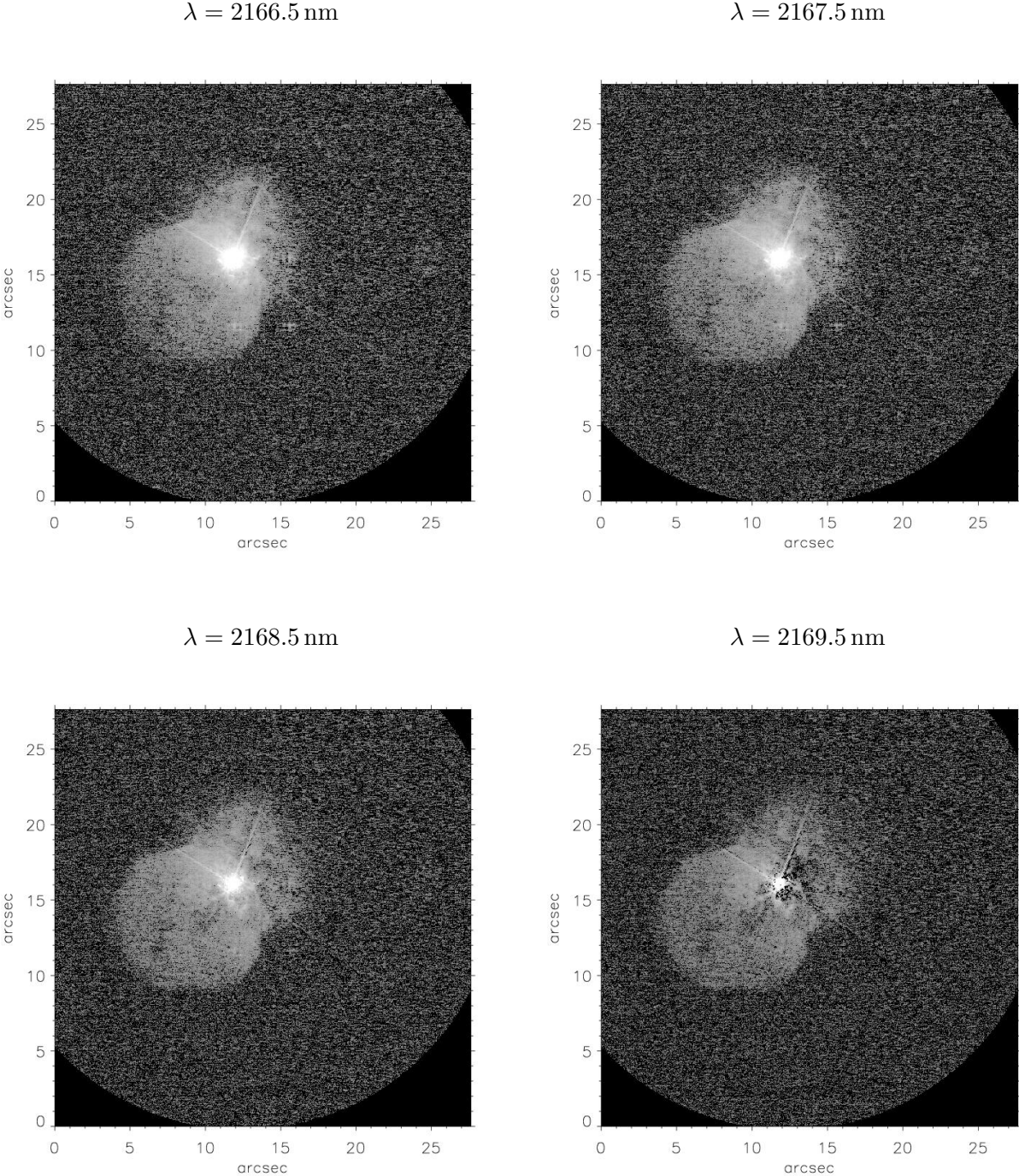


Figure 5.2: Continued.

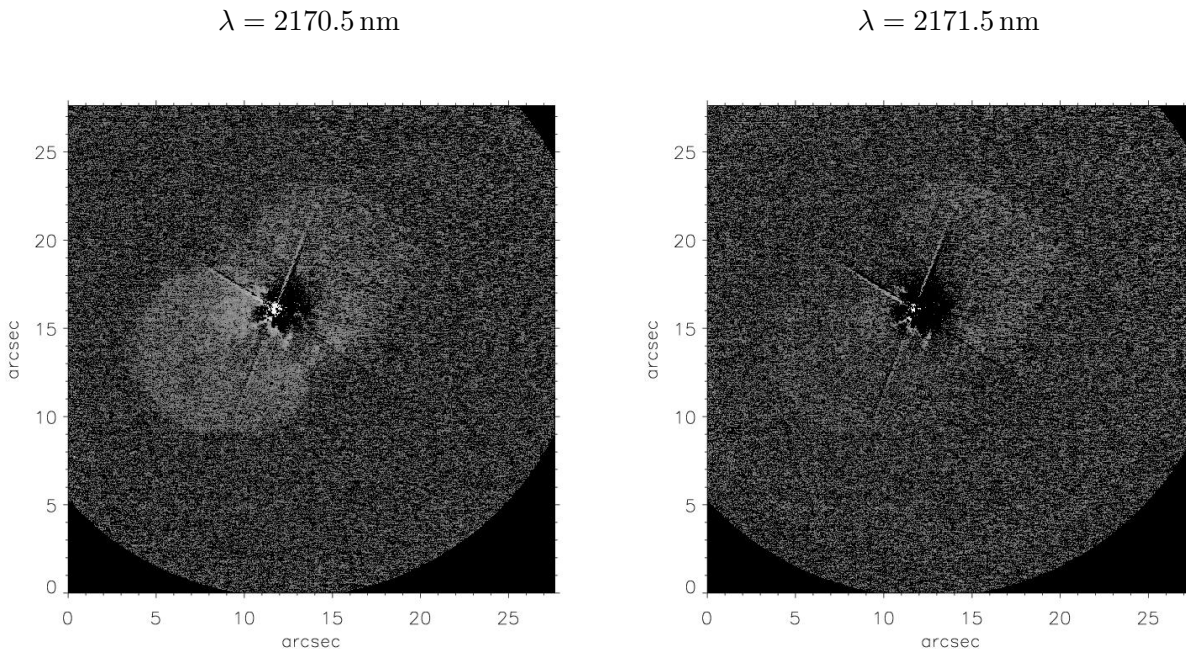


Figure 5.2: Continued.

5.2 Eta Carinae

Eta Carinae is a very well-studied Luminous Blue Variable (LBV) but still there are a lot of unsolved questions and mysteries. For an up-to-date overview the reader may refer to Davidson and Humphreys (1997); Morse et al. (1999) Gull et al. (2001).

This star is an extremely massive and highly evolved member of the Carinae star-burst region. It shows a periodicity of 5.5 years. In 1841, a giant eruption ejected several solar masses or more of material. Most of this material is currently in the dusty nebula denoted as the “Homunculus” that is the subject of our Fabry-Perot performance demonstration. The projected diameter of the Homunculus is about 17”. Each bipolar lobe’s near-UV-to-near-IR spectrum is essentially a reflection of the central star, plus some intrinsic emission lines. On the other hand, the “northwest” fan in the equatorial skirt shows a spatially-dependent forest of intrinsic emission lines with less reflection of the star. Complex ions such as Fe+, Ni+, and Cr+ are especially well represented. The HST image shown in Fig. 5.7 (see Morse et al. (1998)) may serve as illustration.

The average outflow velocity is thought to be approximately 500 km/sec, even though faster and slower streams are suspected to exist. The projected expansion of the Homunculus walls ranges from 10 to 50 mas per year. This corresponds to 1 to 3 pixels per year, when observing with CONICA’s slowest camera objective C50S.

5.3 Investigation of the 3D structure of the Homunculus

To probe the 3D structure of the Homunculus nebula, the Br γ -line is a good choice, since this line is not produced in the Homunculus itself. Hence, all light within this line coming from the Homunculus can be regarded as reflected star light.

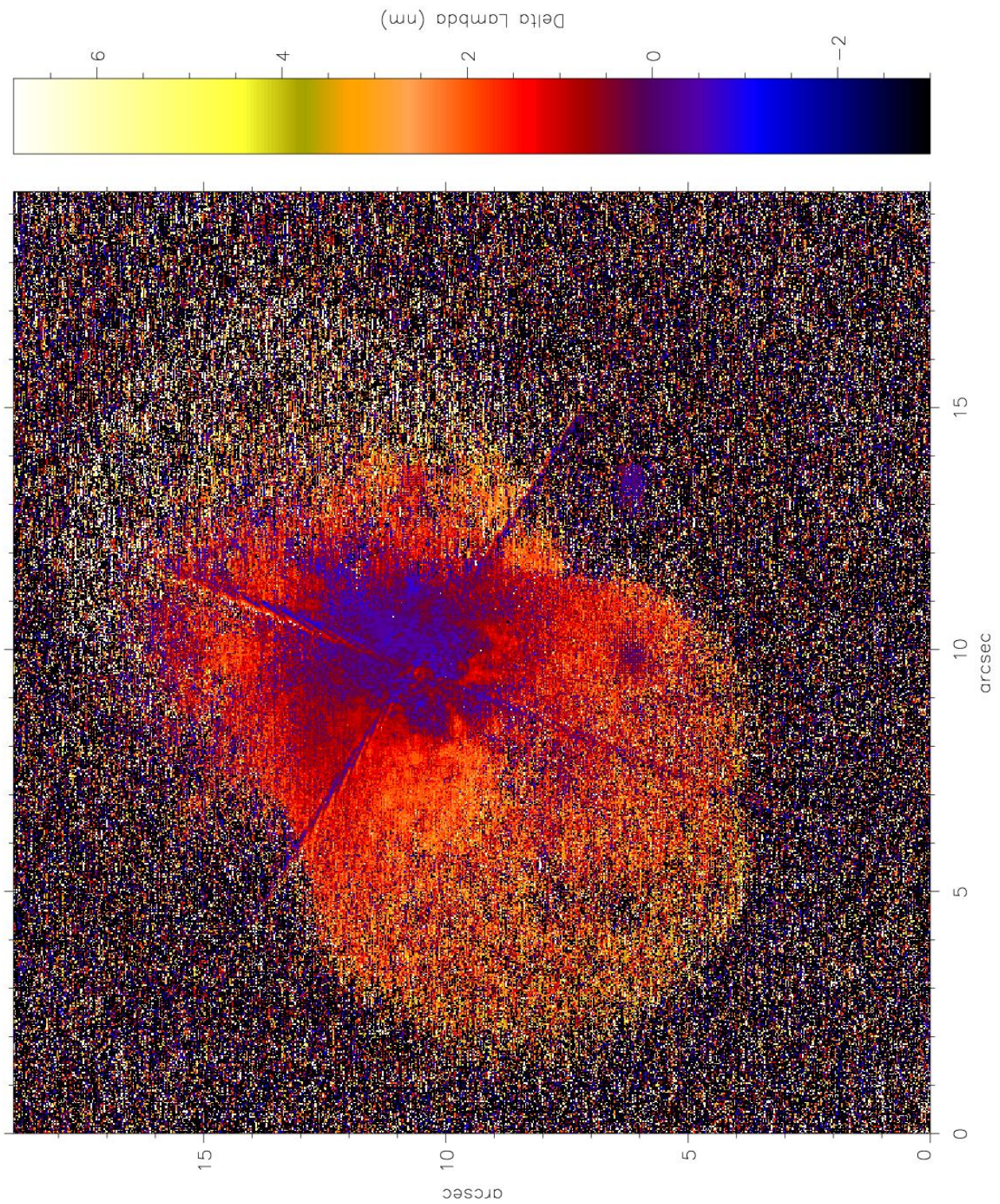


Figure 5.3: Velocity map of Eta Car displaying the wavelength range from -3 nm to $+7$ nm around the center of the $\text{Br}\gamma$ -line in the laboratory frame.

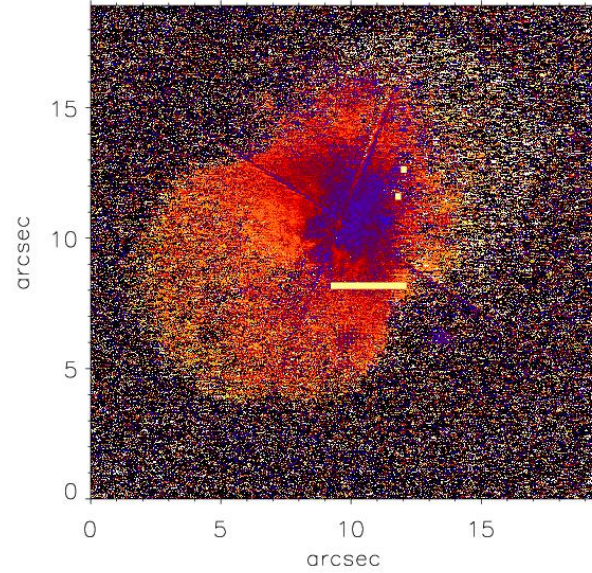


Figure 5.4: Velocity map indicating the position for the extracted spectra. The thickness of the straight line corresponds to the re-binned region to improve the S/N of the spectral cut shown in Fig. 5.5.

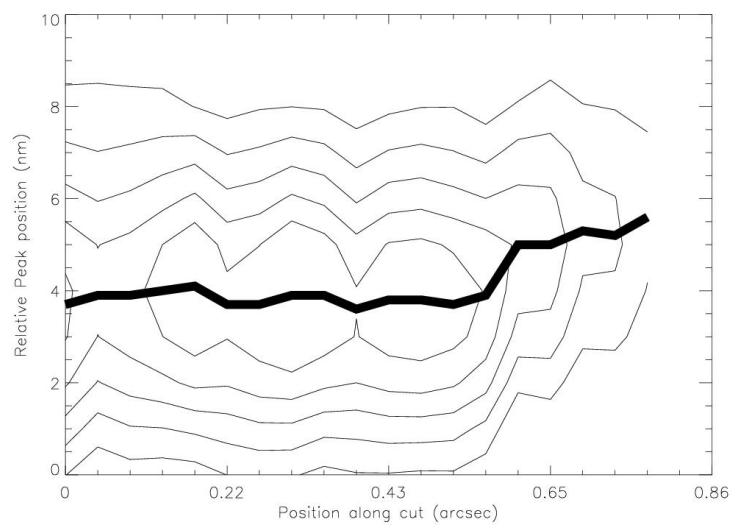


Figure 5.5: Spectra extracted from the (x, y, λ) -cube along the line indicated in Fig. 5.4.

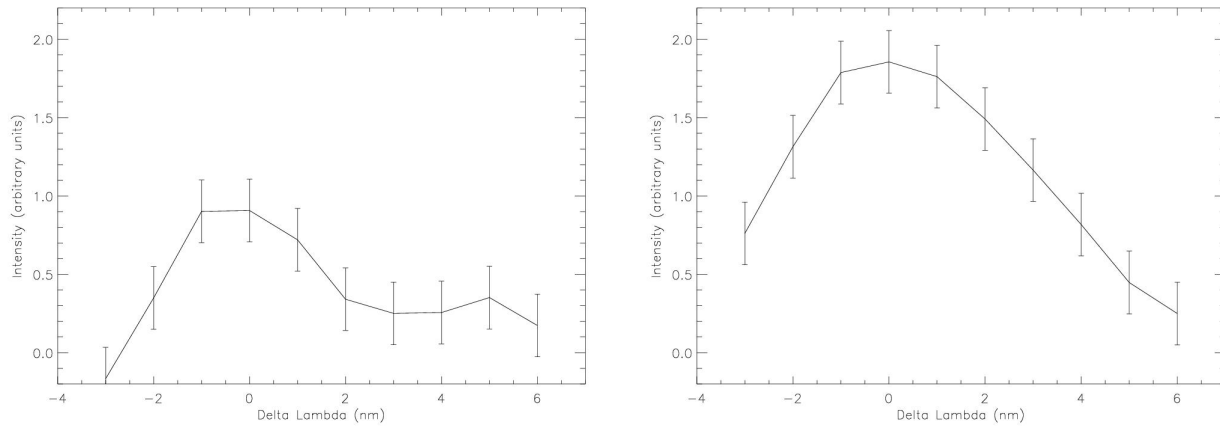


Figure 5.6: Spectra extracted from the (x, y, λ) -cube at spatial positions indicated by the filled squares in Fig. 5.4.

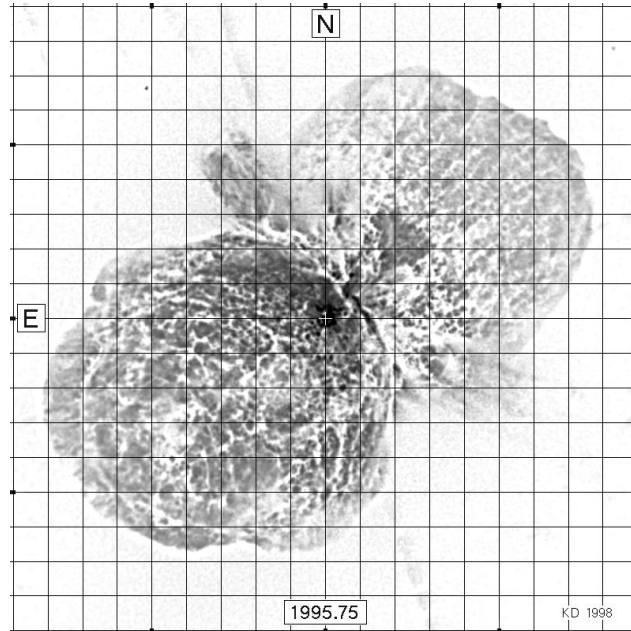


Figure 5.7: HST/WFPC2 image of Eta carinae with its Homunculus in late 1995. The grid spacing is $1''$, it is oriented NE/SW in the J2000 coordinate system. The center (marked +) coincides with the star. This image represents mainly red continuum light scattered by dust, with little contribution by intrinsic emission produced in the gas.

In Currie et al. (2000) a double flask (in contrary to spherical hollow shells) is proposed to model the 3D shape of the Homunculus. The Br γ -line emission is used to probe the structure of the walls from the flask. Assuming that the central star illuminates the walls, projected Doppler velocities are derived from the reflected line and compared with the observations. This approach seems to confirm the double flask shape of the Homunculus.

Our CONICA Fabry-Perot data are very shallow (17.2 sec total integration time per scan frame), and therefore they cannot be used to extract further details. Yet, they reveal the exciting potential for deeper data cubes. Even if the velocity map depicted in Fig. 5.3 is rather noisy, the expected velocity profile is detected. The central star shows its line emission with no significant spectral shift. Regions close to the direct line of sight are less red-shifted, than regions away from the line of sight. A jump in the velocity of about 140 km/sec between the west border of the southeast lobe and the central disk can be seen. This is emphasized by the extracted spectrum (Fig. 5.5). In Currie et al. (2000) an example is given for a possible double peak detection of the Br γ line. The peaks pertain to the reflected lines at the front and the back wall of the northeast lobe. The back wall peak is of much lower intensity because of its obscuration. The spectrum shown in Fig. 5.6 on the left is taken at a position close to the one shown in Currie et al. (2000). Even if our data are too shallow to detect the back wall peak to a significant level, for statistical reasons the little peak seems to reflect a real back wall signal, since similar spectra show up a different spatial positions in that region. Further confidence is given through the comparison with the spectrum shown in Currie et al. (2000), which shows a similar intensity ratio and a similar separation in wavelength of both peaks.

5.4 Conclusion

Taking the example of a FPI scan of the Homunculus nebula, we demonstrated the exciting scientific potential of CONICA's Fabry-Perot, in particular, given the short exposures.

For scientifically useful data, we should ensure that the spectral sampling is well above the Nyquist criterion, and to have the wavelength scan long enough to observe the range of possible Doppler shifts, and to provide frames far enough away from the line emission to construct the continuum image.

Additional interesting data sets would be cubes, on the one hand, without the central source being saturated to allow a derivation of the relative photometric relation between light emitted from the central source and the light reflected from the walls of the nebula. On the other hand, deep data in combination with CONICA's coronagraphic mode would permit fascinating insights in the 3-dimensional structure of the Homunculus.

Certainly, this high resolution imaging spectroscopy together with adaptive optics at an 8-m class telescope will open a new realm of possibilities in exploring our universe.

Chapter 6

Gallery

Pictures may tell more than thousands words, hence the final chapter intends to give an impression about some moments within the course of the project via a picture gallery. Certainly, the selection of images for the first section showing CONICA and NAOS on their way to First Light is very restricted and subjective, but represent definitely corner stones in the project or moments of high (personal) relevance. The pictures in Sect. 6.1 pick out some of these moments from CONICA and NAOS on their way to First Light.

A kaleidoscope of technical and scientific results presented in Sect. 6.2 is intended to light up the exciting research potential of the new VLT instrument. All examples are taken from data obtained during Commissioning and Science Verification before the instrument was offered to the astronomical community in October 2002.

6.1 The way to First Light

Figure 6.1 Spring 2000. Experimental setup for the throughput measurement in the Montagehalle (not renovated yet) of the MPIA in Heidelberg. This measurement is described in Sect. 3.4. CONICA is detached from the adapter flange to get close access to its entrance window. The emitting surface of the tunable blackbody source is positioned directly in front of the entrance window. The IRACE readout electronics that usually is mounted piggy-back at the adapter flange is pending over the cryostat. Its connection cables must kept short for a high frame rate.

Figure 6.2 Autumn 2000. Armin Böhm prepares CONICA for its transport to Paris and fixes the cryostat into its maintenance carriage.

Figure 6.3 Autumn 2000. In a foggy morning the lorry was loaded with the boxes containing CONICA, the adapter flange, mounting equipment, electronic racks, workstations, tools and spares. From the left: J. Pihale, F. Witzel and the driver Achmed.

Figure 6.4 Autumn 2000. View from the Observatory Paris-Meudon over Paris. For the lack of space at the observatory, the integration hall was sourced out to the CNRS terrain in Bellevue, approximately 1 km away from the Observatory.

Figure 6.5 Spring 2001. Having resolved technical problems mainly concerning the infrared wavefront sensor and field selector during wintertime, the double marriage of NAOS and CONICA (top) and the author with his bride (bottom) could take place with hard constraints for the honeymoon.

Figure 6.6 Summer 2001. Preliminary Acceptance Europe. Arno van Kesteren (ESO) performs together with Karl Wagner (MPIA) electro-magnetic compliance tests. In steps, all electronic devices of NAOS-CONICA were shut down to measure the electro-magnetic radiation over a wide band of frequencies. In the front a vertical directed dipole-antenna is set up.

Figure 6.7 Summer 2001. Preliminary Acceptance Europe. To determine the total weight, NAOS is separated from the VLT Nasmyth simulator and the adapter flange. The weight for the platforms of the VLT Nasmyth focii is limited to 3 tons. NAOS' weight was determined to approximately 2.2 tons; together with CONICA the combined instrument exceeded slightly the limit. This action item was solved during commissioning and the instrument was lightened.

Figure 6.8 Autumn 2001. NAOS-CONICA was shipped via air-fright from Paris to Santiago de Chile and then overland to Cerro Paranal in the Atacama desert. The CONICA boxes are lined up in front of the Paranal assembly hall at the base camp.

Figure 6.9 November 2001. NAOS in the state of re-integration in the Paranal assembly hall.

Figure 6.10 November 2001. On a low-loading truck the instrument is transported to the top of Cerro Paranal. A tarred road leads from the base camp to the summit. Three of the four VLT telescopes are visible from the distance. The telescope unit to the left is UT4, called Yepun, into which NAOS-CONICA is going to be installed.

Figure 6.11 November 2001. NAOS-CONICA mounted to the Nasmyth-B focus of UT4. The telescope is tilted and the primary mirror is seen.

Figure 6.12 December 2001. F. Laombe, W. Brandner and G. Zins at the UT4 console in the VLT control room. After first light the AO performance was tested.

Figure 6.13 December 2001. NAOS (blue) mounted to the Nasmyth adapter. CONICA (red) is attached via the adapter flange to NAOS.

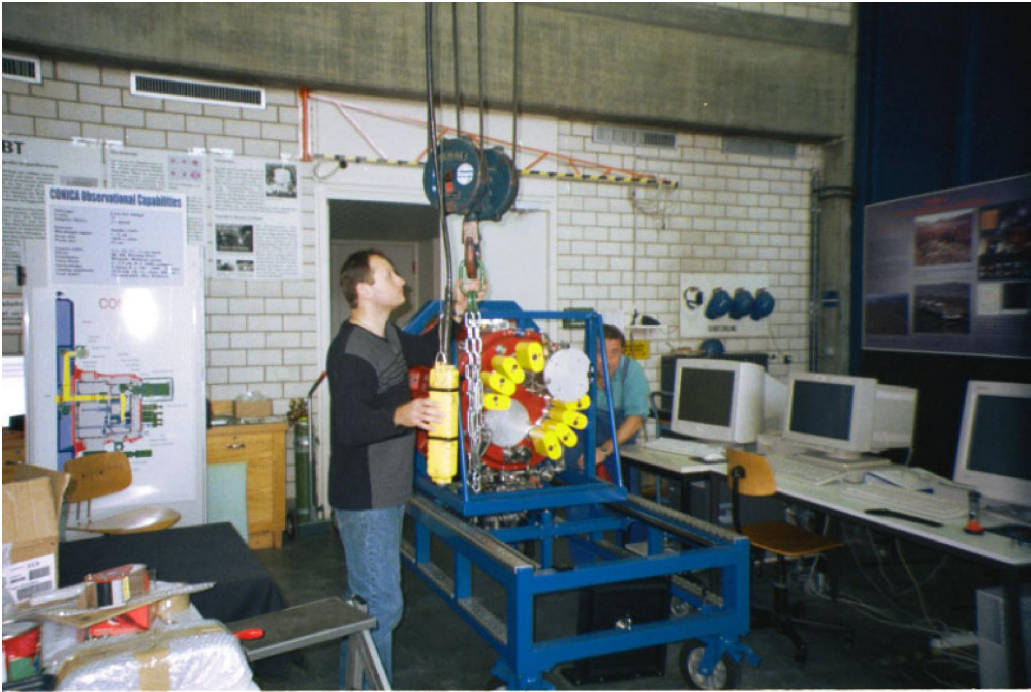
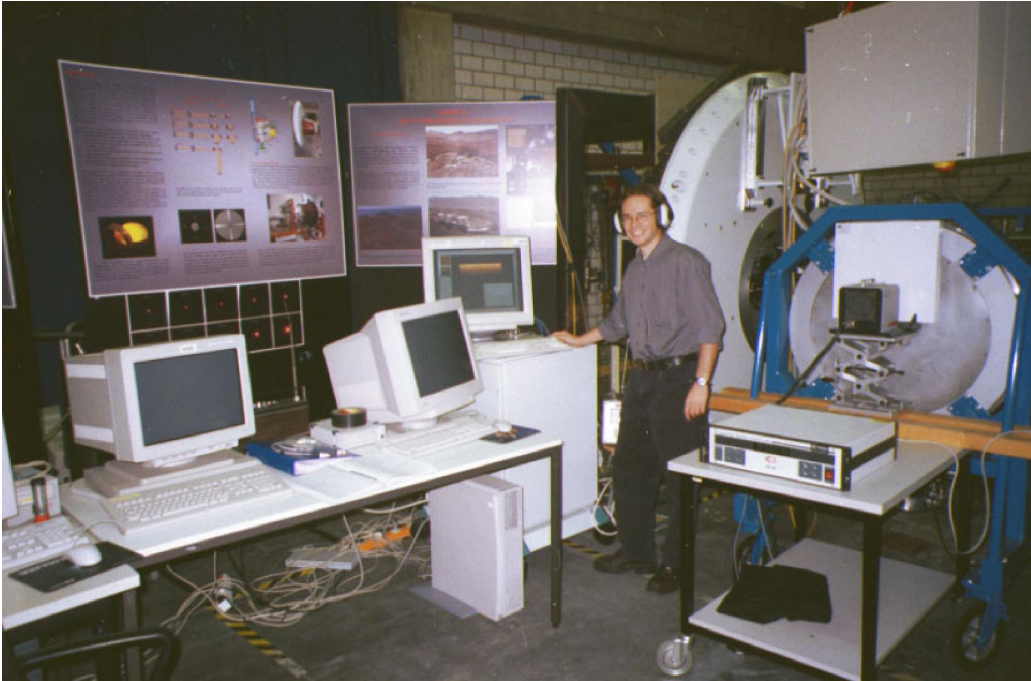


Figure 6.1: Throughput measurement.

Figure 6.2: A. Böhm is fixing CONICA into its maintenance carriage.



Figure 6.3: Loading of the lorry with CONICA boxes.

Figure 6.4: View from the Observatory Paris-Meudon over Paris.

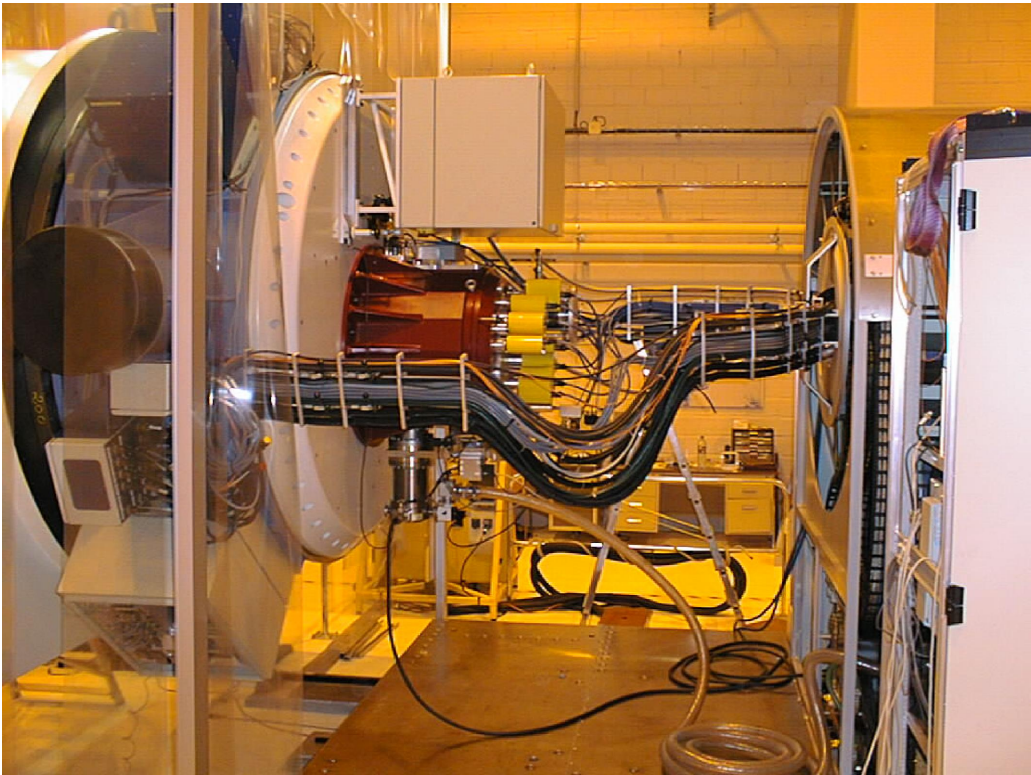


Figure 6.5: Double-marriage: NAOS & CONICA and the author with his bride.

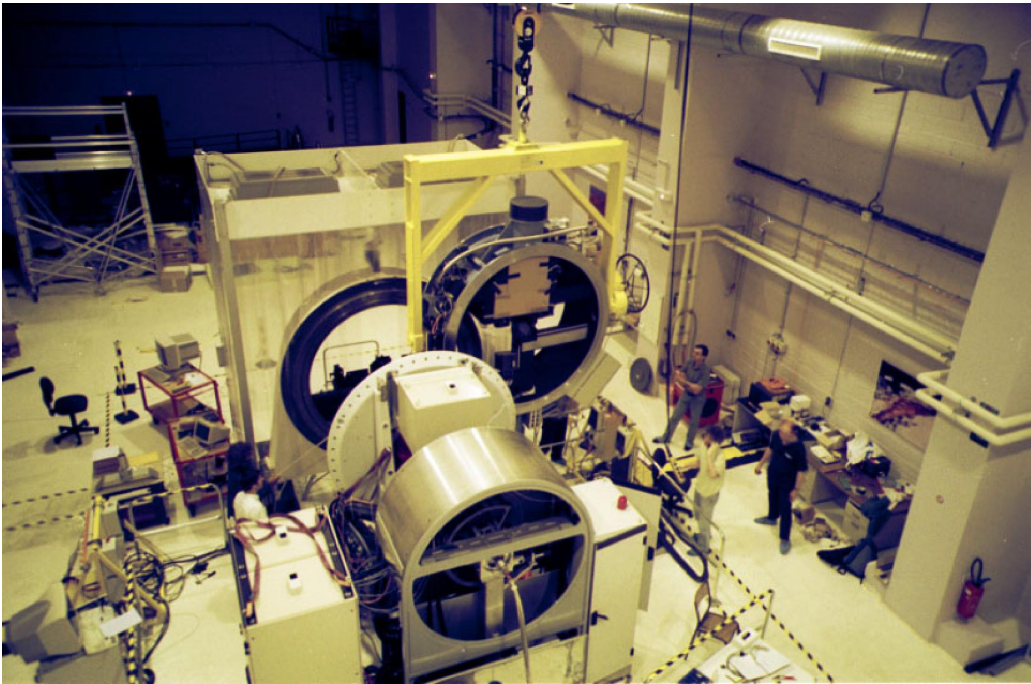


Figure 6.6: Electromagnetic compliance tests.

Figure 6.7: Weighing of NAOS.

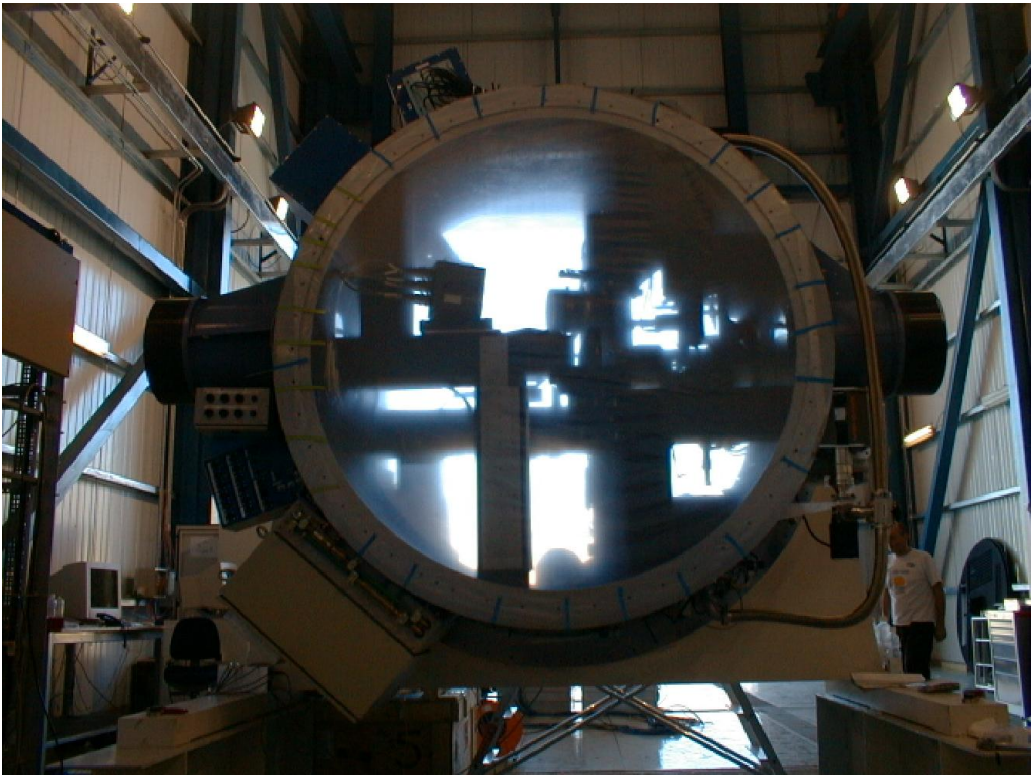


Figure 6.8: Arrival at Paranal. CONICA boxes in front of Assembly and Integration hall.

Figure 6.9: Re-integration of NAOS.

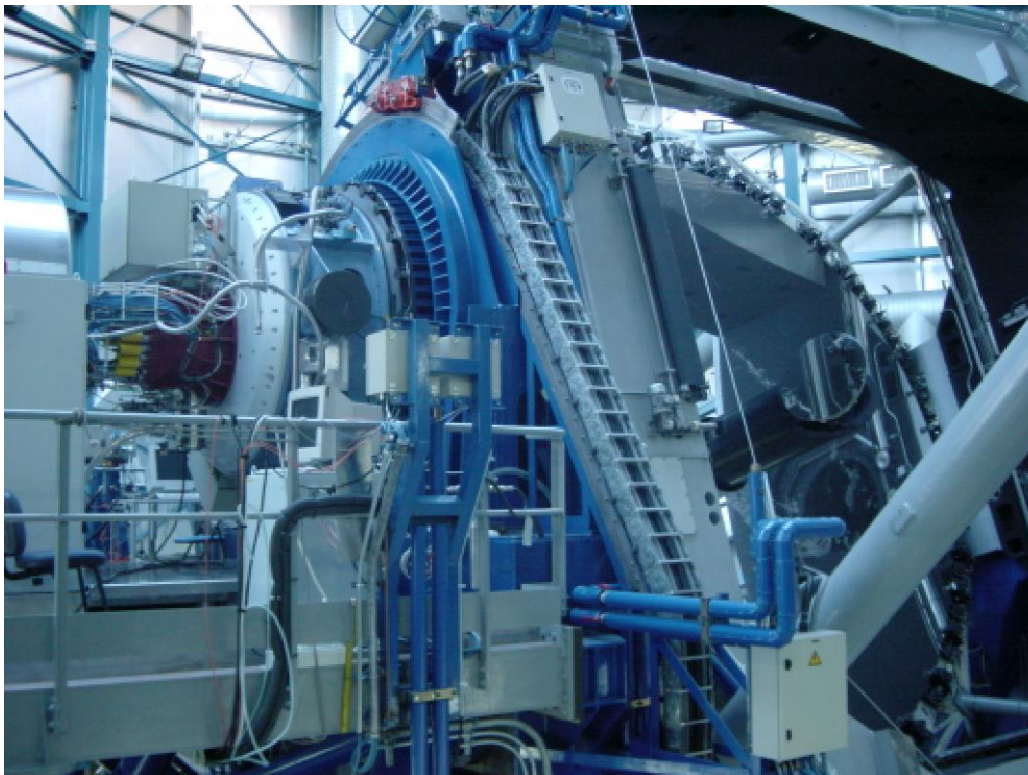


Figure 6.10: Transport of the instrument to the summit of Cerro Paranal.

Figure 6.11: NAOS-CONICA mounted to the Nasmyth focus.



Figure 6.12: UT4 console in the VLT control room.

Figure 6.13: NAOS-CONICA flanged to the Nasmyth-focus.

6.2 Highlights during Commissioning and Science Verification

Io

Figure 6.14. *December 2001. Commissioning.* Certainly, AO systems prefer their reference objects to be point like. But if the reference object is bright, the AO loop can be close on extended objects with a diameter in the order of 1 arcsec. This ability is proofed at the Jovian moon Io. The picture is a composite of Br γ - and L'-band observations. Despite the small angular diameter of Io, many features are visible with the high-angular resolution camera CONICA. A latitude-longitude grid is superposed, with the most prominent features identified by name, including some of the large volcanoes and sulphurus plains. The richness of details can be further improved by the application of myopic¹ deconvolution techniques (Fusco et al. 2003).

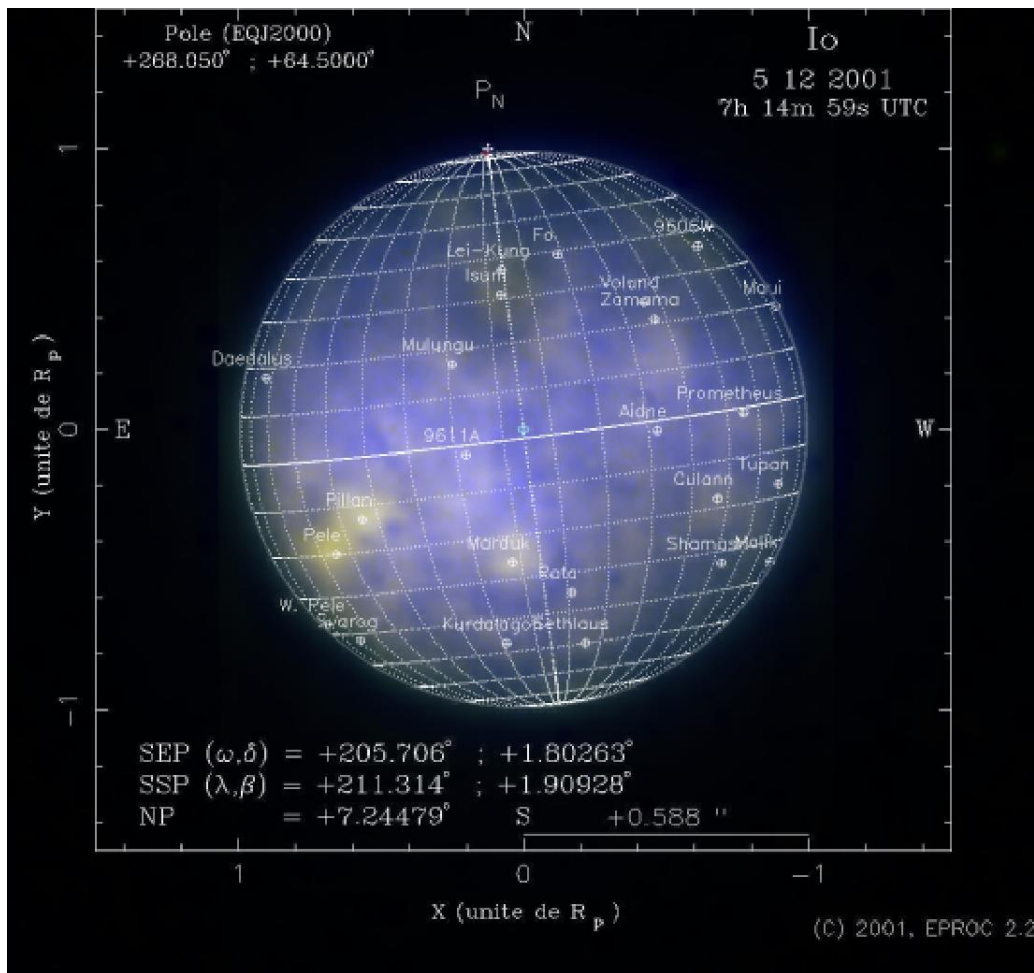


Figure 6.14: K- and L-Band composite of Io.

¹Joint estimation of object and PSF.

Saturn

Figure 6.15. *December 2001. Commissioning.* In the case that the AO reference object is moving relative to the science object, the AO system is able to adapt for this by the differential tracking mode of the field selector. A demonstration of this mode is given with the aid of the Saturnian moon Tethys serving as AO reference object. To keep Saturn fixed on the CONICA detector, the differential motion of Tethys is compensated via a pre-calculated tracking table valid for the observing time. With the tracking table the field selector directs the reference object in exactly that manner over the wavefront sensor that the AO tip-tilt mirror will counter steer resulting in a fixed position of Saturn but in a trailed image of the reference object (Lacombe et al. 2003). The picture of Saturn is a composite of J-, H- and K-band frames. Tethys can be identified as tiny spot under Saturn. The FOV is 55 arcsec.

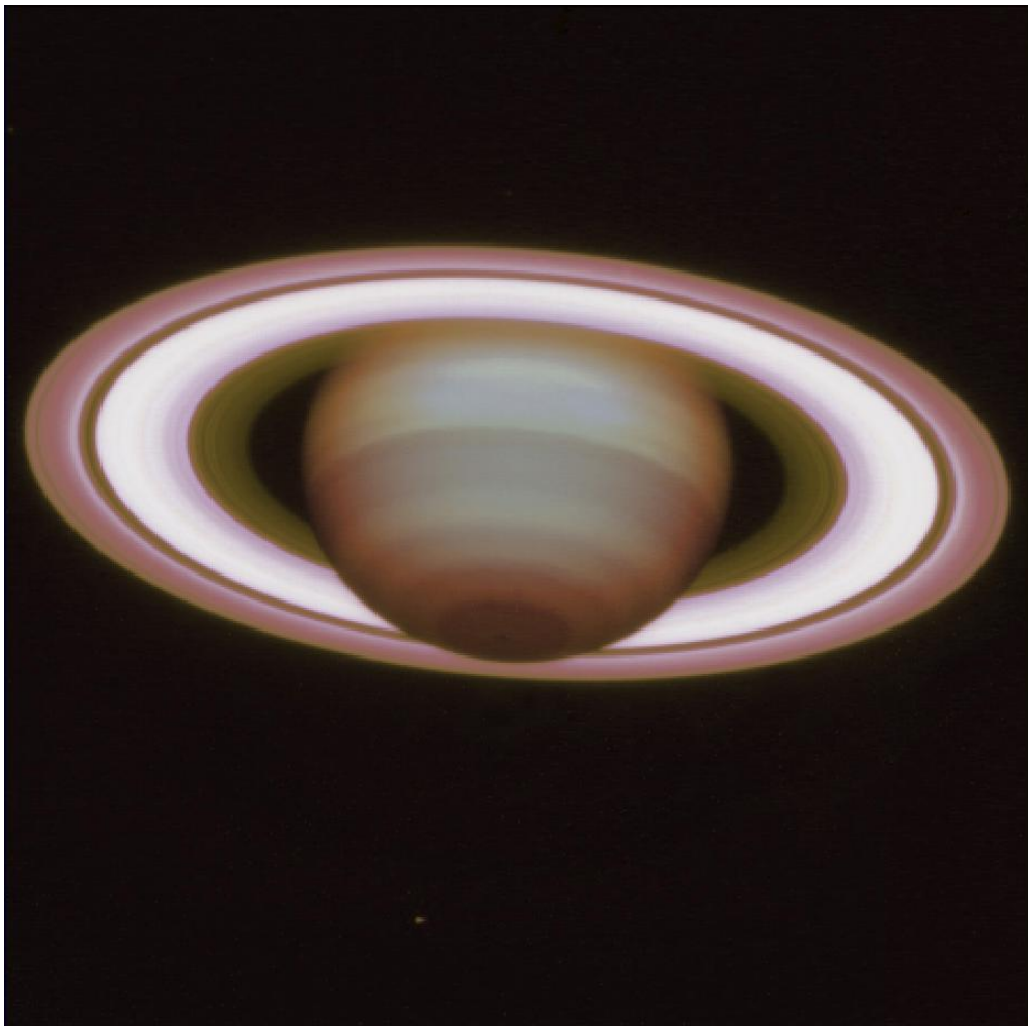


Figure 6.15: Composite of Saturn in JHK.

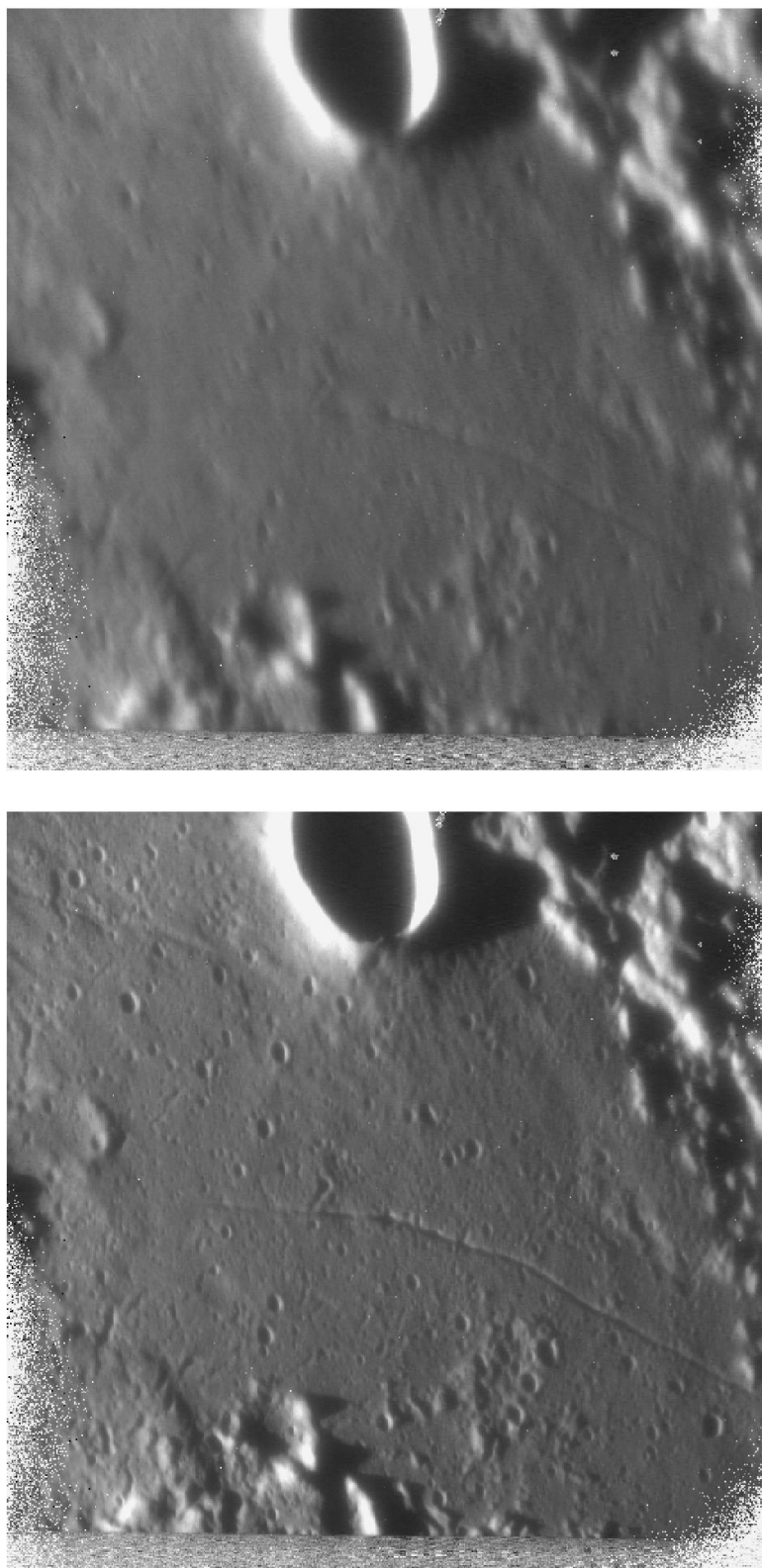


Figure 6.16: The moon surface with and without adaptive optics.

The moon

Figure 6.16. *April 2002. Commissioning.* An astonishing demonstration of NAOS' ability to close the loop at resolved sources was done at the moon. Here, the visible WFS uses a bright rim of a crater to control the loop. The picture on the top is without AO correction, on the bottom with AO correction. For the extreme brightness of the moon the images are taken with very short exposure times (0.22sec) with a narrow band filter in K-band. The pixel scale amounts to 27 mas/pix. The depicted frames are only flat-fielded.²

The Galactic center

For two decades, evidence has been mounting that the Galactic center harbours a concentration of dark mass associated with the compact radio source SgrA* located at the center of the nuclear star cluster. This radio source in the center of our Milky Way thus may be a supermassive black hole. Even if it is commonly believed by now, that black holes in the center of galaxies are not exceptionally, there are still alternative physical models (ball of heavy fermions, ball of mini-bosons) that seem improbable but are not totally ruled out. Because of its proximity, the Galactic center of the Milky way is unique to allow for a study of the physical processes that might occur generally in galactic nuclei.

The MPE in Garching, CO-PI-institute³ of CONICA investigates since a decade proper motions in the Galactic center and traces carefully trajectories of the closest stars to SgrA*. With the capabilities of the NAOS IR WFS it is possible to observe the region with unprecedented spatial resolution. Even if it was already known from earlier observation that a star denoted S2 would pass SgrA* in close proximity, its observation during commissioning turned out to a big surprise because S2 was detected in its peri-center almost on SgrA*. The separation was found to be 30 mas, less than than the FWHM of the diffraction limit.

This lucky coincidence made it possible to determine the orbital parameters with a surprising good precision and the period of S2 was found to be approximately 16 years. With the aid of this orbit the mass of the supermassive black hole is determined to $2.9 \cdot 10^6$ sun masses and the evidence for the dark matter concentration to be a black hole strongly reinforced (Schödel et al. 2002; Ott et al. 2003).

Figure 6.17. *May 2002. Commissioning.* Left: K_s-band image of the central 40 arcsec of the Milky Way. North is up and East to the left, the angular linear scale for a distance of 8 kpc are marked at the bottom. The total integration time was 20 min with the final image resulting as a sum of 60 images with 20 sec each. The pixel scale is 27 mas/pix. The bright supergiant IRS7 served as guide star for the IR WFS to close the loop. The achieved SR exceeds 50%. The IRS16 and IRS13 complexes of bright HeI emission line/early type stars are marked. Right: The central 2 arcsec region (rectangle in the left figure) around the compact radio source SgrA*. This image is deconvolved with a linear Wiener filter method to remove the seeing halos. The ring structures around the brighter stars are artifacts of the linear deconvolution algorithm that arise because information on the PSF in Fourier space is not know up to infinite frequencies.

Figure 6.18. *March to September 2001. Commissioning and Science Verification.* Orbit of S2, relative to the position of SgrA* (large cross and circle, denoting the ± 10 mas uncertainty of the

²Dead and hot pixels not removed. The stripe at the bottom is the edge of the field limiting mask.

³According to the ESO contract, the Max-Planck-Institut für extraterrestrische Physik (Garching) was in charge of the detector and its readout electronics. Reiner Hofmann signed as Co-Primary Investigator. The guaranteed observing time between MPE and MPIA.

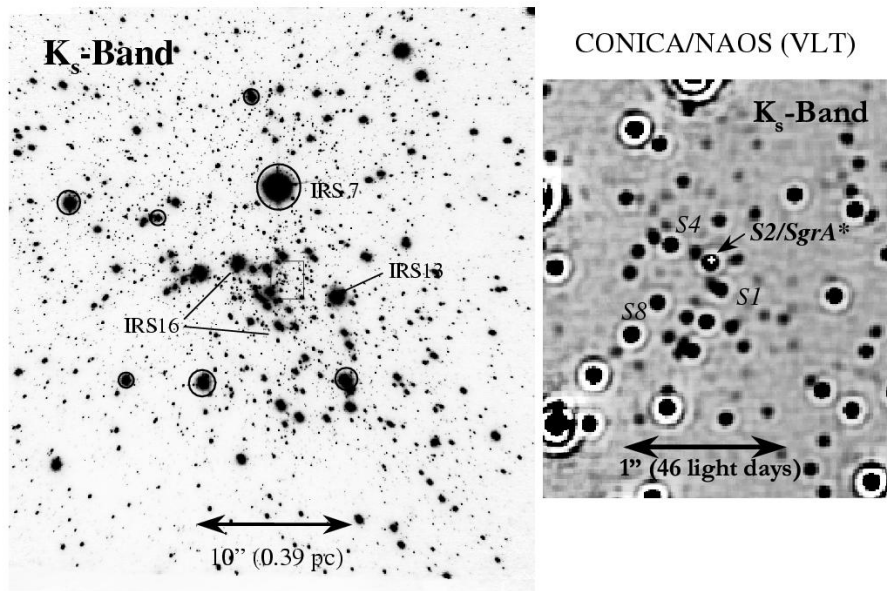


Figure 6.17: The Galactic center in the near-infrared (Ks-Band).

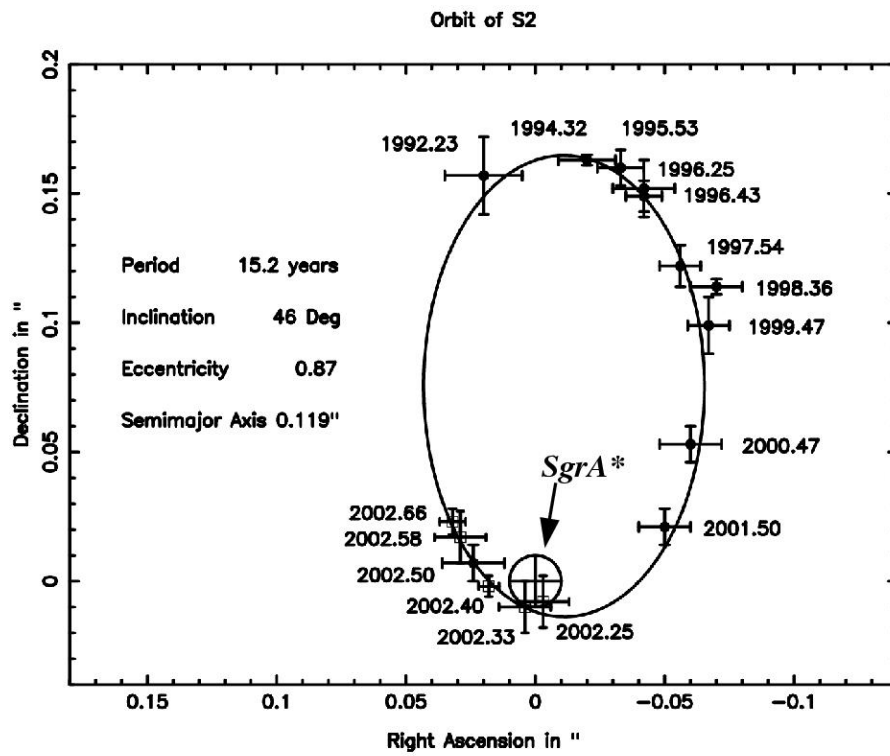


Figure 6.18: The orbit of S2.

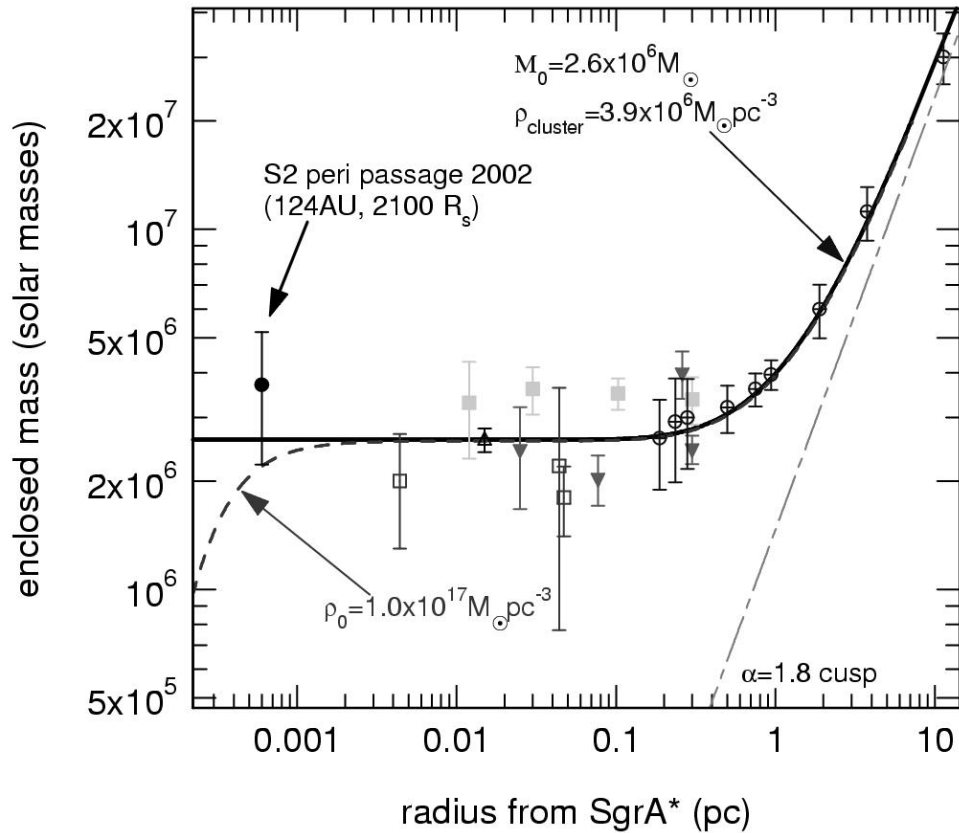


Figure 6.19: Mass distribution in the galactic center.

infrared-radio astrometry). The filled small circles (with 1σ errors) between 1992 and 2001, and at 2002.40, denote the results of speckle imaging with the SHARP camera at the ESO NTT. The three open rectangles are the NAOS-CONICA data points taken during the Commissioning and Science Verification period. The projection of the best fitting Kepler orbit is shown as a thick continuous curve, with their main parameters listed adjacent to the orbit.

Figure 6.18. *March to September 2001. Commissioning and Science Verification.* Mass distribution in the Galactic center. The filled circle denotes the mass derived from the orbit of S2, with the error bar coming from the combination of the statistical fit error for the nominal SgrA* position, and the error stemming from the uncertainty in the infrared-SgrA* astrometry. Filled rectangles are Leonard-Merritt projected mass estimates from a new proper motion data set by Ott et al. (manuscript in preparation). Crossed rectangles and open circles are mass estimates from the Jeans models Genzel et al. (2000). The continuous curve is a best fit model and results from the sum of a $2.9 \cdot 10^6 M_\odot$ point mass, plus a stellar cluster of central density of $3.5 \cdot 10^6 M_\odot$, core radius 0.34 pc and power-law index $\alpha = 1.8$ (plotted as a long-dash-short-dash curve.) The thick dashed curve is a sum of the same cluster, plus a Plummer model of a hypothetical concentrated ($\alpha = 5$), very compact ($R_0 = 0.00037$ pc) dark cluster of central density $1.4 \cdot 10^{16} M_\odot \text{pc}^{-3}$.

Chapter 7

Summary and Conclusions

This PhD thesis work led to a number of important contributions to the successful commissioning of the near-infrared camera CONICA, operating with its adaptive optics system NAOS at the Very Large Telescope in Chile.

During the test and laboratory period of CONICA in Heidelberg, the replacement of the preliminary Hawaii-Chip with the Aladdin chip revealed that the instrumental thermal background exceeded by far the specification (< 1 electron/sec). First background measurements yielded a detector “dark current” ten thousand times higher than specified, threatening the scientific viability of CONICA. With great effort, the multiple origins for this elevated background were tracked down, in order to avoid the “emergency solution”, i.e., forsaking all use of CONICA beyond $2.5\ \mu\text{m}$. This would have significantly reduced the overall performance of CONICA due to the loss of the L and M band observing capabilities and suboptimal PSF sampling.¹ In the context of this thesis, a number of diagnostic measurements were performed that confirmed the need to replace the stainless steel axles with carbon fiber, and the need for the improvement of the baffles of the closed-cycle cooler and the focus drive. According to my proposed design modifications, the thermal background shielding was modified. In particular, a sophisticated encapsulation of the detector fanout board suppressed the residual thermal radiation. Finally, the specification was reached, ensuring the high sensitivity of CONICA’s spectroscopic modes in the near infrared, as well as the retention of the thermal infrared bands L and M.

During the integration of CONICA and NAOS in Bellevue near Paris, a collaboration between the MPIA and ONERA was established to develop a method to calibrate the static aberrations. In cooperation with Amandine Blanc and Thierry Fusco², who brought in their expertise on the estimate of static wavefront aberrations, I developed a phase diversity wavefront sensor for the imaging path of NAOS-CONICA. After providing the necessary optical setup and having iterated by a number of phase diversity measurements and experimental modifications, it turned out that a principal difficulty was the requirement of extreme precision in the alignment of the optical path, to ensure Strehl ratios $> 90\%$ in the K-band.³ Therefore, a minimal error in pupil alignment or focus adjustment will already dominate the wavefront error. Disregarding the calibration of the higher order aberrations, it turned out that even for the adjustment of the residual foci from the different optics (i.e., camera objectives and filters), phase diversity sensing had to be applied to achieve excellent compensation performance.

¹CONICA optics were designed for the Aladdin pixel size.

²A. Blanc and T. Fusco are affiliated with ONERA.

³Without atmospheric turbulence.

The instrument software architecture was expanded following my proposed conception. The sensed wavefront errors determined in the calibration measurements are administered by a database. This allows the instrument control software to automatically update the deformable mirror to compensate the wavefront errors for the actual instrument configuration. These processes are invisible to the instrument user.

Apart from providing the utmost performance for adaptive optics systems, the implementation of this wavefront sensor allows for monitoring the optical quality and to alert for any degradation. E.g., phase diversity wavefront sensing signaled a sudden contamination of the collimator during the commissioning periods. The analysis of this incident without phase diversity would have been by far more complicated and time consuming.

To facilitate the implementation of this technique for other high-performance AO systems, this thesis presents a detailed guideline through the error budget regarding instrumental and algorithmic constraints.

The full implementation⁴ of the technique to calibrate for static wavefront aberrations was accomplished during commissioning and I obtained the first AO-compensated images proving the excellent achieved performance. NAOS-CONICA is probably the first (astronomical) instrument with a complete implementation of static aberration compensation. There is no doubt that for future high performance AO systems, this technique or a similar approach will play a major role in achieving the challenging science goals of the astronomical community.

In addition, I participated in the on-sky performance evaluation of the instrument, with particular attention to the cold, tunable Fabry-Perot interferometer of CONICA. This rather unique device permits low-noise, high-spatial resolution imaging spectroscopy. Having solved technical difficulties⁵ in running the Fabry-Perot interferometer during the laboratory test period in Heidelberg as well as during integration in Bellevue, technical reliability could be achieved and proved during the commissioning period. Using guaranteed observing time data, I generated a first high-spatial resolution velocity map of Eta Carinae. To avoid an impact for high-resolution AO analysis on *deep* exposures, special care must be taken on the AO nature of the data with an appropriate observing strategy regarding the science goals. For a scan with long integration times, the PSF might significantly vary in time and thus vary along the wavelength channel. For the FPI data presented in this thesis, the assumption of a constant PSF was justified by the rapid scan.⁶ In spite of the short exposure times, the exciting capabilities for 3-dimensional structure analysis have been demonstrated. Certainly, this high-resolution imaging spectroscopy together with adaptive optics at an 8-m class telescope will open a new realm in exploring the universe.

This thesis work has been a pivotal contribution to making CONICA the sharpest, most versatile infrared camera in the world.

⁴For the final calibrations an optimized Zernike-tool was manufactured and implemented into CONICA.

⁵This concerned the cryogenic alignment and the adjustment of the capacity bridge.

⁶In addition, the data are too shallow to detect such AO artifacts.

Appendix A

Argon calibration lines

Table A.1: Prominent Argon lines in the bands J, H and K. Note that the refraction index of air depends on wavelength. For the J-band, all lines with $S/N > 4.8$, for H and K all lines with $S/N > 4.0$ are compiled. The S/N -values help identify the line via their relative intensities. The lines are extracted from Whaling et al. (2002).

Band	Wavelength in vacuum (nm)	Wavelength in standard air (nm)	Intensity $\log(S/N)$
J	1244.2725	1243.9321	4.85
	1249.1080	1248.7663	4.88
	1296.0201	1295.6659	4.94
	1327.6265	1327.2635	5.18
	1331.6849	1331.3209	5.02
	1337.0767	1336.7110	5.23
	1350.7882	1350.4189	5.34
	1362.6383	1362.2658	5.07
	1372.2327	1371.8575	5.47
H	1505.0621	1504.6505	4.82
	1517.6837	1517.2691	4.27
	1530.6061	1530.1878	4.32
	1599.3860	1598.9492	4.30
	1644.1062	1643.6572	4.02
	1652.4376	1651.9864	4.19
	1694.5210	1694.0584	5.09
	1791.9615	1791.4723	4.46
K	2062.1854	2061.6226	4.64
	2099.1836	2098.6108	4.41
	2154.0080	2153.4203	4.19
	2208.3204	2207.7179	4.26
	2313.9514	2313.3201	4.28
	2385.1536	2384.5030	4.81

Appendix B

Phase diversities and oversampling

Table B.1: Peak-to-peak phase diversities in radian corresponding to axial pinhole distances and the factor of oversampling for an f/15 beam. The values are compiled for all CONICA narrow band filters.

Filter	$\lambda_c(\mu\text{m})$	1 mm	2 mm	4 mm	C25S/C25L	C50S
Oversampling						
NB1.040	1.040	1.07π	2.14π	4.27π	0.50	1.00
HeI	1.083	1.03π	2.05π	4.10π	0.51	1.04
P γ	1.094	1.02π	2.03π	4.06π	0.52	1.05
OII	1.237	0.90π	1.80π	3.59π	0.59	1.19
FeII 1.257um	1.257	0.88π	1.77π	3.54π	0.60	1.21
P β	1.282	0.87π	1.73π	3.47π	0.61	1.23
FeII 1.644um	1.644	0.68π	1.35π	2.70π	0.78	1.58
H2(1-0)S(7)	1.748	0.64π	1.27π	2.54π	0.83	1.68
NB2.00	2.000	0.56π	1.11π	2.22π	0.95	1.92
NB2.03	2.030	0.55π	1.09π	2.19π	0.97	1.95
NB2.06	2.060	0.54π	1.08π	2.16π	0.98	1.89
NB2.09	2.090	0.53π	1.06π	2.13π	0.99	2.01
NB2.12	2.120	0.52π	1.05π	2.10π	1.01	2.04
H2(1-0)S(1)	2.122	0.52π	1.05π	2.09π	1.01	2.04
NB2.15	2.150	0.52π	1.03π	2.07π	1.02	2.07
Br γ	2.166	0.51π	1.03π	2.05π	1.03	2.08
NB2.18	2.180	0.51π	1.02π	2.04π	1.04	2.10
NB2.21	2.210	0.50π	1.01π	2.01π	1.05	2.13
NB2.24	2.240	0.50π	0.99π	1.98π	1.07	2.15
NB2.27	2.270	0.49π	0.98π	1.96π	1.08	2.18
NB2.30	2.300	0.48π	0.97π	1.93π	1.09	2.21
NB2.33	2.330	0.48π	0.95π	1.91π	1.11	2.24
NB2.36	2.360	0.47π	0.94π	1.88π	1.12	2.27
NB2.39	2.390	0.46π	0.93π	1.86π	1.14	2.30
NB2.42	2.420	0.46π	0.92π	1.84π	1.15	2.33
NB2.45	2.450	0.45π	0.91π	1.81π	1.17	2.36
NB2.48	2.480	0.45π	0.90π	1.79π	1.18	2.39
Pf γ	3.740	0.30π	0.59π	1.19π	1.18	3.60
Br α	4.051	0.27π	0.55π	1.10π	1.93	3.89

Appendix C

Calculation of Strehl Ratios

C.1 SR via image space

A common way to describe the achieved image quality is the ‘Definitionsshelligkeit’, introduced by Strehl (1902). Meanwhile, the term ‘Strehl ratio’ (SR) is employed. It is defined by the ratio of the measured and the theoretical diffraction-limited peak intensity. The common approach to derive this value from the image is to construct a theoretical diffraction-limited PSF with the adequate pixel sampling and then to compare the pixel values at peak position after having normalized the total flux. The calculation of the theoretical diffraction-limited PSF can be done straight-forward as long as the input parameters like wavelength, pixel scale, aperture, and central obscuration are known. Yet, the normalization of the experimental data is often problematic, since it is hard to determine the accurate value of the total intensity. Certainly, the raw image data must be flat-fielded and background corrected, but even then the data are usually afflicted by residual background features. These features strongly affect the precision of normalization and thus the precision of the calculated SR. We illustrate this by a calibration image of the $10\ \mu\text{m}$ in-focus pinhole in the entrance focal plane of CONICA. The wavelength is selected by the Br γ -filter and objective C50S is used. The corresponding image is shown in Fig. C.1. In this example, we have chosen a PSF with very little degradation. The log-scale image reveals several diffraction rings and we expect a SR above 90%. Calculating the SR as described above disregarding the influence of the residual background yields a SR of 73% (see Tab. C.1). A good way to investigate the residual background is to trace the intensity with concentric rings around the PSF. This is illustrated in Fig. C.2. The evolution of the total number of counts within a concentric ring of radius r and a thickness d of 5 pixel (66 mas) is plotted. The rings for small radii still count a significant amount of intensity from the trailing edge of the PSF, but far enough from the center they measure the residual background. The affect of the theoretically expected PSF is shown by the long-dashed line. The short-dashed line marks the mean level referring to the region of radii $30\ \text{pixel} < r < 60\ \text{pixel}$. The 1σ deviation gives an upper and lower limit for the error. This error can be quite large, in particular for PSFs under atmospheric turbulence or at frames with bad background correction or bad noise characteristics (e.g., pickup noise). Our example definitely belongs to the best cases, in general the given errors might be significantly larger. The correction for the residual background (0.4 ADU/pixel) lifts the SR to a reasonable value of 92.7%. For the corresponding 1σ values see Table C.1. From this we can conclude that the SR cannot be derived with an accuracy better than 3%.

Table C.1: SRs via different methods. Error approximately 3%.

Method	SR (%)
Image space, no correction of residual BG	72.8
Image space, correction of residual BG	92.7
Image space, correction of residual BG - 1σ	89.6
Image space, correction of residual BG + 1σ	96.0
Fourier space, sinc and diffusion corrected	95.1
Coherent energy (using Zernike coefficients)	93.7

The low precision of SR calculated in the image space is mainly due to this residual background features. This is the strongest argument to calculate SRs in the Fourier space, if there is the need for high precision results (which is usually not the case). Another argument is that if the sampling is close to the Nyquist limit, the finite pixel size and any asymmetry of the peak in respect to the pixel center starts playing a significant role. In Fourier space we correct for the finite pixel size by a simple division with a sinc-function and are not affected by a translation of a PSF over a pixel.

C.2 SR via Fourier space

To calculate the SR in the Fourier space we make use of the relation

$$SR = \frac{\text{PSF}(\alpha = 0)}{\text{PSF}_{\text{theo}}(\alpha = 0)} = \frac{\int \text{OTF}(f)}{\int \text{OTF}_{\text{theo}}(f)}. \quad (\text{C.1})$$

C.2.1 Finite pixel size

To take into account the limited sampling due to the finite pixel size we need to modify the perfect MTF by a division of the appropriate sinc-function. The solid line in Fig. C.3 represents a perfect detector MTF taking into account the finite pixel size. The range in which the MTF is showed is limited by the theoretical cut-off frequency D/λ .

C.2.2 Diffusion

Apart from the correction for the finite pixel size, the diffusion process further degrades the detector MTF. The larger the diffusion length of the minority carriers in the detector material, the more signal is detected from the adjacent pixels, having exposed only the central pixel to photons. During the course of the project, no measurements could be performed to quantify the diffusion of the CONICA detector. In principle, there are two ways of doing this:

- illuminating the detector with very fast optics, ensuring that the diameter corresponding to an Airy spot is only a fraction of the pixel size. Then the detector response can be measured for different spot positions;
- fixing a pinhole smaller than the pixel size onto the chip surface.

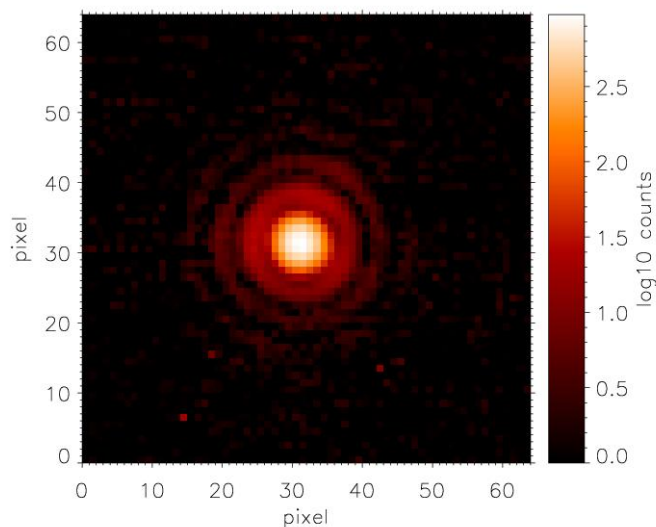


Figure C.1: A high SR calibration PSF taken with narrow-band filter NB2.17 and camera C50S. With logarithmic intensity scale, up to four diffraction rings can be seen.

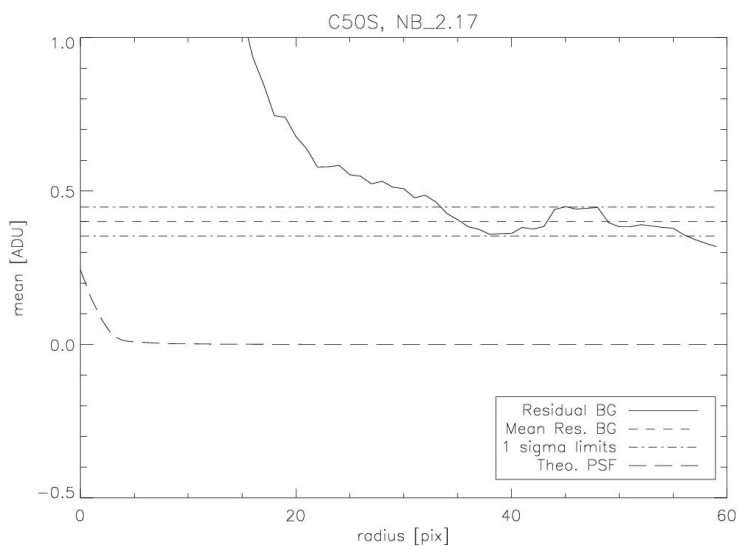


Figure C.2: Estimation of the residual background using the almost perfect PSF shown in Fig. C.1. The residual background is estimated by the integrated signal of concentric rings with a width of 5 pixel and a varying radius corresponding to the abscissa. Even if the frame was background corrected, stray light and noise features remain to be corrected for. To give evidence that the signal of a theoretical diffraction-limited PSF can be neglected already a few pixel away from its core, the long-dashed line plots the expected signal for this case.

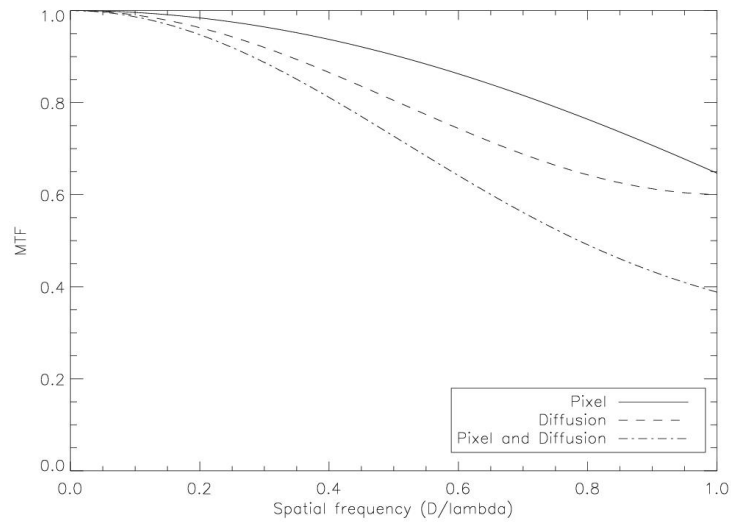


Figure C.3: Influence of the different corrections on the detector MTF. The finite pixel size is corrected for through a simple division by a sinc-function. The MTF for diffusion solely corresponds to the Fourier transform of the determined Aladdin detector response. Certainly, the “real” case has to take into account both effects: finite pixel size and diffusion.

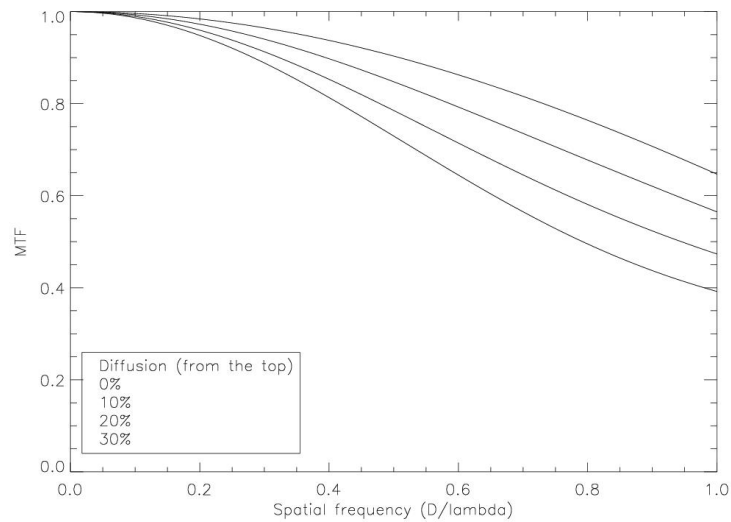


Figure C.4: Detector MTF for different diffusion coefficients. The correction for the finite pixel size is included. The zero diffusion curve shows the detector MTF only corrected for finite pixel size.

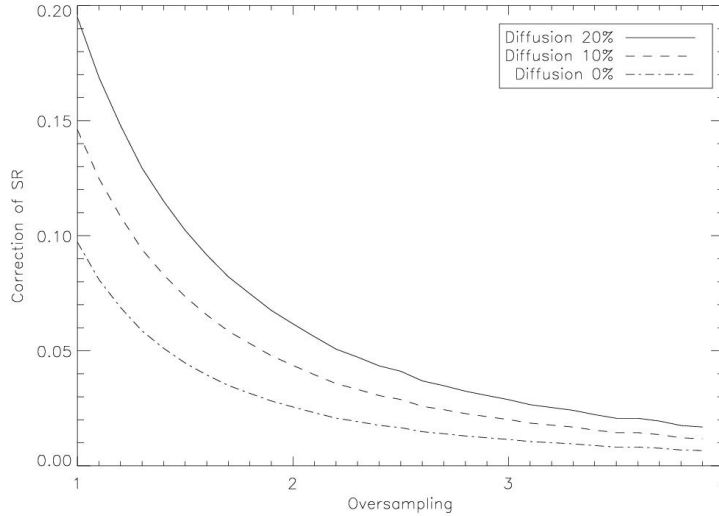


Figure C.5: Demonstration of the influence of different diffusion coefficients to the SR in dependence of the oversampling factor. An oversampling factor of 1 corresponds to Nyquist sampling. Obviously, the influence of diffusion decreases the more the PSF is oversampled. The zero diffusion curve shows the effect of finite pixel sampling solely. It is noteworthy that for the Nyquist sampling case even without any diffusion the minimum correction of SR is still 10%.

A measurement of the detector diffusion by the first method can be found in Finger et al. (1998). The MTF measurement of a Hawaii HgCdTe infrared array yields that 42% of the total energy diffuses into the neighboring pixel. Due to the lack of measurements for the Aladdin InSb array a rough estimate of the diffusion can be obtained by scaling the results for the Hawaii chip to the Aladdin chip. If we assume diffusion of the photon-generated electron-hole pairs to behave linearly in one dimension then diffusion over the chip surface will drop down quadratically with the distance from the center of generation. By this means we may estimate the diffusion η for the Aladdin array taking into account a pixel size of $18\ \mu\text{m}$ and $27\ \mu\text{m}$ for the Hawaii and the Aladdin array respectively:

$$\eta_{\text{Aladdin}} = \frac{18^2}{27^2} = 0.18 \quad (\text{C.2})$$

The corresponding detector responses are:

HAWAII			ALADDIN		
3.50	7.00	3.50	1.50	3.00	1.50
7.00	58.00	7.00	3.00	82.00	3.00
3.50	7.00	3.50	1.50	3.00	1.50

The given pixel values are normalized to a total flux of 100%. Note, that for simplicity the detector response of the Hawaii array is written symmetrically, even if different diffusion for columns and rows was measured (Finger et al. 1998). It is a trivial consequence of the assumption of quadratic behavior that the edge pixel contain half of the intensity of the directly neighboring pixels. From now on, a diffusion of 18% will be assumed which turns out to be in good agreement with related

experimental results (expected SRs). The degradation of the MTF due to this diffusion solely and the MTF according to both corrections is shown in Fig. C.3. Figure C.4 demonstrates the variation of the MTF with different diffusion coefficients. The correction for the finite pixel size is included. In general, the correction for the finite pixel size should not be neglected, since it is needed in any case (if we are not very far away from Nyquist sampling).

Figure C.5 demonstrates the importance of including the diffusion correction into SR calculations. The difference of SR is plotted versus the oversampling factor. As expected the impact becomes smaller the the oversampling factor is. Note the important correction of SR in the case of Nyquist sampling (1 x oversampling) that comes to approximately 15% for a diffusion of 20%. Even for a perfect detector response ($\eta = 0$) Fig. C.5 clearly shows that the correction for the finite pixel size must not be neglected for oversampling factor close to Nyquist.

Oversampling values for the camera objectives C25S/C25L and C50S for the narrow-band filters of CONICA can be found in Tab. B.1.

Appendix D

PD results for broadband and neutral density filters

During Science Verification in October 2002 PD data were taken¹ approximately six month after the commissioning period. These data allow to analyze the long term stability of the calibrated static aberrations. Furthermore, to the first time combined measurements of broadband, neutral density and narrowband filters allow one to derive the contribution of the broadband and neutral densities filters to the wavefront degradation.

D.1 Image SR versus PD SR

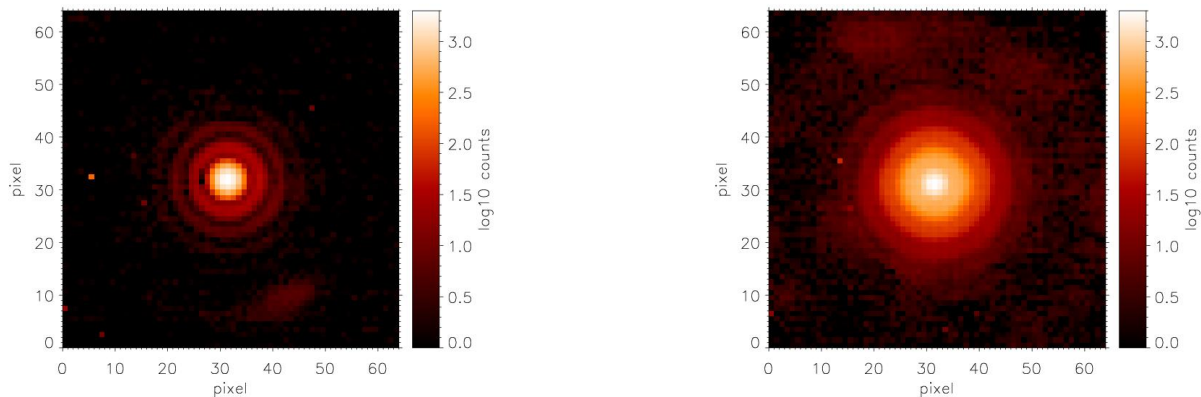


Figure D.1: In-focus and out-of-focus image (4 mm) in L'-band with camera C50S. Images are taken with the aid of the Zernike-tool. The SR exceeds 95%.

The in-focus image is taken to calculate a SR on the image. The results of wavefront sensing from PD are applied to estimate a SR via the coherent energy. The SRs on the image are calculated in the Fourier space as described in Sect. 4.2.2 and Appendix C. The SRs on the image are corrected for the finite pixel size (sinc-correction) and for the detector MTF pertaining to diffusion. For the

¹These technical data were acquired by Chris Lidman from 03 Oct 2002 to 05 Oct 2002.

Aladdin array a diffusion of 18% is assumed. The results shown in Table D.1 confirm the CONICA optics to be in good shape. As specified, SRs in the JH-band are above 80% and in the K-Band well above 90%. In L-band SRs are close to 100%. On the in-focus images up to 5 diffraction rings can be seen (see Fig. D.1). Since we do not expect a significant degradation of image quality in the L- and M-bands, the low SR for L'+ND_Long indicate the ND_Long-Filter to be aberrant. This conclusion is underlined by the PD results.

Filter	SR by PD	SR by image
NB.2.17	93.7	95.1
NB.2.17+Ks	95.3	93.8
Ks	96.1	97.1
Ks+ND_Short	96.0	95.0
NB.1.64	96.3	87.1
H	97.0	88.3
H+ND_Short	96.8	91.4
NB.1.26	92.1	84.1
NB.1.26+J	92.5	81.2
J+ND_Short	94.4	87.0
L'	99.4	96.2
L'+ND_Long	92.0	88.6
NB.3.74	99.5	94.2
NB.4.05	99.8	94.8
NB.4.05+L'	99.5	94.2

Table D.1: CONICA internal SRs calculated via PD results (coherent energy) and directly on the image.

D.2 PD calibration results

The results of the PD reduction are shown in Table D.2, D.3 and D.4. For comparison the relevant results of Commissioning 4 are given in Table D.5. The values for L'+ND_Long in respect to the ones for L' confirm the degradation of imaging quality due to ND_Long. Note, that the PD results alone would only be a hint, but in this case no proof for an aberrant ND_Long-filter since no verification measurement for the alignment of the both pupils exists. Only the ND filters are concerned by this question, since they are implemented on the pupil wheel. Nevertheless, the consistency with the SR results and the zero deviations for the ND_Short filter let conclude that the full pupil and the combined pupil of the ND-filters are properly aligned. (PD measurements are very sensitive to the pupil alignment.)

In general, apart from a residual focus term, the combined PD data using a broadband and a narrowband filter together show no significant deviations. Thus, in the database the higher order aberrations of the broadband filters J, H and K can be handled as null vectors.

To point out the drift of aberrations during the 6 months between these measurements, the difference is calculated in Table D.6. Disregarding the focus term, there is no significant drift detectable. The small deviations in the focus terms are most likely due a service intervention in summer 2002.

Table D.2: Raw aberrations in nmRMS including camera and filters. C50S (S13), 0/2 mm, science verification data (Oct 2002).

Filter	λ_c (μm)	4	5	6	7	8	9	10	11	12	13	14	15
NB.1.64	1.644	-20	-36	21	-3	0	2	18	0	4	-1	3	-2
H	1.65	-1	-38	20	-7	6	5	12	3	-3	-1	1	-3
H+ND_Short	1.65	-6	-39	20	-7	6	5	12	-1	-4	-1	1	-3
NB.1.26	1.26	2	-46	24	-12	5	7	14	3	2	-3	8	0
NB.1.26+J	1.26	-22	-39	21	-12	5	7	12	3	2	-3	12	-1
J+ND_Short	1.25	-2	-30	24	-11	8	6	12	16	2	-4	8	-1

Table D.3: Raw aberrations in nmRMS including camera and filters. C50S (S13), 0/4 mm, science verification data (Oct 2002).

Filter	λ_c (μm)	4	5	6	7	8	9	10	11	12	13	14	15
NB.2.17	2.17	63	-35	32	-19	7	9	14	22	1	-1	3	-3
NB.2.17+Ks	2.17	33	-41	47	-15	9	9	14	6	1	0	2	-2
Ks	2.15	15	-44	44	-8	9	6	13	-3	-2	-1	4	-2
Ks+ND_Short	2.15	5	-44	47	-7	8	5	13	-9	-3	-1	3	-2

Table D.4: Raw aberrations in nmRMS including camera and filters. C25L (L27), 0/4 mm, science verification data (Oct 2002).

Filter	λ_c (μm)	4	5	6	7	8	9	10	11	12	13	14	15
L'	3.8	39	-2	-14	-4	-11	4	-1	5	7	-4	-8	-5
L'+ND_Long	2.8	-88	15	70	-27	-77	-44	-83	-15	23	0	-2	18
NB.3.74	3.74	-27	-11	-15	4	2	6	-5	-25	5	-1	-4	0
NB.4.05	4.05	16	1	-1	-1	-16	-4	3	-9	5	3	-3	-6
NB.4.05+L'	4.05	27	5	-7	-3	-21	-7	3	-19	9	-1	-8	-11

Table D.5: Raw aberrations in nmRMS including camera and filters. C50S (S13), 0/2 mm: NB.1.26, NB.1.64, 0/4 mm: NB.2.17, comm4 data (April 2002).

Filter	λ_c (μm)	4	5	6	7	8	9	10	11	12	13	14	15
NB.1.26	1.257	-18	-42	24	-9	0	1	9	-11	1	0	9	-1
NB.1.64	1.644	-36	-34	23	-1	-4	0	16	-9	5	0	4	-2
NB.2.17	2.166	10	-33	33	-16	8	8	15	-11	3	1	3	-2

Table D.6: Drift of aberrations: a_i (Oct 2002) - a_i (April 2002)

Filter	λ_c (μm)	4	5	6	7	8	9	10	11	12	13	14	15
NB.1.26	1.257	20	-4	0	-3	5	6	5	14	1	-3	-1	1
NB.1.64	1.644	16	-2	-2	-2	4	2	2	9	-1	-1	-1	0
NB.2.17	2.166	53	-2	-1	-3	-1	1	-1	33	-2	-2	0	-1

Note that even the spherical aberration of NB_2.17 with $a_{11} = 33\text{nm RMS}$ affects the SR ratio by a loss less than 1%. It is not clear if the slightly increased spherical aberration plays along with the modified focus term or if this can be interpreted as indication for a small drift.

D.3 Conclusion

The CONICA internal PD measurements confirm the image quality to be very good. All measured filters and camera combinations yield SRs better than specified. There is no significant wavefront aberration stemming from the broadband filters and the neutral density filter for short wavelengths (ND_Short). *The neutral density filter for long wavelengths (ND_Long) seems to behave aberrant.* An update of the database is necessary. One might even think about a replacement if appropriate. In any case, a second test measurement is recommended (measuring ND_Long together with NB_3.74 and NB_4.05).

No significant drift of the higher order aberrations between Commissioning 4 (April 2002) and October 2002 could be detected.

Appendix E

List of publications

- A. Blanc, T. Fusco, **M. Hartung**, L. M. Mugnier, and G. Rousset. Calibration of NAOS and CONICA static aberrations: Application of the phase diversity technique. *Astron. Astrophys.*, 399:373–383, 2003.
- M. Hartung**, A. Blanc, T. Fusco, F. Lacombe, L. M. Mugnier, G. Rousset, and R. Lenzen. Calibration of NAOS and CONICA static aberrations: Experimental results. *Astron. Astrophys.*, 399:385–394, 2003a.
- M. Hartung**, R. Lenzen, R. Hofmann, A. Boehm, W. Brandner, G. Finger, T. Fusco, F. Lacombe, W. Laun, P. Granier, C. Storz, and K. Wagner. CONICA design, performance and final laboratory tests. In M. Iye and A. F. Moorwood, editors, *Instrument Design and Performance for Optical/Infrared Ground-based Telescopes*, volume 4841 of *Proc. SPIE*, 2003b.
- M. Hartung**, A. Blanc, T. Fusco, F. Lacombe, L. M. Mugnier, G. Rousset, and R. Lenzen. Calibration of CONICA static aberrations by phase diversity. In M. Iye and A. F. Moorwood, editors, *Instrument Design and Performance for Optical/Infrared Ground-based Telescopes*, volume 4841 of *Proc. SPIE*, 2003c.
- M. Hartung**, P. Bizenberger, A. Boehm, W. Laun, R. Lenzen, and K. Wagner. First test results and calibration methods of CONICA as a stand-alone device. In M. Iye and A. F. Moorwood, editors, *Optical and IR Telescope Instrumentation and Detectors*, volume 4008 of *Proc. SPIE*, pages 830–841, 2000.
- R. Schödel, T. Ott, R. Genzel, R. Hofmann, M. Lehnert, A. Eckert, N. Mouawad, T. Alexander, M. J. Reid, R. Lenzen, **M. Hartung**, F. Lacombe, D. Rouan, E. Gendron, G. Rousset, A.-M. Lagrange, W. Brandner, N. Ageorges, C. Lidman, A. Moorwood, J. Spyromilio, A. Renzini, N. Hubin, and K. M. Menten. A star in a 15.2-year orbit around the supermassive black hole at the centre of the Milky Way. *Nature*, 419:694–696, 2002.
- T. Ott, R. Schödel, R. Genzel, A. Eckart, F. Lacombe, D. Rouan, R. Hoffmann, M. Lehnert, T. Alexander, A. Sternberg, M. Reid, W. Brandner, R. Lenzen, **M. Hartung**, E. Gendron, Y. Clénet, P. Léna, G. Rousset, A.-M. Lagrange, N. Ageorges, N. Hubin, C. Lidman, A.F.M. Moorwood, A. Renzini, J. Spyromilio, L.E. Tacconi-Garman, K.M. Menten, and N. Mouawad. Inward Bound: Studying the Galactic Centre with NAOS/CONICA. *The Messenger*, 111:1–8, 2003.

- W. Brandner, G. Rousset, R. Lenzen, N. Hubin, F. Lacombe, R. Hofmann, A. Moorwood, A.-M. Lagrange, E. Gendron, **M. Hartung**, P. Puget, N. Ageorges, P. Biereichel, H. Bouy, J. Charton, G. Dumont, T. Fusco, Y. Jung, M. Lehnert, J.-L. Lizon, G. Monnet, D. Mouillet, C. Moutou, D. Rabaud, C. Röhrle, S. Skole, J. Spyromilio, C. Storz, L. Tacconi-Garman, and G. Zins. NAOS+CONICA at YEPUN: First VLT adaptive optics system sees first light. *The Messenger*, 107:1–6, 2002.
- R. Lenzen, **M. Hartung**, W. Brandner, G. Finger, N. Hubin, F. Lacombe, A.-M. Lagrange, M. Lehnert, A. Moorwood, and D. Mouillet. NAOS-CONICA first on sky results in a variety of observing modes. In M. Iye and A. F. Moorwood, editors, *Instrument Design and Performance for Optical/Infrared Ground-based Telescopes*, volume 4841 of *Proc. SPIE*, 2002.
- A. M. Lagrange, Gael Chauvin, T. Fusco, E. Gendron, D. Rouan, **M. Hartung**, F. Lacombe, D. Mouillet, G. Rousset, P. Drossart, R. Lenzen, C. Moutou, W. Brandner, N. Hubin, Y. Clenet, A. Stolte, R. Schödel, G. Zins, and J. Spyromilio. First diffraction limited images at the VLT with NAOS and CONICA. In M. Iye and A. F. Moorwood, editors, *Instrument Design and Performance for Optical/Infrared Ground-based Telescopes*, volume 4841 of *Proc. SPIE*, 2002.
- N. Ageorges, R. Lenzen, **M. Hartung**, W. Brandner, E. Gendron, A. Moorwood, and A.M. Lagrange. Polarimetry with adaptive optics at the ESO Very Large Telescope (Yepun). In S. Fineschi, editor, *Polarimetry in Astronomie*, volume 4843 of *Proc. SPIE*, 2002.
- G. Chauvin, A.-M. Lagrange, H. Beust, T. Fusco, D. Mouillet, F. Lacombe, E. Gendron, G. Rousset, D. Rouan, W. Brandner, R. Lenzen, N. Hubin, and **M. Hartung**. VLT/NACO adaptive optics imaging of the TY CrA system: A fourth stellar component candidate detected. *Astron. Astrophys.*, 2003, submitted.

Bibliography

References

- N. Ageorges, R. Lenzen, M. Hartung, W. Brandner, E. Gendron, A. Moorwood, and A.M. Lagrange. Polarimetry with adaptive optics at the ESO Very Large Telescope (Yepun). In S. Fineschi, editor, *Polarimetry in Astronomie*, volume 4843 of *Proc. SPIE*, 2002.
- C. W. Allen. *Allen's Astrophysical Quantities*. AIP Press, fourth edition, 2000.
- H. W. Babcock. The Possibility of Compensating Astronomical Seeing. *Publ. Astron. Society Pacific*, 65:229–236, October 1953.
- A. Blanc. *Identification de Réponse impulsionnelle et Restauration d'Images: Apports de la Diversité de Phase*. PhD thesis, Université Paris XI UFR Scientifique d'Orsay, 2002.
- A. Blanc, T. Fusco, M. Hartung, L. M. Mugnier, and G. Rousset. Calibration of NAOS and CONICA static aberrations. Application of the phase diversity technique. *Astron. Astrophys.*, 399:373–383, March 2003.
- A. Blanc, J. Idier, and L. Mugnier. Novel estimator for the aberrations of a space telescope by phase diversity. In J. B. Breckinridge and P. Jakobsen, editors, *UV, Optical, and IR Space Telescopes and Instruments*, volume 4013 of *Proc. SPIE*, pages 728–736, 2000.
- M. Born and E. Wolf. *Principles of Optics*. Cambridge University Press, seventh edition, 1999.
- W. Brandner, G. Rousset, R. Lenzen, N. Hubin, F. Lacombe, R. Hofmann, A. Moorwood, A.-M. Lagrange, E. Gendron, M. Hartung, P. Puget, N. Ageorges, P. Biereichel, H. Bouy, J. Charton, G. Dumont, T. Fusco, Y. Jung, M. Lehnert, J.-L. Lizon, G. Monnet, D. Mouillet, C. Moutou, D. Rabaud, C. Röhrle, S. Skole, J. Spyromilio, C. Storz, L. Tacconi-Garman, and G. Zins. NAOS+CONICA at YEPUN: First VLT adaptive optics system sees first light. *The Messenger*, 107:1–6, 2002.
- R. A. Carreras, S. R. Restaino, and D. C. Duneman. Laboratory experiment using phase diversity to extract higher order Zernike coefficients. In T.J. Schulz and D.L. Snyder, editors, *Image Reconstruction and Restoration*, volume 2302 of *Proc. SPIE*, pages 323–329, 1994.
- D. Currie, D. Le Mignant, B. Svensson, S. Tordo, and D. Bonaccini. 3D structure and dynamics of the Homunculus of Eta Carinae: an application of the Fabry Perot, ADONIS and AO software. *The Messenger*, 102:25–27, 2000.
- K. Davidson and R. M. Humphreys. Eta Carinae and Its Environment. *Ann. Rev. Astron. Astrophys.*, 35:1–32, 1997.

- G. Demoment. Image reconstruction and restoration: Overview of common estimation structure and problems. *IEEE Transactions on Acoustics speech and Signal Processing*, 37:2024–2036, 1989.
- M. P. Ekstrom and R. L Rhoads. *J. Comput. Phys.*, 14:319, 1974.
- ESO, NAOS-CONICA, 2002. URL <http://www.eso.org/instruments/naos/>.
- P. Feautrier, P. Kern, R. Dorn, G. Rousset, P. Rabou, S. Laurent, J.-L. Lizon, E. Stadler, Y. Magnard, O. Rondeaux, M. Cochard, D. Rabaud, A. Delboulbe, P. Puget, and N. Hubin. The NAOS visible wave front sensor. In P. L. Wizinowich, editor, *Adaptive Optical Systems Technology*, volume 4007 of *Proc. SPIE*, pages 396–407, 2000.
- P. Feautrier, G. Rousset, R. J. Dorn, C. Cavadore, J. Charton, C. Cumani, T. Fucso, N. Hubin, P. Kern, J.-L. Lizon, Y. Magnard, P. Puget, D. Rabaud, P. Rabou, and E. Stadler. Performances and results on the sky of the NAOS visible wavefront sensor. In P. L. Wizinowich and D. Bonaccini, editors, *Adaptive Optical System Technologies II*, volume 4839 of *Proc. SPIE*, pages 250–258, 2003.
- G. Finger, 2002. ESO, private communication.
- G. Finger, H. Mehrgan, M. Meyer, A. Moorwood, G. Nicolini, and J. Stegmeier. Infrared detector development programs for the VLT instruments at the European Southern Observatory. In A. M. Fowler, editor, *Infrared Astronomical Instrumentation*, volume 3354 of *Proc. SPIE*, pages 87–98, 1998.
- A. M. Fowler, J. B. Heynssens, I. Gatley, F. J. Vrba, H. D. Ables, A. W. Hoffman, and J. T. Woolaway. Aladdin: the 1024 x 1024 insb array test results. In A. M. Fowler, editor, *Infrared Detectors and Instrumentation for Astronomy*, volume 2475 of *Proc. SPIE*, pages 27–33, 1995.
- T. Fusco, J.-M. Conan, F. Marchis, G. Chauvin, G. Rousset, A.-M. Lagrange, D. Mouillet, and F. Roddier. Deconvolution of astronomical images obtained from ground-based telescopes with adaptive optics. In P. L. Wizinowich, editor, *Adaptive Optical System Technologies II*, volume 4839 of *Proc. SPIE*, pages 1065–1075, 2003.
- E. L. Gates, S. R. Restaino, R. A. Carreras, R. C. Dymale, and G. C. Loos. Phase diversity as an on-line wavefront sensor: experimental results. In T.J. Schulz and D.L. Snyder, editors, *Image Reconstruction and Restoration*, volume 2302 of *Proc. SPIE*, pages 330–339, 1994.
- E. Gendron, F. Lacombe, D. Rouan, J. Charton, C. Collin, B. Lefort, C. Marlot, G. Michet, G. Nicol, S. Pau, V. D. Phan, B. Talureau, J. L. Lizon, and N. Hubin. NAOS Infrared wave-front sensor design and performance. In P. L. Wizinowich and D. Bonaccini, editors, *Adaptive Optical System Technologies II*, volume 4839 of *Proc. SPIE*, pages 195–205, 2003.
- R. Genzel, C. Pichon, A. Eckart, O. E. Gerhard, and T. Ott. Stellar dynamics in the Galactic Centre: proper motions and anisotropy. *Mon. Notices Royal Astron. Society*, 317:348–374, 2000.
- R. A. Gonsalves. Phase retrieval and diversity in adaptive optics. *Optical Engineering*, 21(5):829–832, 1982.
- S. Gordon, B. Koribalski, S. Houghton, and K. Jones. A guide to TAURUS-2 Fabry-Perot data reduction. *Mon. Notices Royal Astron. Society*, 315:248–262, 2000.

-
- P. Granier. Participation to the tests of the Adaptive Optics system of the VLT and evaluation of its performance. Master's thesis (Diplôme d'Etudes Supérieures Spécialisées), Observatoire de Paris, 2001.
- T. R. Gull, S. Johannson, and K. Davidson, editors. *Eta Carinae and Other Mysterious Stars: The Hidden Opportunities of Emission Spectroscopy.*, 2001.
- J. W. Hardy. *Adaptive Optics for Astronomical Telescopes.* Oxford University Press, 1998.
- J. W. Hardy, J. E. Lefebvre, and C. L. Koliopoulos. Real-time atmospheric compensation. *J. Opt. Society America*, 67(3):360–369, 1977.
- M. Hartung, P. Bizenberger, A. Böhm, W. Laun, R. Lenzen, and K. Wagner. First test results and calibration methods of CONICA as a stand-alone device. In M. Iye and A. F. Moorwood, editors, *Optical and IR Telescope Instrumentation and Detectors*, volume 4008 of *Proc. SPIE*, pages 830–841, 2000.
- M. Hartung, A. Blanc, T. Fusco, F. Lacombe, L. M. Mugnier, G. Rousset, and R. Lenzen. Calibration of CONICA static aberrations by phase diversity. In M. Iye and A. F. Moorwood, editors, *Instrument Design and Performance for Optical/Infrared Ground-based Telescopes*, volume 4841 of *Proc. SPIE*, 2002a.
- M. Hartung, A. Blanc, T. Fusco, F. Lacombe, L. M. Mugnier, G. Rousset, and R. Lenzen. Calibration of NAOS and CONICA static aberrations. Experimental results. *Astron. Astrophys.*, 399:385–394, March 2003.
- M. Hartung, R. Lenzen, R. Hofmann, A. Böhm, W. Brandner, G. Finger, T. Fusco, F. Lacombe, W. Laun, P. Granier, C. Storz, and K. Wagner. CONICA design, performance and final laboratory tests. In M. Iye and A. F. Moorwood, editors, *Instrument Design and Performance for Optical/Infrared Ground-based Telescopes*, volume 4841 of *Proc. SPIE*, 2002b.
- T. Herbst. *New views in the Near Infrared: A Fabry-Perot interferometer for galactic and extragalactic astronomy.* PhD thesis, Graduate School of Cornell University, 1990.
- H. Holzwarth. Entwicklung eines Korrektors der atmosphärischen Dispersion für den nahen Infrarotbereich. Diplomarbeit, Universität Heidelberg, 1992.
- R. D Hudson and J. W. Hudson. The Military Applications of Remote Sensing by Infrared. volume 63 of *Proc. IEEE*, pages 104–128, 1975.
- S. M. Jefferies, M. Lloyd-Hart, E. Keith, and J. Georges. Noise propagation in wave-front sensing with phase diversity. *Appl. Opt.*, 41(11):2095–2102, 2002.
- R. L. Kendrick, D. S. Acton, and A. L. Duncan. Phase-diversity wave-front sensor for imaging systems. *Appl. Optics*, 33(27):6533–6546, 1994.
- J. Klare. Tests und Kalibration eines kryogenen Fabry-Perot-Interferometers für die hochauflösende Infrarotkamera CONICA des Very Large Telescope. Diplomarbeit, Universität Heidelberg, 1996.
- F. Lacombe, G. Zins, J. Charton, G. Chauvin, G. Dumont, P. Feautrier, T. Fusco, E. Gendron, N. Hubin, P. Kern, A.-M. Lagrange, D. Mouillet, P. Puget, D. Rabaud, P. Rabou adn G. Rousset, and J. L. Beuzit. NAOS: from an AO system to an Astronomical Instrument. In P. L. Wizinowich, editor, *Adaptive Optical System Technologies II*, volume 4839 of *Proc. SPIE*, pages 150–154, 2003.

- D. J. Lee, M. C. Roggemann, and B. M. Welsh. Cramér-rao analysis of phase-diverse wave-front sensing. *J. Opt. Soc. Am. A*, 16(5):1005–1015, 1999.
- D.J. Lee, B.M. Welsh, and M.C. Roggemann. Diagnosing unknown aberrations in an adaptive optics system by use of phase diversity. *Opt. Lett.*, 22(13):952–954, 1997.
- R. Lenzen, R. Hofmann, P. Bizenberger, and A. Tusche. Conica: The high resolution near-infrared camera for the ESO VLT. In A. M. Fowler, editor, *Infrared Astronomical Instrumentation*, volume 3354 of *Proc. SPIE*, pages 606–614, 1998.
- R. J. A. Little and D. B. Rubin. On Jointly Estimating Parameters and Missing Data by Maximizing the Complete-Data Likelihood. *The American Statistician*, 37(3):218–220, 1983.
- M. G. Löfdahl and G. B. Scharmer. Wavefront sensing and image restoration from focused and defocused solar images. *Astron. Astrophys.*, 107:243–264, 1994.
- M. G. Löfdahl, G. B. Scharmer, and W. Wei. Calibration of a deformable mirror and strehl ratio measurements by use of phase diversity. *Appl. Optics*, 39(1):94–103, 2000.
- E. Marchetti, N. Hubin, E. Fedrigo, J. Brynnel, B. Delabre, R. Donaldson, F. Franza, R. Conan, M. Le Louarn, C. Cavadore, A. Balestra, D. Baade, J.-L. Lizon, R. Gilmozzi, G. Monnet, R. Ragaini, C. Arcidiacono, A. Baruffolo, E. Diolaiti, J. Farinato, E. Viard, D. Butler, S. Hippler, and A. Amorim. MAD the ESO mulit-conjugate adaptive optics demonstrator. In P. L. Wizinowich, editor, *Adaptive Optical System Technologies II*, volume 4839 of *Proc. SPIE*, pages 317–328, 2003.
- M. J. McCaughrean. *The Astronomical Application of Infrared Array Detectors*. PhD thesis, University of Edinburgh, 1988.
- Ian S. McLean. *Electronic Imaging in Astronomy*. John Wiley & Sons, Ltd, Chichester, 1997.
- M. Meyer, G. Finger, H. Mehrgan, G. Nicolini, and J. Stegmeier. The ESO Infrared Detector High Speed Array Control and Processing Electronic IRACE. In A. M. Fowler, editor, *Infrared Astronomical Instrumentation*, volume 3354 of *Proc. SPIE*, pages 134–138, 1998.
- L. Meynadier, V. Michau, M. T. Velluet, J.-M. Conan, L. M. Mugnier, and G. Rousset. Noise propagation in wave-front sensing with phase diversity. *Appl. Opt.*, 38(23):4967–4979, 1999.
- A. V. Moiseev. Reduction of CCD observation with scanning Fabry-Perot interferometer. *Bull. Spec. Astrophys. Obs.*, 54, 2002.
- A. F. Moorwood. ISAAC: a 1- to 5-um imager/spectrometer for the VLT. In Arne L. Ardeberg, editor, *Optical Telescopes of Today and Tomorrow*, volume 2871 of *Proc. SPIE*, pages 1146–1151, 1997.
- J. A. Morse, K. Davidson, J. Bally, D. Ebbets, B. Balick, and A. Frank. Hubble Space Telescope Wide Field Planetary Camera 2 Observations of Eta Carinae. *The Astronomical Journal*, 116:2443–2461, November 1998.
- J. A. Morse, R. M. Humphreys, and A. Damineli, editors. *Eta Carinae At The Millennium*, 1999.
- D. Mouillet, S. Marteau, G. Zins, J.-M. Conan, E. Gendron, L. Rousset-Rouvière, J.-L. Beuzit, A.-M. Lagrange, C. Moutou, and G. Rousset. Preparation tool for optimal observations with NAOS-CONICA. In P. L. Wizinowich, editor, *Adaptive Optical System Technologies II*, volume 4839 of *Proc. SPIE*, pages 107–113, 2003.

-
- P. E. Müller. Grisms und Wollaston-Prismen für die IR-Kamera CONICA (VLT). Diplomarbeit, Universität Heidelberg, 1995.
- R. J. Noll. Zernike polynomials and atmospheric turbulence. *J. Opt. Soc. Am. A*, 66(3):207–211, 1976.
- T. Ott, R. Schödel, R. Genzel, A. Eckart, F. Lacombe, D. Rouan, R. Hoffmann, M. Lehnert, T. Alexander, A. Sternberg, M. Reid, W. Brandner, R. Lenzen, M. Hartung, E. Gendron, Y. Clénet, P. Léna, G. Rousset, A.-M. Lagrange, N. Ageorges, N. Hubin, C. Lidman, A.F.M. Moorwood, A. Renzini, J. Spyromilio, L.E. Tacconi-Garman, K.M. Menten, and N. Mouawad. Inward Bound: Studying the Galactic Centre with NAOS/CONICA. *The Messenger*, 111:1–8, 2003.
- R. G. Paxman, T. J. Schulz, and J. R. Fienup. Joint estimation of object and aberrations by using phase diversity. *J. Opt. Soc. Am. A*, 9(7):1072–1085, 1992.
- S. Restaino. Wave-front sensing and image deconvolution of solar data. *Appl. Optics*, 35(31):7442–7449, 1992.
- G. Rousset, J. C. Fontanella, P. Kern, P. Gigan, and F. Rigaut. First diffraction-limited astronomical images with adaptive optics. *Astron. Astrophys.*, 230:L29–L32, 1990.
- G. Rousset, F. Lacombe, P. Puget, E. Gendron, R. Arsenault, P. Y. Kern, D. Rabaud, P.-Y. Madec, N. Hubin, G. Zins, E. Stadler, P. Gigan J. Charton, and P. Feautrier. Status of the VLT Nasmyth adaptive optics system (NAOS). In P. L. Wizinowich, editor, *Adaptive Optical Systems Technology*, volume 4007 of *Proc. SPIE*, pages 72–81, 2000.
- G. Rousset, F. Lacombe, P. Puget, N. Hubin, E. Gendron, J.-M. Conan, P. Y. Kern, P.-Y. Madec, D. Rabaud, D. Mouillet, A.-M. Lagrange, and F. J. Rigaut. Design of the Nasmyth adaptive optics system (NAOS) of the VLT. In D. Bonaccini and R. K. Tyson, editors, *Adaptive Optical System Technologies*, volume 3353 of *Proc. SPIE*, pages 508–516, 1998.
- R. Schödel, T. Ott, R. Genzel, R. Hofmann, M. Lehnert, A. Eckert, N. Mouawad, T. Alexander, M. J. Reid, R. Lenzen, M. Hartung, F. Lacombe D. Rouan, E. Gendron, G. Rousset, A.-M. Lagrange adn W. Brandner, N. Ageorges, C. Lidman, A. Moorwood, J. Spyromilio, A. Renzini, N. Hubin, and K. M. Menten. A star in a 15.2-year orbit around the supermassive black hole at the centre of the Milky Way. *Nature*, 419:694–696, 2002.
- J. H. Seldin and R. G. Paxman. Phase-diverse speckle reconstruction of solar data. In *Image Reconstruction and Restoration*, volume 2302 of *Proc. SPIE*, 1994.
- J.H. Seldin and R.G. Paxman. Closed-loop wavefront sensing for a sparse-aperture, phased-array telescope using broadband phase diversity. In *Imaging Technology and Telescopes*, volume 4091 of *Proc. SPIE*, pages 48–63, 2000.
- P. Spanoudakis, L. Zago, O. Chételat, R. Gentsch, and F. Mato Mira. Extremely high-resolution tip-tilt-piston mirror mechanism for the VLT-NAOS field selector. In P. L. Wizinowich, editor, *Adaptive Optical Systems Technology*, volume 4007 of *Proc. SPIE*, pages 408–415, 2000.
- K. Strehl. Über Luftschlieren und Zonenfehler. *Zeitschrift für Instrumentenkunde*, 22, 1902.
- B. J. Thelen, R. G. Paxman, D. A. Carrara, and J. H. Seldin. Maximum a posteriori estimation of fixed aberrations, dynamic aberrations, and the object from phase-diverse speckle data. *J. Opt. Soc. Am. A*, 16(5):1016–1025, 1999.

R. K. Tyson. *Principles of Adaptive Optics*. Academic Press, second edition, 1998.

W. Whaling, W. H. C. Anderson, M. T. Carle, J. W. Brault, and H. A. Zarem. Argon I Lines Produced in a Hollow Cathode Source, 332 nm to 5865 nm. *J. Res. Natl. Inst. Stand. Technol.*, 107 (2):149–169, 2002.

Technical Reports and Manuals

- K. Bickert. VLT Hardware - CONICA Detector Control Hardware - DCH Design Description. Final Design Report VLT-TRE-NIC-14200-0115, Issue 1.1, CONICA Consortium to ESO (MPE), December 1995.
- K. Bickert and A. Tusche. CONICA Instrument Software: Functional Specification. Final Design Report VLT-TRE-NIC-14200-0104, Issue 1.1, CONICA Consortium to ESO (MPIA), May 1997.
- W. Brandner, C. Lidman, and C. Moutou. NAOS-CONICA User Manual. User Manual VLT-MAN-ESO-14200-2761, Issue 1.5.1, ESO, January 2003.
- M. Hartung. Calibration of the static NAOS-CONICA aberrations. Manual VLT-TRE-ESO-14200-2849, CONICA Consortium to ESO (MPIA), in preparation 2003.
- R. Lenzen. CONICA Allignment Procedures. Final Design Report VLT-TRE-NIC-14200-0109, Issue 1.0, CONICA Consortium to ESO (MPIA), December 1995a.
- R. Lenzen. CONICA Assembly Procedures. Final Design Report VLT-TRE-NIC-14200-0108, Issue 1.2, CONICA Consortium to ESO (MPIA), December 1995b.
- R. Lenzen. CONICA Control Electronics Requirements. Final Design Report VLT-TRE-NIC-14200-0111, Draft 0, CONICA Consortium to ESO (MPIA), December 1995c.
- R. Lenzen. CONICA Critical Mechanical Design Study. Final Design Report VLT-TRE-NIC-14200-0102, Issue 1.4, CONICA Consortium to ESO (MPIA), December 1995d.
- R. Lenzen. CONICA Critical Optical Design Study. Final Design Report VLT-TRE-NIC-14200-0101, Issue 2.3, CONICA Consortium to ESO (MPIA), December 1995e.
- R. Lenzen. CONICA Design Specification. Final Design Report VLT-TRE-NIC-14200-0106, Issue 1.1, CONICA Consortium to ESO (MPIA), December 1995f.
- R. Lenzen. CONICA Fabry Perot Design Study. Final Design Report VLT-TRE-NIC-14200-0110, Issue 1.1, CONICA Consortium to ESO (MPIA), December 1995g.
- R. Lenzen. CONICA focal plane and Lyot stops. Final Design Report VLT-TRE-NIC-14200-0114, Issue 1.1, CONICA Consortium to ESO (MPIA), December 1995h.
- R. Lenzen. CONICA Grism Design Study. Final Design Report VLT-TRE-NIC-14200-0124, Issue 2.1, CONICA Consortium to ESO (MPIA), December 1995i.
- R. Lenzen. CONICA Software User Requirements. Final Design Report VLT-TRE-NIC-14200-0112, Issue 1.1, CONICA Consortium to ESO (MPIA), December 1995j.
- R. Lenzen. CONICA Product Assurance and Verification Plan. Final Design Report VLT-PLA-NIC-14200-0101, Issue 2.1, CONICA Consortium to ESO (MPIA), January 1996.
- R. Lenzen. CONICA Interface Control Document. Final Design Report VLT-ICD-NIC-14200-0107, Issue 2.4, CONICA Consortium to ESO (MPIA), March 1998.
- R. Lenzen and K. Wagner. CONICA Cables/Hoses Requirements. Final Design Report VLT-TRE-NIC-14200-0113, Issue 1.2, CONICA Consortium to ESO (MPIA), January 1996.

- D. Mouillet and T. Fusco. NAOS Test Report. Technical Report VLT-TRE-NAO-11650-1-000000-0004, Issue 1.0, NAOS Consortium to ESO (LAOG, ONERA), May 2002.
- Queensgate Instruments Ltd. *Queensgate Servo-stabilized Interferometer System, CS100 Controller, ET Series II and EC Series Etalons*, 1995. User's Guide.
- A. Tusche. CONICA Instrument Software - Instrument Control Software - ICS Design Description. Final Design Report VLT-SPE-NIC-14200-0124, Issue 1.0, CONICA Consortium to ESO (MPE), May 1997.
- K. Wagner. CONICA Control Electronics. Manual VLT-TRE-NIC-14200-0103, Issue 1.1, CONICA Consortium to ESO (MPIA), July 2001.

Abbreviations and Acronyms

ADC	Atmospheric Dispersion Compensator
ADC	Analog Digital Converter
ADU	Analogue Digital Unit
AMOS	Air Force Maui Optical Site
AO	Adaptive Optics
ARPA	Advanced Research Projects Agency
CONICA	COudé Near-Infrared CAmera
DFT	Discrete Fourier Transform
DIT	Detector Integration Time
DM	Deformable Mirror
ESO	European Southern Observatory
FCU	Fabry-Perot Control Units
FOV	Field Of View
FPI	Fabry-Perot Interferometer
FS	Field Selector
FWC	Full Well Capacity
FWHM	Full Width at Half Maximum
GML	Generalized Maximum Likelihood
ICS	Instrument Control Software
IRACE	InfRared Array Control Electronics
JMAP	Joint Maximum A Posteriori
LAOG	Laboratoire d'Astrophysique de l'Observatoire de Grenoble

LBV	Luminous Blue Variable
MAD	Multi-conjugate Adaptive optics Demonstrator
MTF	Modulation Transfer Function
NAOS	Nasmyth Adaptive Optics System
ONERA	Office National d'Etudes et Recherches Aéropatiales
OTF	Optical Transfer Function
PD	Phase Diversity
PSD	Power Spectral Density
PSF	Point Spread Function
RO	ReadOut
SNR	Signal to Noise Ratio
SR	Strehl Ratio
TCS	Telescope Control Software
TTM	Tip-Tilt Mirror
UT	Unit Telescope
VLT	Very Large Telescope
WFE	Wavefront Error
WFS	Wavefront Sensor

Acknowledgements

There is no doubt that the successful end of this ambitious venture has arisen from teamwork and it is a pleasure to write these lines and to say thank you to all the people who contributed to the accomplishment of the project and this thesis.

I would like to express my gratitude to Rainer Lenzen, the Principal Investigator of CONICA, for his fair and flexible leadership and for supervising me. His support and advice allowed me to easily get involved in astronomical infrared instrumentation and I benefited very much from his expertise.

I am glad that Prof Hans-Walter Rix was ready to take over my academic supervision. In case of emergency, he was never hesitant with quick advice and action. Thank you to Prof. Wolfgang Duschl who kindly agreed to referee my thesis, and to Prof. Wielen as well as Prof. Jähne for being jury members at the defence.

For a long time, CONICA was a well known acronym in the MPIA mechanical workshop headed by Armin Böhm. He and his employees contributed a lot to CONICA's successful completion. Additionally, Werner Laun and Peter Bizenberger were always prepared to help solve technical problems concerning cryogenics, optics or mechanical flexure. In the same way Karl Wagner, responsible for CONICA's control electronics, Heini Becker and Norbert Salm from the MPIA electronics department, supported me in many details and I am very thankful to all of you. In addition, I am thankful to Claudia Röhrle from the MPE for good co-operation concerning the detector fan-out board.

I appreciated a lot the team play with Clemens Storz who coded the control software for CONICA, as well as with Gerard Zins, responsible for the NAOS software, who implemented the software tools for the correction of static aberrations. Thereby, I thank Florian Briegel and Ulrich Hiller from the MPIA software group for all their uncomplicated and quick assistance in computer emergencies. Moreover, I apologize to Clemens Storz for being test target of sudden screen locks, the exchange of RGB channels or "Gertrud wartet!" cron-jobs.

An important assistance ensuring the smooth course of the CONICA project during the last days in Heidelberg was rendered by the members of the MPIA technical assistance, in particular through H. Zergiebel¹ and F. Witzel². Quick assistance was never a question!

On the French side of the project, I am obliged to Gerard Rousset, the Principal Investigator of NAOS, who proposed me for a Marie-Curie-Fellowship and who established the collaboration between ONERA, Observatoire Paris-Meudon and the MPIA to develop and implement the technique for the calibration of static aberrations. Thereby, I got to know Amandine Blanc, and I appreciated very much this co-operation, with her being always friendly and so conscientious. With a benign smile,

¹His taste for tobacco still has to be adjusted.

²Needs a more powerful fork-lift.

I recall Silvain Pau saying to me: “C’est mieux comme un grand barbu ...!”, when he met her the first time in the integration hall. I thank Thierry Fusco, who backed this collaboration, in particular for his work on data reduction during the hot days in Bellevue and during commissioning on Cerro Paranal.

I am grateful to François Lacombe, the technical project manager of NAOS, and Eric Gendron, responsible for the infrared wavefront sensor, for their overview and calmness during the count-down in Bellevue. Disregarding the lack of time, there was always an open ear, sense of humour and quick practical solutions to survive with.

In general, I enjoyed my stay in France very much, and I thank all NAOS team members who I got to know in the integration hall. Still to mention, Geneviève Michet with whom I shared my office and who always tried to establish some comfort in the harsh working environment of the yellow illuminated, window-less, integration hall, and Silvain Pau, who offered to me his apartment in Montparnasse with his insistent request to smoke cigars and to enjoy.

During re-integration and commissioning of the instrument in Chile, the technical ESO instrument responsables Martina Garcia and Gordon Gillet perfectly supported the German and French instrument teams. Fortunately, Martina took care for the spiritual relief of the teams, and taught us how to cook coffee on a flat iron and to play basketball without burning fingers.³ Furthermore, Nancy Ageorges, Marc Ollivier, Chris Lidman, Jason Spyromillio and Jean-Gabriel Cuby contributed a lot to successful commissioning.

Thank you very much to Laird Close and Wolfgang Brandner, the two subsequent instrument scientists of ESO for excellent co-operation. In addition, I would like to thank Gert Finger for a series of discussions concerning infrared array characteristics, Jörg Stegmeier, for very rapid answers concerning the command line control of the operating software, and Alan Moorwood, as ESO instrument responsible for CONICA, for all his remote support when CONICA was integrated with NAOS in France. Special thanks to Norbert Hubin for a half-year ESO contract that allowed for the finalization of static aberration compensation during commissioning on Cerro Paranal.

For proofreading of parts of my thesis, I thank David Butler, Wolfgang Gässler, Wolfgang Brandner, Peter Schuller and in particular I thank Tom Herbst who rendered assistance concerning data reduction and interpretation of the Fabry-Perot data.

Moreover, I must admit that without the little hint of my long-term friend Peter Schuller, I would have never applied for this job!

At the end, I wish to thank my parents in Stuttgart and in the Eifel who always supported and encouraged me on my ways, and I thank my wife and the Lord who bore the brunt of this work.

A wife of noble character who can find? She is worth far more than rubies. Proverbs (31:10)

³Note that both might conflict with Paranal Security.

Si vous voulez construire un bateau, il est inutile de réunir des hommes, de leur donner des ordres et de répartir les tâches. Donnez-leur simplement envie de partir à la découverte de mers lointaines.

Based on Antoine de Saint Exupery

